University of Iowa

Iowa Research Online

Theses and Dissertations

Spring 2018

Development of electrospun polymer nanofiber mats for removal of uranium from aqueous systems

Adam Joseph Johns
University of Iowa

Recommended Citation
Johns, Adam Joseph. "Development of electrospun polymer nanofiber mats for removal of uranium from aqueous systems." MS (Master of Science) thesis, University of Iowa, 2018.
https://doi.org/10.17077/etd.mb72nfd4

DEVELOPMENT OF ELECTROSPUN POLYMER NANOFIBER MATS FOR REMOVAL
OF URANIUM FROM AQUEOUS SYSTEMS

by

Adam Joseph Johns

A thesis submitted in partial fulfillment
of the requirements for the Master of Science
degree in Civil and Environmental Engineering in the
Graduate College of
The University of Iowa

May 2018

Thesis Supervisors: Associate Professor David M. Cwiertny
Associate Professor Tori Z. Forbes

Graduate College
The University of Iowa
Iowa City, Iowa

CERTIFICATE OF APPROVAL

_____

MASTER'S THESIS

_____

This is to certify that the Master's thesis of

Adam Joseph Johns

has been approved by the Examining Committee for
the thesis requirement for the Master of Science degree
in Civil and Environmental Engineering at the May 2018 graduation.

Thesis Committee: _____
                     David M. Cwiertny, Thesis Supervisor

                     _____
                     Tori Z. Forbes, Thesis Supervisor

                     _____
                     Syed Mubeen

To my friends and family, for I would not be here without your constant encouragement.

ACKNOWLEDGEMENTS

First and foremost, I would like to thank my parents for all of the support getting me to where I am today. None of this would have been possible without you guys. Jeremy, thanks for always being there to help me relax and enjoy myself. Dusty, you will always be in my heart and I wish you were here to see where I am today. Although you are not here physically, you are with me in spirit, constantly pushing me forward.

I would also like to thank both of my advisors, David Cwiertny and Tori Forbes, for their constant encouragement and guidance through my undergraduate and graduate career. Both of you guys have challenged me to be not only a better scientist but also a better, well-rounded person. You guys had faith in me at times when I didn't have faith in myself, giving me the courage to constantly move forward.

I would also like to give a huge shout out to all of my prior and present lab mats. From the Forbes group: Daniel Unruh, Madeline Basile, Andy Nelson, Andrew Knight, Eric Eitrheim, Ahsini Jayasinghe, Josh DeGroot, Maurice Payne and many others. From the Cwiertny group: Kathy Peter, Jiajie Qian, Andrew Kral and Matt Nagorzanski. You all were instrumental in helping me along the way whether it be scientific advice or just a person to lean on in a time of need.

ABSTRACT

Uranium contamination in drinking water sources, such as ground or surface water, poses a potential health risk. In areas, such as the Navajo Nation, uranium levels can be found at concentrations ~300 times higher than the maximum concentration limit (MCL) set by the Environmental Protection Agency (EPA) of 30 μg/L. Exposure to these contaminated waters can result in elevated uranium concentrations within the body even after several months of eliminating the source. Inside the body uranium is a nephrotoxin (damages the kidney) and has been linked to cancer among other health problems. Reducing these health risks towards individuals requires methods for cleaning uranium from aqueous systems and sensing it within water and body fluids for biomonitoring.

The objective of this work was to synthesize, characterize, and test electrospun polymer nanofiber mats capable of extracting uranium from water with applications in sensing and/or point of use (POU) treatments devices. Materials were synthesized with a suite of functional groups capable of extracting uranium from aqueous systems such as amidoxime, phosphonic acids, and quaternary ammonium salts (QAS) then characterized to evaluate materials physical and chemical traits. Batch uptake studies evaluated materials uptake rates, efficiency at varying pH's, and ability to remove uranium over a range of initial concentrations. Flow through studies assessed materials abilities to be used as a POU treatment technology for removing uranium from drinking water.

PUBLIC ABSTRACT

Within the Four Corner regions of the United States there are elevated uranium concentrations in unregulated drinking water sources. Using these water sources has associated health risks such as damage to kidneys and cancer, among other health issues. In order to mitigate these health risks the ability to detect and remove uranium from water is greatly desired. Current technologies for determining if water is contaminated can be time consuming and costly meanwhile removing uranium from water can require units which may require proper infrastructure. In order to overcome these issues, engineers have turned to using electrospun polymer nanofiber mats to be used as a potential solution for removing uranium from water.

In this work, electrospun polymer nanofiber mats were developed to be used for extracting uranium from water. These materials were tested to evaluate how much uranium they can capture in a variety of conditions. Flow through tests investigated how the materials were able to remove uranium in flow like conditions. These materials can be potentially used in sensing devices for detecting uranium concentrations in water or used as a treatment device for providing clean drinking water to those who use uranium contaminated source.

TABLE OF CONTENTS

LIST OF TABLES

LIST OF FIGURES

CHAPTER 1: INTRODUCTION

1.1 Uranium legacy contamination within the Navajo Nation

The Atomic Era is said to have begun on July 16th, 1945 after the successful detonation of a nuclear bomb code named Trinity.[1] After the close of World War II, America saw the potential for uranium (U) to be used as a source of military weaponry and as a civilian energy source. Consequently, the four corners region of the U.S. (Colorado, New Mexico, Arizona, and Utah) saw a subsequent increase in uranium mining activities to meet this new demand. Within this region is 27,000 square miles of land with abundant uranium ore deposits owned by the Navajo Nation.[2] Tribes leased these lands between 1944 and 1986, during which four million tons of uranium[2] was mined from the ore deposits. Mining operations typically hired Navajo Nation workers who were tasked with extracting uranium from the surface (e.g., canyon walls and mesa tops) or from underground.[2] High grade uranium ores (0.1-0.63 % U_3O_8)[3] were removed from the mines to be processed later while low-grade uranium ore and nonradioactive host rock was either left in waste piles or dumped down the sides of mesas.[2] By the 1970s the U.S. Atomic Energy Commission (USAEC) discontinued purchasing uranium due to their ample reserves.[2]

The decline in uranium demand led to the abandonment of approximately 523 uranium mines (AUMs) within the area (Figure 1-1). Surveys of these mines found that 78% exhibited radiation two times above background, while 50% of the mines were ten times above background.[2] At present, these AUMs are considered a major source for ground and surface water contamination by uranium and other radionuclides. For those who live within the Navajo Nation, these waters can be a source of drinking water for human and livestock consumption and irrigation of crops.[2]

1

Concern over uranium contamination in the Navajo nation and the desert southwest in general led to further investigations of the levels of uranium in surface and groundwater within these regions. A study conducted by Blake et al. investigated the uranium contamination in a spring in the vicinity of an abandoned mine in Northeastern Arizona. Uranium concentrations from the acid mine waste (pH 3.8) were elevated to ~160 µg/L,[4] which exceeds that of the maximum contaminant limit (MCL) set by the Environmental Protection Agency (EPA) (30 µg/L).[5] These concentrations were higher than observed in the nearby spring (~pH 7), which possessed values of 67 and 135 µg/L.[4] Kamp et al. also conducted a study near Shiprock, New Mexico to investigate the contamination of groundwater at a former uranium mill site adjacent to a floodplain. Uranium concentrations in the area varied from 1.5 µg/L to 9280 µg/L, with 32 of the 33 samples being above that of the MCL.[6]

At high uranium concentrations in water there is potential for increased toxicological risk for the public. Exposure studies found that people exposed to high uranium concentrations in water (620 µg/L average) had an average uranium concentration of 0.162 µg/L in their urine (highest detected at 9.55 µg/L) several months after exposure.[7] These levels are approximately 5 times higher than that of a reference range concentration at 0.0345 µg/L (95th percentile; 500 U.S. residents to establish a baseline concentration).[8] There is no established legal limit for uranium in urine for civilians, although the U.S. Nuclear Regulatory Commission (NRC) has set an action limit of 15 µg/L for those with occupational exposure to uranium.[9]

High levels of uranium in drinking water can lead to health effects, although it is the chemical toxicity rather than the radiotoxicity that is of concern. Short-term exposure of uranium is normally not of concern due to the poor absorbing efficiency of uranium in the gastrointestinal tract (0.1%-6%).[10] During long-term exposure uranium will start to accumulate

2

within the kidney, liver, and bones with a majority being stored in bones.[11] The accumulation of uranium has shown to result in pathological alterations within the kidney[12] while other studies suggest that it imposes greater cancer risks than those without exposure.[13]

1.2 Radiochemistry of uranium within the environment

Uranium ($[Rn]5f^36d7s^2$) is located in the actinide series at the bottom of the periodic table and is the heaviest element to naturally occur at significant quantities within the environment. Three isotopes, ^{238}U, ^{235}U, and ^{234}U, occur at relative mass abundances of 99.28, 0.72, and 0.0055%, respectively.[14] Other isotopes, most notably ^{236}U and ^{232}U, can be synthesized in nuclear reactors; both ^{236}U and ^{232}U have practical applications as tracers for chemical yield during uranium analyses. All of the isotopes undergo alpha decay in which a helium atom is ejected from the nucleus, creating a daughter atom in the following process:

$$^{238}_{92}U \rightarrow {}^{234}_{90}Th + {}^{4}_{2}He \qquad \text{Eq. 1-1}$$

Rates of decay are quantified by their half-life, which is defined as the time it takes for a specific isotope to decay to half of the original value.[15] All three natural isotopes have considerably long half-lives of 4.5×10^9, 7.0×10^8, and 2.5×10^5 y for ^{238}U, ^{235}U, and ^{234}U, respectively.[15] Although each uranium atom undergoes alpha decay to produce a daughter product atom, these daughter products also decay to produce other elements until they ultimately end at a stable element. For ^{238}U and ^{235}U, twenty-five radioactive daughter products are formed that span thirteen different elements in either the uranium or actinium series and include the production of ^{234}U through decay of the ^{238}U parent (Figure 1-2).[15]

3

The radioisotopes produced through these decay series can lead to environmental and public health concerns. As each new element is created, the chemical properties of the daughter product changes, which can influence the fate of this and subsequent radionuclides. A notable example of this phenomenon is the intimate relationship between radium and its daughter product radon. Radium-226 is a divalent cation that is part of the ^{238}U decay series and highly soluble in water.[15] Its daughter product is radon-222, an inert noble gas, that typically diffuses out of water and into the air. This behavior has public health implications because radon can be released from water distribution systems or seep through cracks in concrete foundations, leading to inhalation by inhabitants.[16] Radon rapidly decays ($t_{1/2} = 3.823$ days), emitting alpha particles that can cause damage to lung tissues.[17]

Although there are environmental and public health concerns regarding some of the daughter products within these decay series, others have beneficial uses as an investigative tool for researchers. A famous example is their use in geochronology, the method of dating rock formations, to determine the age of the Earth at 4.54 billion years old.[18] Because both decay series end with stable lead, ^{238}U to ^{206}Pb and ^{235}U to ^{207}Pb, scientists are able to measure their concentrations in rocks to calculate their age.[18]

Uranium can occur in multiple oxidations between +III and +VI, with +IV and +VI being the dominant oxidation states within environmental systems. The +V oxidation state can occur in some cases, but it rapidly undergoes disproportionation reactions to form +IV and +VI oxidation states.[15] In acidic conditions (less than pH 1) uranium +IV can be found as a U^{4+} ion, although as the pH increases it will readily hydrolyze to form uranyl oxhydroxide clusters, colloids, and amorphous uranium dioxide (UO_2).[15] The +IV state is relatively stable under anoxic conditions, but it will typically slowly oxidize to +VI in the presence of oxygen. In the

4

+IV state, uranium is not found as the free ion but rather it forms two strong bonds to O atoms to create the UO_2^{2+} cation. Within oxidizing surface waters, the chemistry associated with the UO_2^{2+} cation dominates, whereas more anoxic conditions can sometimes occur within groundwater (Figure 1-3).

The chemistry of uranium and how it behaves in the environment is dependent largely on the pH and the presence and abundance of suitable ligands. Uranyl exists as a linear molecule, with two strongly bound oxygen atoms located in the axial positions to form the dioxo cation. Four, five, or six additional bonds between the metal cation and ligands in the equatorial plane can form an overall square, pentagonal, or hexagonal coordination geometry.[19] As pH increases, uranyl will readily hydrolyze through olation and oxolation reactions, causing polymerization of the uranyl coordination complex to form dimeric, trimeric or larger uranyl colloidal species.[20]

As uranium is a strong Lewis Acid, it will readily accept electrons from O- and N-functional groups associated with inorganic or organic ligands. Uranyl coordination occurs as an equilibrium reaction, below:

$$UO_2^{2+} + L^n \rightleftharpoons UO_2L^m$$ Eq. 1-2

where uranyl and the ligand (L) with a certain charge (n) will form a uranyl-ligand complex (UO_2L) with a new overall charge (m). This reaction is characterized as follows:

$$\beta = \frac{[UO_2L^m]}{[UO_2^{2+}][L^n]}$$ Eq. 1-3

5

where the ligand constant (β) is the ratio of the uranyl-ligand complex concentration ($[UO_2L^m]$) over the free uranyl and ligand concentrations ($[UO_2^{2+}]$ and $[L_n]$, respectively). For inorganic oxyanions, the strength of bonding weakens in the order of $PO_4^{3-} > CO_3^{2-} > SO_4^{2-} > NO_3^-$, suggesting that a higher valence state of the ligand results in stronger bonds with UO_2^{2+} cation as seen by their associated ligand constants (Table 1-1). Molecules that contain carboxylate, alcohol, and amidoxime groups are common organic ligands that strongly bind the uranyl cation in aqueous solutions.[21–23]

While there are many ligands that can interact with the uranyl cation to form a stable complex, the environmental relevance of these molecular species is related to their natural abundance in surface and groundwater and their solubility in water. Carbonate is considered the most important ligand for uranium mobility due to its natural abundance in ground and surface waters.[24] Sources of carbonate in surface and groundwater include dissolved carbon dioxide from the atmosphere and dissolution of rocks (e.g. limestone and dolomite).[24] Carbon dioxide from the atmosphere can dissolve into water and react to form carbonic acid as follows:

$$CO_2(aq) + H_2O \rightleftharpoons H_2CO_3(aq) \qquad\qquad \text{Eq. 1-4}$$

Carbonic acid can then lose a proton to create bicarbonate (Eq. 1-5) with a pKa of 6.35[25] while another proton can be lost to create carbonate (Eq. 1-6) with a pKa of 10.33[25] as follows:

$$H_2CO_3(aq) \rightleftharpoons H^+(aq) + HCO_3^-(aq) \qquad\qquad \text{Eq. 1-5}$$

$$HCO_3^-(aq) \rightleftharpoons H^+(aq) + CO_3^{2-}(aq) \qquad\qquad \text{Eq. 1-6}$$
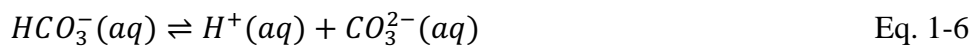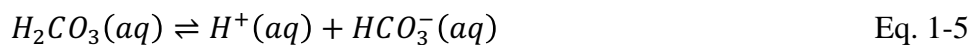
Carbonate containing mineral dolomite[26] contributes carbonate to water by dissolving and releasing carbonate as well as calcium and magnesium and is governed by its solubility as seen below:

$$CaMg(CO_3)_2 \rightleftharpoons Ca^{2+} + Mg^{2+} + 2CO_3^{2-} \qquad \text{Eq. 1-7}$$
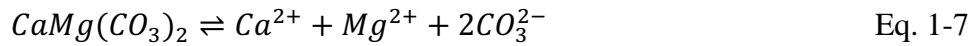
$$K_{sp} = [Ca^{2+}][Mg^{2+}][CO_3^{2-}]^2 \approx 10^{-17} - 10^{-19} \qquad \text{Eq. 1-8}$$

where the solubility constant (K_{sp}) is related to the soluble species activity raised to the power of their molar coefficient.

Within the Navajo Nation, high bicarbonate/carbonate concentrations have been found in surface and ground waters. For example, surface waters near Laguna Pueblo, NM had CO_3^{2-} concentrations between 43.2 – 223.2 mg/L (pH's between 7.07 and 8.58).[27] This is compared to that of groundwater near Shiprock, NM that had concentrations of HCO_3^- between ~100-1500 mg/L (pH's between 6.4 and 7.7)[6] where CO_3^{2-} would be at ~ 0.5% of these concentrations (0.5-7 mg/L). At such high concentrations in surface waters and ground waters, carbonates can compete with uranium hydrolysis products, creating highly soluble uranyl carbonate species and contributing to enhanced mobility of uranium in the environment.

1.3 Analysis of uranium in aqueous systems

There are multiple analytical methods that can be used for the detection of uranium in aqueous systems. These range from spectroscopic (e.g., absorption, vibrational, or fluorescence), inductively coupled plasma in tandem with mass spectrometry or optical emission spectrometry (e.g., ICP-MS/OES), or radioanalytical techniques. When choosing an analytical method for

7

detecting uranium in water, the main concern is being able to detect levels relevant to the drinking water standard or bodily fluids (e.g. urine and blood) for biomonitoring of those exposed to uranium. This means the method should be able to at least detect uranium at the 30 μg/L MCL set by the EPA and robust enough to analyze complex chemical matrices such as blood and urine. There may also be concerns towards obtaining isotopic data, which can give insight into natural fractionation and uranium source information. Based upon the criterion above, alpha spectrometry and inductively coupled plasma mass spectrometry/optical emission spectroscopy (ICP-MS/OES) are the two gold standards for uranium analysis in water and in bodily fluids (e.g. urine or blood) for biomonitoring. Both methods have their advantages and disadvantages, and choosing which is most appropriate for use must account for factors such as cost, labor, and availability.

1.3.1 Alpha spectrometry

Alpha spectrometry detects the emission of an alpha particle with an energy specific to that of the parent material. For the natural uranium isotopes, these energies are considered monoenergetic at 4.27, 4.67, and 4.86 MeV for ^{238}U, ^{235}U, ^{234}U, respectively.[28] The area of the peaks can be integrated to provide quantitative information on the concentration of the sample while the energies correlate to the identity of the specific isotope. To collect quantitative data, samples are spiked with a uranium tracer (to confirm yields) and then undergo an extensive separation procedure to remove any radionuclides that may have overlapping energies and interfering ions. These separations can be laborious, time consuming, and typically generate a lot of acidic and caustic waste. After the uranium is separated, it is deposited on a planchette by either micro-coprecipitation or electrodeposition, with both methods producing a thin layer of

8

uranium on the surface. These sources can then be counted in a vacuum chamber, where the alpha particles have a direct path to hit a semiconductor surface, producing an electric signal which can be detected and converted to isotopic information. Using the radiotracer, the efficiency of chemical separations can be determined and thus the original uranium concentration can be calculated based upon separation efficiencies. The benefits of this technique is that it is can detect uranium at low levels, such as 0.3 pCi/L (150 mL samples and 300 minutes count times), which correlates to 0.892 µg/L for ^{238}U and 0.139 µg/L for ^{235}U.[29] Alpha spec is capable of being detecting uranium in complex matrices and provides isotopic data, but it also requires skilled labor, is time intensive, and generates significant quantities of waste.

1.3.2 ICP-OES/MS

ICP-OES/MS has an easier sample preparation procedure because it does not require extensive separation processes that are necessary for the alpha spectrometry. Filtering samples with a 0.45 µm filter can separate suspended metals (metals stuck on filter) and dissolved metals[30] while also removing large particles that can be harmful to the instrument. Samples are typically acidified in nitric or hydrochloric acid to keep samples stable and dissolved in the solution. The timing of the sample acidification can aid in determining the level of suspended solids in solution. If you add acids to samples initially, total metals are analyzed (suspended and dissolved). Filtering and then acidifying the sample will leave just the dissolved metal fraction and this can be subtracted from the total to determine the concentration of suspended and dissolved metals. Samples are commonly diluted when total dissolved solids (TDS) are present at concentrations greater than 0.2 wt% to protect the instrument and allows for lower detection limits.[30]

Samples are introduced into the machine by nebulization in an argon carrier gas, producing small liquid droplets. These small droplets are then ionized via electromagnetic induction to create a plasma, which reaches temperatures between 9000 to 10,000 K.[30] Both ICP-MS and ICP-OES use the same sample introduction system (ICP), but utilize different detectors. In ICP-OES, this plasma contains ionized atoms that emit a specific wavelength of radiation and the intensity can be correlated to the elemental abundance.[30] Interferences in analysis typically occurs when elements emit overlapping wavelengths, which must either be accounted for or eliminated from the samples. In ICP-MS, the ionized atoms are focused in an electrical field by their mass to charge ratio (*m/z*), where only ions with a specific *m/z* make it through to the detector.[30] Interferences can occur when ions become doubly charged or polyatomic, which can typically be reduced with a collision gas or by eliminating them from the samples. The benefits of this analytical approach are the low detection limits for uranium and relatively easy sample preparation, but the instrumentation costs are high and require a skilled technician for analysis due to the many potential interferences that can occur.

1.4 Technologies for removal of uranium from drinking water

Current small system compliance technologies (SSCT) for removing uranium from small drinking water systems (e.g. homes) includes point of entry (POE) and point of use (POU) devices. POE devices treat all of the water as it enters the home whereas POU treats water where it is used (e.g., the tap). POE devices are typically more expensive and complex than that of POU devices due to the larger volumes that are processed. Since uranium is only harmful when inside the body, only drinking water is required to be treated in homes. This means that both systems work for treating water but POE is not necessarily required since it treats more

water than what is necessary for mitigating human health risks. Factors to consider when choosing POE and POU systems includes capital costs, operating and maintenance schedules, and water quality parameters among other factors.[31]

Existing EPA approved POU systems for uranium include anion exchange and reverse osmosis technologies, while POE systems includes anion exchange, reverse osmosis, and activated alumina.[31] All of these systems are typically able to treat large amounts of uranium and reduce its concentration to below the MCL. For example, Sorg[32] investigated the bench scale removal of uranium in pond water using activated alumina resins. The original uranium concentrations in the pond water were measured at 273 to 432 µg/L U (pH 7.2-8.2), but application of activated alumina resins could reduce the uranium concentration in the treated supply to ~1 µg/L for up to 2000 bed volumes.[32] Sorg was also able to demonstrate that anion exchange columns were able to remove >90% of uranium at concentrations between 175 to 300 µg/L (pH 7.4-7.7). This study also indicated that the system was relatively robust, with this level of uranium removal occurring over 7,500 bed volumes when using just 55 mL of resin.[32] Reverse osmosis was demonstrated to have the best performance, with 99% removal of uranium (initial concentration of 300µg/L) with no sign of breakthrough.[32] Although all of these systems are capable of removing uranium to below that of the MCL, the technology can be difficult to use with underserved populations (e.g., the Navajo Nation) due to costs and lack of infrastructure. For example, reverse osmosis allows for great removal of uranium but requires high operating pressures which can be costly and requires the proper piping and pumping to allow for treatment.

11

1.5 Electrospinning of polymer nanofiber mats

The aforementioned treatment technologies (anion exchange, reverse osmosis, and activated alumina) are all efficient at removing uranium, but may not be practical choices for those who live in areas of low infrastructure such as the Navajo Nation. Factors such as high costs, routine maintenance, and dealing with potentially low level nuclear waste can be potential problems. Electrospun nanofiber mats offers a potential solution to these issues with low capital costs, little to no maintenance, and can be replaced frequently to avoid the accumulation of uranium at levels of low level nuclear waste.

Polymer nanofiber mats are an attractive material for use as an adsorbent for a wide range of inorganics and organic molecules.[33] They have been previously used in water treatment[33,34], bone and tissue regeneration[35,36] and a variety of sensing devices[37–39]. Polymer nanofibers are desirable for many of their applications, including environmental treatment, due to their high surface area to volume ratio, cheap and easy synthesis, mechanical stability, and high porosity.

One approach to fabricating nonwoven polymer nanofibers mats with high surface areas for enhanced adsorption is electrospinning. An overview of the electrospinning process and apparatus is provided (Figure 1-4). This method starts by dissolving a polymer in an appropriate solvent to create a sol gel that can be used during the electrospinning process. The polymer nanofibers are fabricated by pushing the sol gel through a small blunt needle with a high applied positive voltage (~10-25 kV). This applied potential breaks the surface tension of the solution and creates a whipping jet referred to as a Taylor cone that transforms the sol gel into the solid nanofibers. The nanofibers deposit on a grounded collector surface, producing a non-woven nanofiber mat structure while the solvent evaporates. This approach produces a mat that is typically 25 cm x 10 cm with a thickness of a ~20-100 mm and can be spun with either

hydrophobic (polyvinylidene fluoride (PVDF) and polystyrene (PS)) or hydrophilic polymers (polyacrylonitrile (PAN) and poly(methyl methacrylate) (PMMA)).

Although some polymers like PAN have functional groups capable of metal binding (e.g., nitrile groups), additional functionalization of the polymer mats is typically required to improve uptake of contaminants of interest to levels needed for treatment technologies. Functionalization of electrospun nanofibers can be accomplished either by altering the synthesis precursor solution (e.g., adding metal binding agents including surfactants or nanoparticles into the sol gel) or by post-synthesis processing (e.g., reaction) of the polymer backbone itself. For example, arsenate and chromate were successfully removed by a multi-functional nanofiber mat consisting of ferrihydrate nanoparticles and quaternary ammonium salts (QAS) that were produced via a single-pot synthesis using a sol gel mixture of all reagents.[40] As an example of post-synthesis processing PAN nanofibers have been modified with ethylenediaminetetraacetic acid (EDTA) for capture of chromium and cadmium.[41]

For uranium uptake, post-functionalization of PAN mats has previously been explored for treatment of contaminated water[42], but less is known regarding the effectiveness of alternative nanofiber formulations prepared via embedded surfactants or other types of binding agents within polymers. A common post-functionalization route for PAN involves reducing its nitrile groups to produce amidoxime groups (Figure 1-5A), which are highly selective to U(VI), thereby generating a material that can scavenge ppm levels of uranium from seawater.[21,43] Surfactants such as phosphonates have also been developed for uranium chelation and separations. Bis(2-ethylhexyl) phosphate (HDEHP) is a widely used phosphonate based extractant for uranium used in solvent extractions.[44,45]

13

1.6 Challenges for detection and treatment of uranium

1.6.1 Detection challenges

Although alpha spectrometry and ICP-MS/OES offer excellent detection limits, even in complex chemical matrices such as urine or groundwater, they have drawbacks due to instrumentation costs, need for highly trained personnel, and time-intensive sample preparation and measurement. These techniques also do not provide information on the chemical speciation (e.g., what ligands are bound to the uranyl). This information is desired to aid in risk assessment for remediation efforts and chelation therapy.[46,47] Therefore, it would be desirable to create a new real-time detection method that is low cost, easy to use, and provides enhanced chemical information.

A viable option for this advanced detection is Raman spectroscopy, which uses scattered monochromatic light to uniquely identify molecules both in solution and solid-state samples. As one wavelength of light moves through a sample, analytes shift this wavelength to that of lower or higher energy which is unique for each molecule. Unfortunately, approximately 1 of 10^7 photons that hit an analyte undergo inelastic Raman scatter, leaving it with poor detection limits for uranium.

In order to enhance these signals, surface-enhanced Raman spectroscopy (SERS) can be used which enhances Raman scattering by up to 10^{11} when adsorbing analytes to rough metal surfaces or nanoparticles.[48,49] The exact mechanism of this phenomenon is still debated, although its usefulness has been exploited by scientists. For example, it has been investigated as a potential biosensor for measuring glucose *in vivo* in diabetic patients with detection limits below those established by the International Organization Standard.[50] For uranium detection, it has been found that gold nanostars (AuNS) can be used with SERS to detect uranium in aqueous

14

solutions down to 0.12 µM (~28.56 µg/L),[51] concentrations which are relevant for regulating

drinking water sources.

Although SERS can detect uranium at levels near the MCL of uranium, there are still

inherent concerns. There are issues with AuNS stability in aqueous solutions, which could be

further complicated in complex matrices such as urine and ground water. The ability to increase

the detection limit of U(VI) in solution with SERS is hampered by this instability and limitations

on binding. There are also inherent cost issues of having to use gold as a SERS substrate, which

hinders its economic viability.

1.6.2 Treatment challenges

In underserved populations, such as the Navajo Nation, economic and infrastructural

factors influence the ability to use POU technologies. For example, RO systems need high

operating pressures which requires the proper infrastructure, such as pumps, and is an energy

intensive process. Consequently, these high operating pressures also increases the cost of RO due

to energy costs. In order to make POU technologies viable for underserved populations, cheap

technologies that can remove uranium from complex matrices (e.g. ground and surface water)

while also being able to operate under ambient conditions (e.g. little pressure drop) are desired.

1.7 Research motivation and objectives

Currently, there are inherent issues that must be addressed before sensing of uranium

with SERS can be used to detect uranium at levels near or below its MCL. The ability to

concentrate uranium from complex matrices (e.g. urine and ground water) is required to

overcome the technological and economic factors hindering SERS. To address these issues,

electrospun polymer mats can be developed to create a material that can selectively bind and preconcentrate the U(VI) and remove chemical matrix interferences. AuNS can then be deposited onto the polymer mats which will reduce the amount of AuNS used per sample.

Meanwhile, POU treatment of water in underserved populations is hindered by the costs and infrastructure requirements of EPA approved POU technologies (anion exchange and reverse osmosis). To make POU treatment viable in underserved populations a cheap, yet robust, material is desired that can remove uranium from ground and surface water under conditions that require little to no new infrastructure. Electrsopun polymer mats offer a material for POU technologies which allows for high fluxes of water while inducing little pressure drop due to the high surface area and porosity of the mats.

In order to maintain the affordability of materials, cheap synthesis techniques are required. This can include cheap chemical modification, such as amidoximation, or by using commercially available surfactants. Commercially available surfactants include phosphonic based surfactants such as hexadecyl phosphonic acid (HDPA) and HDEHP as well as QAS such as Aliquat 336® (Aq), which are all depicted in Figure 1-5B. HDPA and HDEHP are thought to incorporate uranium via metal chelation due to the strong bonds formed between phosphates and uranium. For example, phosphonic acid has been attached to the surface of TiO_2 or magnetic nanoparticles, and previous work suggested that these materials have high uranium sorption capacities (up to 1250 and 2330 mg per g of sorbent material).[52,53] Comparatively, Aq is expected to undergo anion exchange with the negatively charged uranyl in solution. For example, strong base anion exchangers (similar to Aq) have been used to extract uranium from sulfate, hydrochloric, nitric, and carbonate media.[54,55] The downside of using strong base anion exchangers though is their dependence on uranium speciation in aqueous systems, which can

vary depending on the ionic strength, pH, and ligand availability. All three of these surfactants (HDEHP, HDPA, and Aq) and post-functionalization routes (AOPAN) are promising functional agents for extracting uranium.

The overarching goals of this research project is to combine electrospun nanofiber mats and functional binding agents (such as the ones mentioned above) to extract uranium from a variety of aqueous systems. Specific objectives related to this goal includes:

Objective 1: Synthesize and characterize polymer nanofiber mats with incorporated functional groups previously mentioned of post-functionalized amidoxime or HDEHP, Aq, and HDPA surfactants.

Objective 2: Test materials in batch systems to determine influence of pH, uptake rates, and uranium capacities on materials.

Objective 3: Test materials in dead-end filtration systems to investigate materials ability to remove uranium under flow.

These three objectives will investigate the applicability of electrospun polymer nanofiber mats as materials to be used for concentration of uranium from aqueous solutions onto a solid material. In Chapter 2 the materials and methods used within this thesis are described. This includes the synthesis and characterization of materials, experimental details, descriptions of the materials used for experiments and the methods for obtaining data. This is followed with Chapter 3 which displays and describes the results found and provides useful discussion of these

results. Finally, Chapter 4 serves to summarize the conclusions made herein and the implications

of this work as well as the additional research required for technology development.
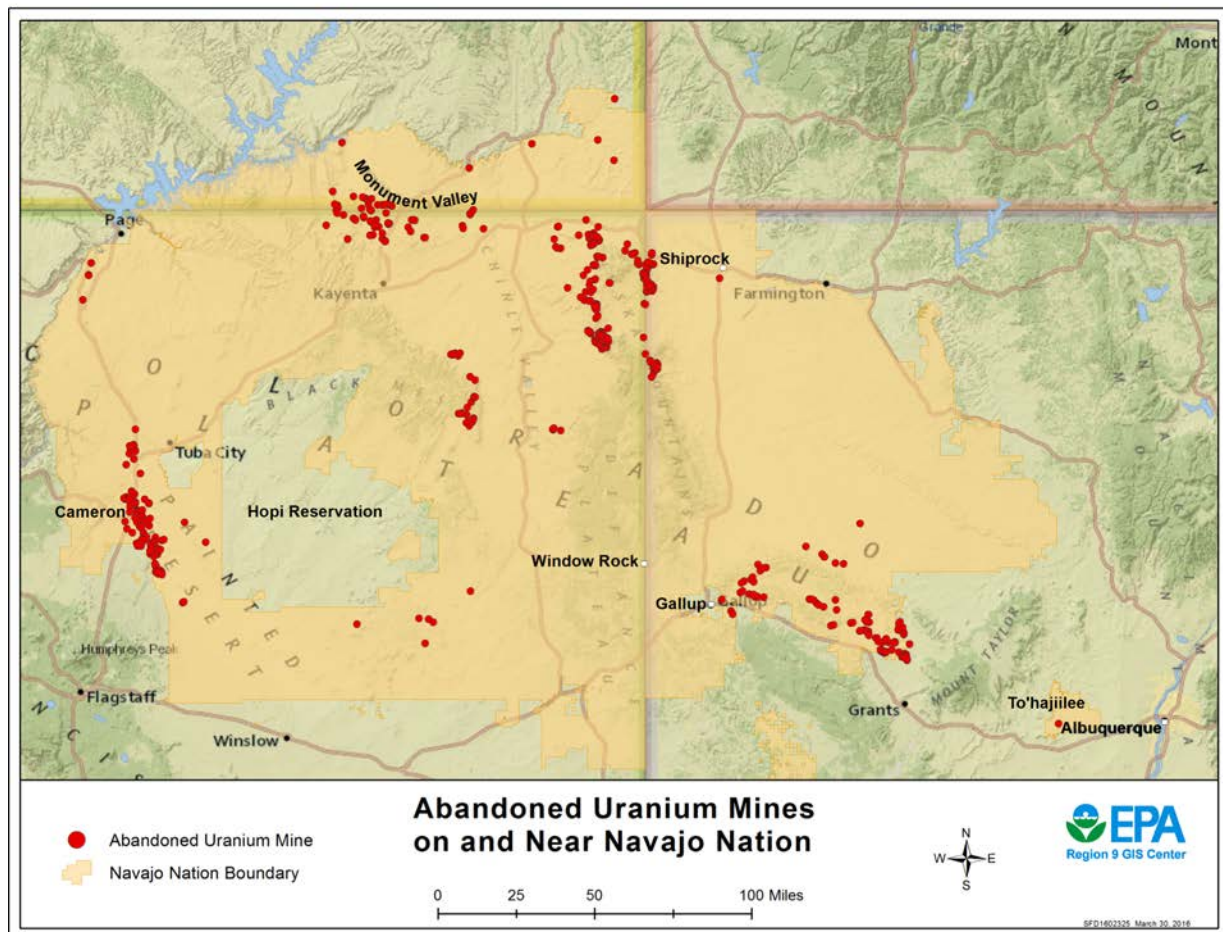
Figure 1-1. Abandoned uranium mines scattered through the Navajo Nation area within the four corners region of the US. Reproduced from US EPA Navajo Nation.

www.manaraa.com
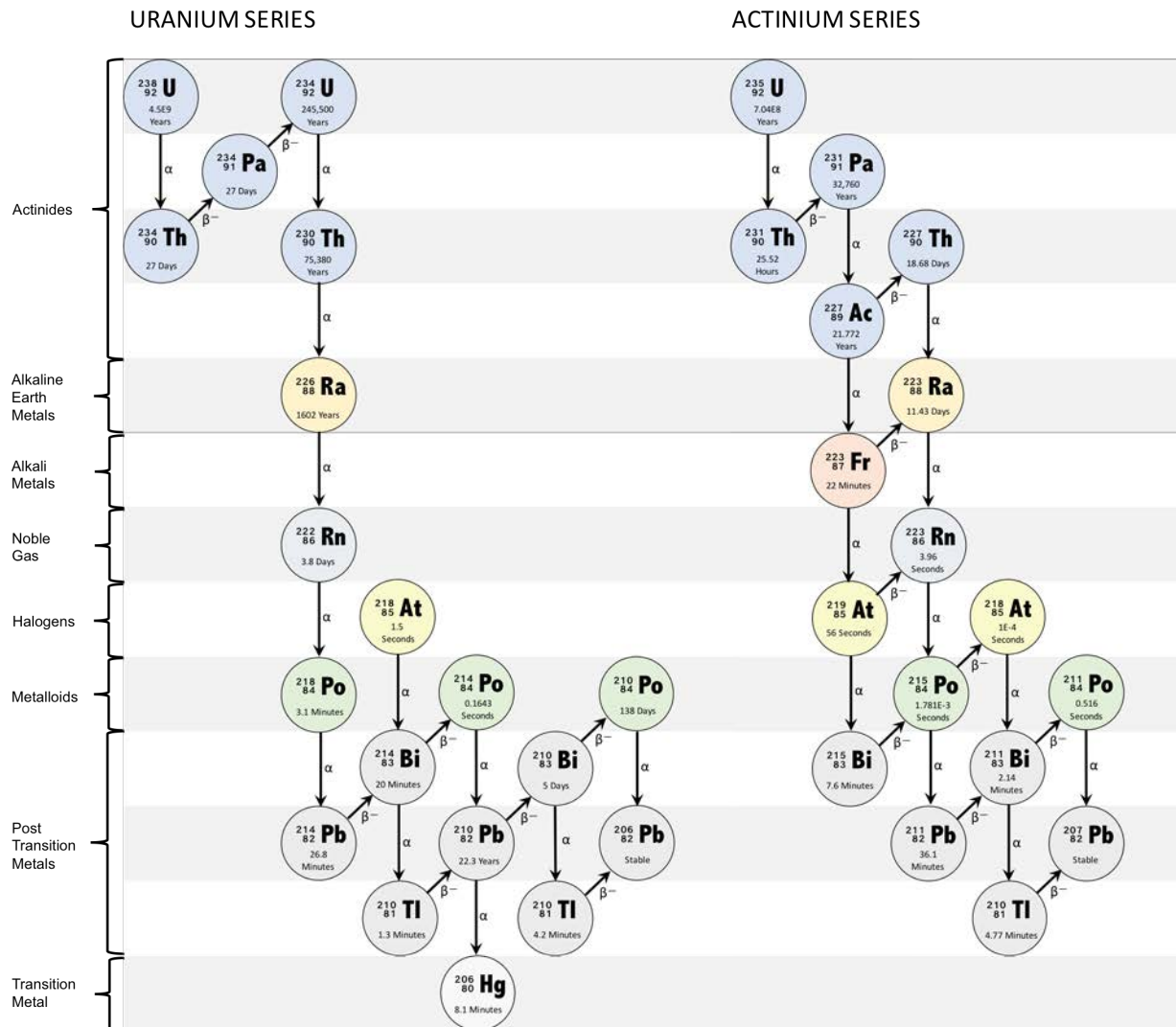
Figure 1-2. Uranium and actinium decay series. Reproduced from Wikipedia contributor BatesIsBack.

"Atlas of Eh-pH diagram" by Geologic Survey of Japan, Report 419

Surface water conditions

Groundwater in the desert southwest
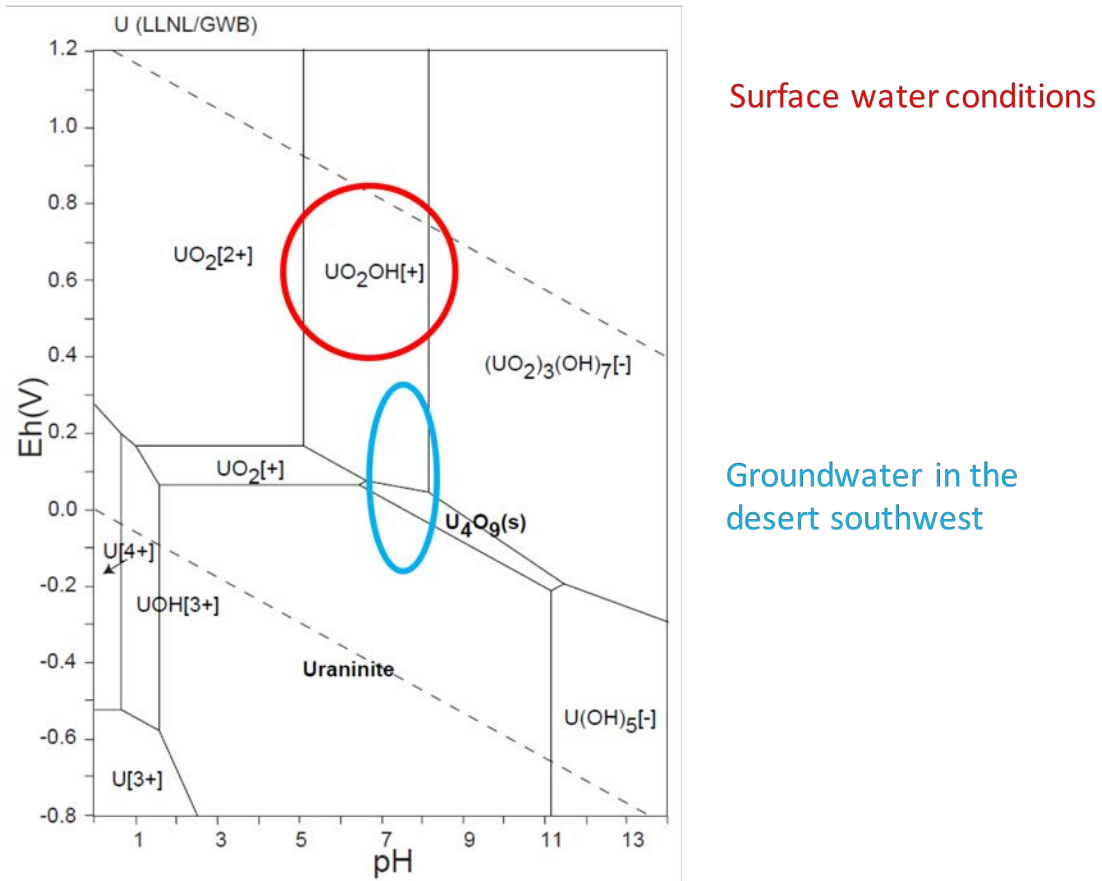
Figure 1-3. Pourbaix diagram for uranium with typical ground and surface water pH and Eh regions labeled.[136]
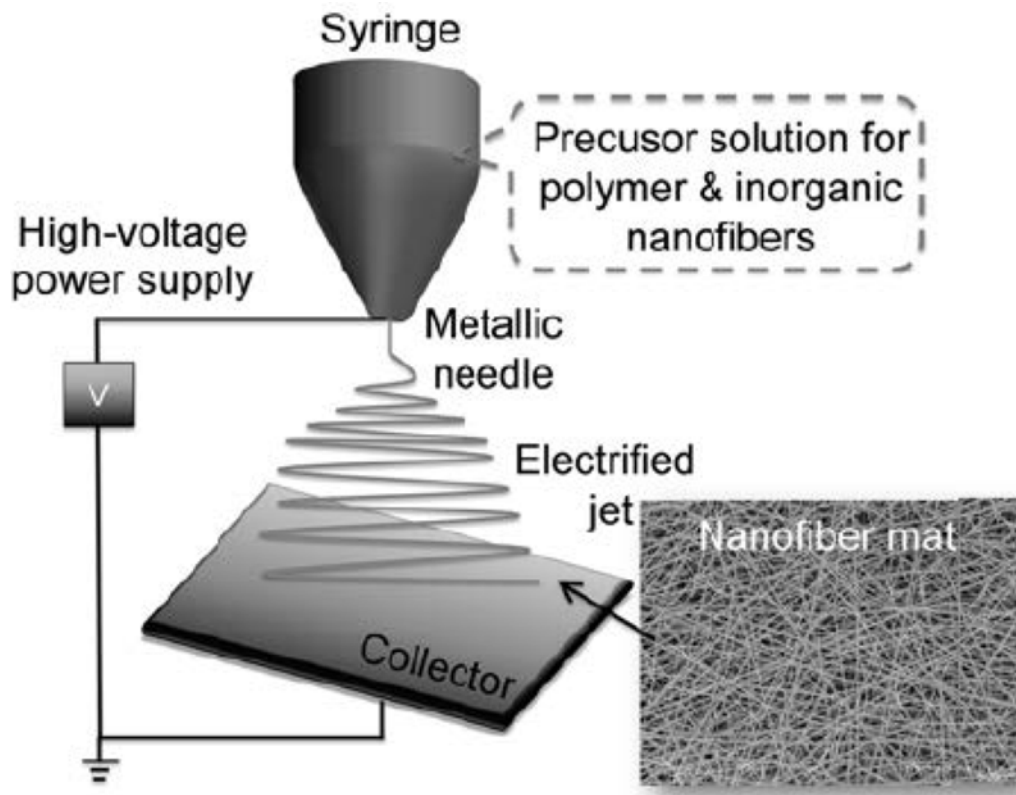
Figure 1-4. Electrospinning technique.
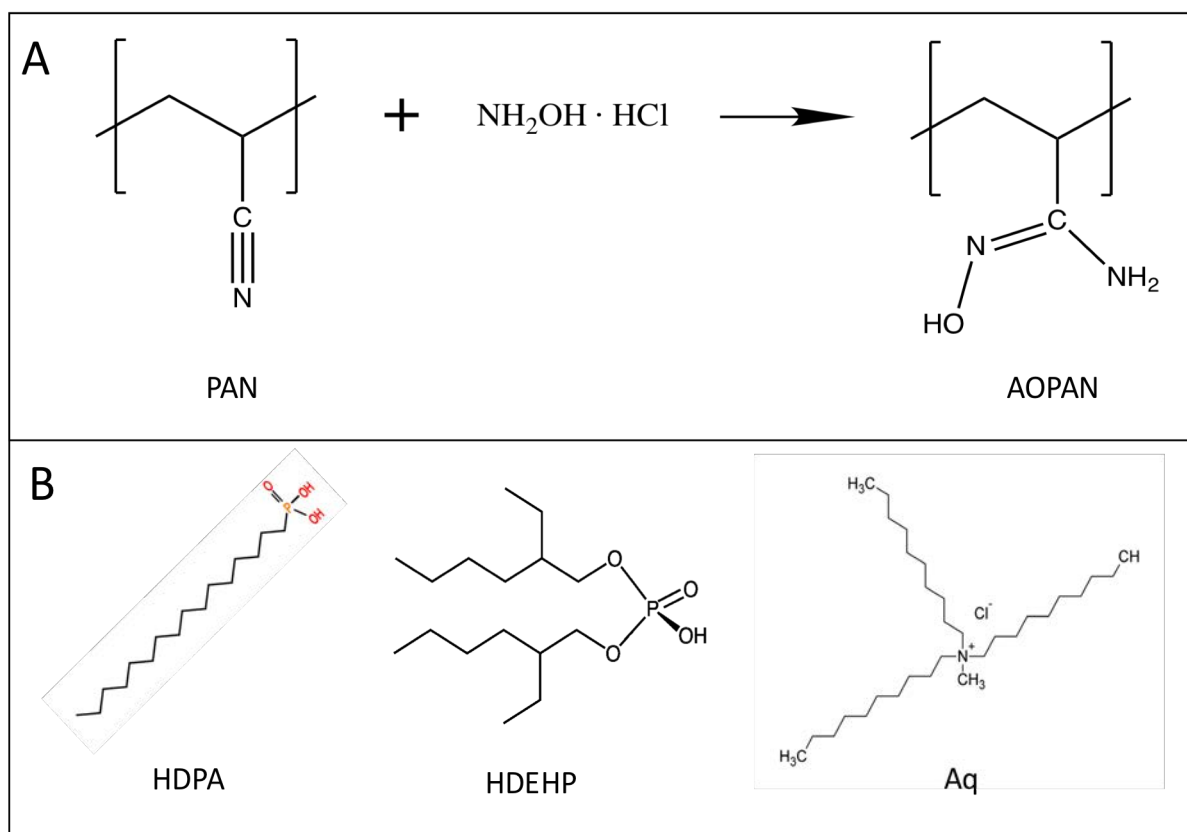
Figure 1-5. Binding agents used in polymer nanofiber mats with (A) post-functionalization of PAN to AOPAN and (B) surfactants incorporated into the polymer matrix.

Table 1-1. Reactions of uranyl with oxyanions and their associated ligand constants

Oxyanion	Reaction	Logβ[80,137]
PO_4^{3-}	$UO_2^{2+} + PO_4^{3-} \rightarrow UO_2PO_4^{-}$	13.25
CO_3^{2-}	$UO_2^{2+} + CO_3^{2-} \rightarrow UO_2CO_3$ (aq)	9.94
SO_4^{2-}	$UO_2^{2+} + SO_4^{2-} \rightarrow UO_2SO_4$ (aq)	3.40
NO_3^{-}	$UO_2^{2+} + NO_3^{-} \rightarrow UO_2NO_2^{+}$	0.04

CHAPTER 2: MATERIALS AND METHODS

2.1 Reagents

All reagents were used as received. Polymers used in electrospinning were polyacrylonitrile (PAN; MW 150,000, Aldrich) and polyvinylidene difluoride (PVDF; MW 180,000, Aldrich). Solvents used to dissolve polymers included N,N-Dimethylacetamide (DMA; 99.8%, Aldrich), N,N-dimethylformamide (DMF; 99.85%, BDH Chemicals), dimethyl sulfoxide (DMSO; ≥99.9%, Fisher Scientific), acetone (≥99.5%, Aldrich), and glacial acetic acid (GAA; ≥99.7%, Fischer Scientific). Surfactants added to precursor solutions were Aliquat® 336 (Aq; Alfa Aesar), bis(2-ethylhexyl phosphate (HDEHP; 97%, Aldrich), and hexadecyl phosphonic acid (HDPA; 97%, Aldrich). Batch experiments were conducted in 10 mM HEPES buffer (≥99%, Aldrich), calcium chloride dihydrate (99%, Fisher Scientific), calcium nitrate tetrahydrate (99%, Aldrich), sodium bicarbonate (99.7%, Fisher Scientific), or Surine™ Negative Urine Control (Cerilliant). Amidoximation of PAN mats used hydroxylamine hydrochloride (98%, Aldrich) and sodium hydroxide (97.0%, Fisher Scientific).

2.2 Electrospinning of polymer mats

2.2.1 PAN-PVDF composite

To enhance the mechanical stability and handling of PAN nanofiber mats, a composite material was created to have a PVDF backbone. The PVDF layer of the composite material, 12 wt% PVDF was dissolved in DMA and acetone (3:7 volume ratio) by mixing at 60°C for 2 h at 700 rpm (Eppendorf ThermoMixer C). For the PAN layer of the composite, 7 wt% PAN was dissolved in DMF by mixing at 60°C for 2 h at 700 rpm. Six mL of the PVDF sol gel was added to a 12 mL plastic syringe (HSW Norm-Ject) that was subsequently loaded onto a syringe drive

25

(New Era Pump Systems, Inc.). A polyethylene (PE) 1/16" female luer lock fitting was connected to the syringe and a 2.0 mm ID PE tube was attached to the lock fitting. The tubing was then connected to a metal nozzle adapter (NanoNC Co., Ltd) by another PE 1/16" female leur lock fitting and a ½" 25G needle attached to the other end of the nozzle. A distance of 10 cm was created between the end of the needle tip and the surface of a 9-5/16" circumference metal drum collector (SPG Co., Ltd; Korea). The metal drum was grounded and covered in Al foil for collection of the electrospun polymer composites. PVDF was electrospun first by eluting the polymer solution through the needle at 0.4 mL/h with a positive voltage of 21 kV applied at the needle tip (high voltage AC to DC converter, Acopian) and the grounded collector (Dingtuo Technology) rotating at 500 rpm. After completion of PVDF layer, six mL of the PAN solution was electrospun at 0.3 mL/h and 15 kV, with all other fabrication parameters being identical to those described for PVDF. The resulting material was a composite containing 50 wt% PAN and 50 wt% PVDF. The two-layer polymeric composite was removed from the Al foil with tweezers to prevent tearing and used in subsequent processes (e.g., amidoximation) without any additional modification.

2.2.2 PAN with surfactants

Surfactants used to target uranium were HDEHP, Aq, and HDPA due to their previous uses for uranium extraction. Mats containing Aq or HDEHP were prepared with 7 wt% PAN and either 1, 2, or 3 wt% of Aq or HDEHP dissolved in DMF. The solutions were stirred at 60°C for 2 h at 700 rpm to ensure complete dissolution of the surfactants and a homogenous solution. Due to HDPA not being soluble in DMF, mats containing HDPA were prepared with 6 wt% PAN and either 0.5 or 1 wt% HDPA dissolved in DMSO. Again, the HDPA was dissolved by

stirring the solution at 60˚C for 2h at 700 rpm. All PAN mats modified with surfactants were electrospun using the same fabrication conditions described previously for layers of PAN on PVDF.

2.3 Amidoximation of polymeric mats

This protocol was originally reported in Horzum et al.[21] and optimized by varying temperature (20 or 30 ^{o}C), reaction time (24 or 48 hours), and solution exchanges (reacted in either one or two fresh solutions). A PAN-PVDF mat (2 g/L of mat, 1 g/L of PAN, ~0.65 cm^2/mL) was placed into a glass dish containing a solution of 15 g/L hydroxylamine hydrochloride (0.216 M) and sodium hydroxide (0.375 M) with the PAN side of the mat on the surface of the solution. A lid was placed on the glass dish, which was then placed into a 30 ^{o}C water bath for 24 hours. Afterwards, the mat was rinsed extensively with DI water to remove any remaining salts; all mats were rinsed until the samples of the wash water were at the same pH of DI water. Mats were then left to dry for 12 hours in air prior to use in any experiments.

2.4 Characterization of polymeric mats

Electrospun fibers were sputter coated with a thin layer of Au/Pd (Emitech Sputter Coater K550) and characterized by scanning electron microscope (SEM) (S-4800, Hitachi). Average fiber dimensions (e.g., diameter) were determined using ImageJ software, with at least 100 fibers imaged and measured for determination of averages (with standard deviation). Amidoximation of the PAN fibers was confirmed via Fourier Transform Infrared Spectroscopy (FTIR; Nicolet™ iS™ 50 FTIR Spectrometer) while PAN fibers with surfactants were also scanned to investigate their incorporation into the mats. The sample was loaded into the chamber and purged with dry

27

air and nitrogen. Single beam scans with 128 sample scans, 1 background scan, and a resolution of 2 cm^{-1} were taken. Specific pore volume (13-point analysis) and surface area (7-point analysis) were measured by N_2-BET adsorption isotherms on a Quantachrome NOVA 4200e Analyzer. Samples were degassed for at least 12 hours prior to analysis.

2.5 Uranium uptake experiments

2.5.1 Batch uptake

Sorption isotherms experiments were conducted in 50 mL plastic conical vials. Solutions were prepared by diluting a 1000 mg/L depleted uranium (SPEX CertiPrep) stock to concentrations of 0.1, 0.5, 1, 5 and 10 µM U. Depleted uranium is any uranium that has a mass percent of ^{238}U greater than that found in nature (99.28%). U uptake was monitored using a radiotracer, with a 3.5 Bq spike of ^{232}U (NIST traceable standard, Eckert & Ziegler) per 20 mL of solution. Chemical matrices consisted of either Milli-pure water, 10 mM HEPES, 500 mg/L Ca^{2+}, 500 mg/L HCO_3^- or Surine™ Negative Urine Control (Cerilliant). All solutions except for Surine™ were pH-adjusted to either pH 2 or 6.8 using 5 N NaOH or 5 N HNO_3. For Surine, uranium was added to the solution, which was then pH adjusted back to its ambient pH. After pH adjustment, the U-containing Surine was left to sit for 24 hours prior to use to ensure stability of U over time. Isotherms with HDPA- and HDEHP-modified PAN were collected at pH 2 while isotherms for Aq-modified PAN and AOPAN were collected at pH 6.8. Minimal pH drift was observed (<0.1 pH units) during the 16 hour reaction period. Mats were added to conical vials at a constant mass of 0.25 g/L (~0.25 cm^2/L) and incubated for 16 hours. Afterwards, mats were removed from the solution and analyzed for sorbed uranium content as described below.

28

Sorption isotherms were characterized by sorption models and parameters were fit to experimental data. Freundlich isotherms [$C_{sorbed} = K_f \cdot (C_{aq})^{1/n}$, where K_f is the Freundlich isotherm parameter an n is the degree of linearity], were linearized in excel and parameters calculated with linear regression at the 95% confidence interval.

Kinetic and pH edge experiments were conducted in identical systems to those described for isotherm experiments. Kinetic experiments were tested at an initial U concentration of 10 µM at either pH 2 (Milli-pure H_2O) or pH 6.8 (10 mM HEPES) for each respective binding agent. Mats were added to reactors and left to react for 0.2, 0.5, 1, 2, 8, and 16 hours prior to analysis.

For pH edge experiments, systems were assembled at initial pH values ranging between 2 and 7 (Milli-pure H_2O pH adjusted with 5M NaOH or HNO_3). Uptake of U as a function of pH was measured at initial U concentrations of 1 and 10 µM and reacted for 16 hours. The final pH value of each reactor was recorded to measure pH drift during incubation, which was typically <0.5 pH units. Reactors with pH's between 4 and 6 tended to show the largest amount of pH drift with minimal drift at pH 2-3 and 7.

2.5.2 Flow through uptake

The performance of select nanofiber mat formulations was also evaluated in a dead-end, flow-through filtration system (Figure 2-1) to simulate their application in water treatment. The filter holder (Cole-Parmer) had a 25 mm outer diameter with an active filtration area of 3 cm^2. Mats were cut to fit within this holder and typically weighed ~12 mg per layer of mat. Flow-through conditions were created using influent flowrates of 0.4 or 0.8 mL/min (80 or 160 LMH, respectively) driven by a 60 mL syringe (B-D) loaded on a syringe pump (New Era Pump

29

Systems, Inc.). Filters were pre-conditioned with 20 mL of a 10 mM HEPES solution (pH 6.8) followed by either 120 or 240 mL of a 1 µM U (0.24 ppm) solution in 10 mM HEPES at pH 6.8. Effluent was collected in 3 mL samples for every 10 mL interval of filtered solution.

2.6 Uranium analysis

2.6.1 Analysis of batch uptake

Initial solution's radioactivity concentrations were measured by adding 2 mL aliquots from each reactor and 10 mL of Ecolite scintillation cocktail (MP Biomedicals) into a 20 mL scintillation vial. Sorbed uranium was measured by removing the mat from the reactor and placing them into a 20 mL scintillation vial with 10 mL of Ecolite scintillation cocktail. Vials were shaken and left overnight to dark adapt (energy in scintillation cocktail from light is able to leave) and provide ample time for the polymer mats to dissolve in the scintillation cocktail. Samples were then counted on a liquid scintillation counter (LSC; Packard 1600CA Tri-Carb Liquid Scintillation Analyzer) for 40 minutes. The range of 100 and 2000 keV was used to exclude beta signals produced by daughter isotopes, ^{234}Th and ^{234}Pa.

2.6.2 Flow through uranium analysis

Uranium samples were acidified with 2% HNO_3 (trace metals grade, Aldrich) and filtered with 0.45 µm filters prior to analysis on an Agilent Technologies 7900 ICP-MS. Argon was used as the carrier gas in low matrix mode and no collision gas. Masses 7, 89, and 205 were used for tuning of the machine prior to running calibration standards and samples in triplicate. ^{209}Bi was used as the internal standard at a concentration of 10 ppb.
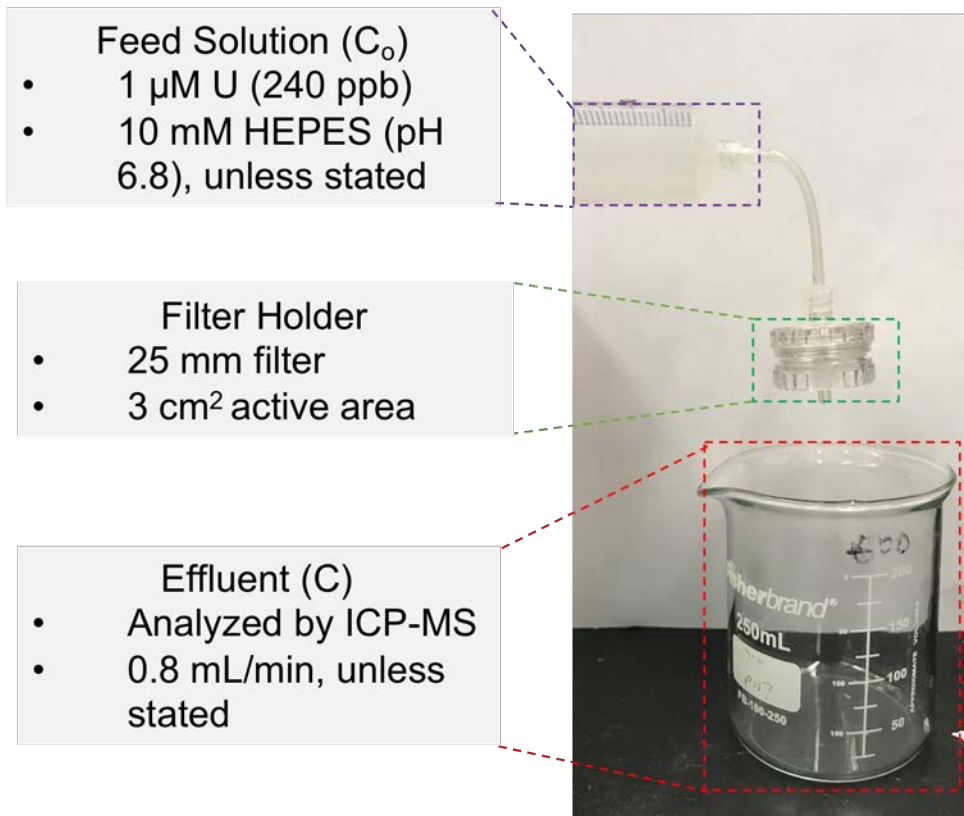
Figure 2-1. Flow through experiment setup with the feed solution (purple), filter (green), and effluent (red) depicted.

CHAPTER 3: SYNTHESIS AND PERFORMANCE OF ELECTROSPUN POLYMER MATS FOR URANIUM CAPTURE

3.1 Synthesis details

The functional binding agents used, shown in Figure 1-5, all created soluble and homogenous sol gels in polyacrylonitrile (PAN) except for hexadecyl phosphonic acid (HDPA). Upon heating, mixtures of HDPA and PAN formed a clear solution, but HDPA was relatively insoluble and precipitated, creating a heterogeneous, but stable, suspension when the mixture was cooled to room temperature. Due to the insolubility of HDPA in DMF, DMSO was required as a solvent to create a sol gel. Upon dissolving PAN in DMSO (vacant of HDPA) a stable sol gel was created, even when cooled, confirming that the addition of HDPA is causing the instability of the sol gel.

During electrospinning, mats containing Aliquat® 336 (Aq) would deposit over a wider area than unmodified PAN, under otherwise identical synthesis conditions. Because the same amount of sol gel was used both with and without Aq, this resulted in Aq-containing mats that were thinner than unmodified PAN. In contrast, inclusion of HDPA and bis(2-ethylhexyl) phosphate (HDEHP) created mats that deposited over a smaller area than unmodified PAN, producing HDEHP-containing mats that were generally thicker.

Hereafter, materials will be denoted as 'PANx-SURFACTANTy', where x and y denote the wt% of PAN and the surfactant in the sol gel, respectively. PAN dissolved in either DMF or DMSO will be denoted by a 6 or 7, respectively. PAN7 in DMF created more flexible mats whereas PAN6 spun in DMSO typically created slightly stiffer mats which was an artifact of the solvent used and not relating to the wt% of PAN in the sol gel. This difference in flexibility is similar to the results reported by Kizildag et al, which found that PAN mats spun with DMSO

had higher breaking stresses relative to mats produced in DMF (breaking stresses of 10.58 for

DMSO mats versus 1.56 MPa for DMF mats, respectively).[56]

3.2 Characterization of synthesized nanofibers

All synthesized materials were further characterized to determine their physical and

chemical properties and ensure reproducibility across synthesis methods and batches (e.g., day to

day variations). Characterization included Fourier Transform Infrared Spectroscopy (FTIR) to

verify the identity of the polymer and confirm the presence of integrated functional groups   In

addition, the nanofiber morphology and diameter was examined via scanning electron

microscopy (SEM) and specific surface area and pore volume measurements for each material

were conducted via N_2-BET isotherm analysis.

3.2.1 Morphology of nanofibers

The particular solvent (DMF or DMSO) used for the electrospinning process resulted in

changes in the morphology of the nanofibers. When DMF was used as a solvent, all mats were

synthesized as smooth fibers and exhibited no beading (Figure 3-1). DMSO exhibited more

variability from batch to batch with a majority of nanofiber batches possessing smooth and bead-

free morphologies whereas a small subset of fabrication attempts displayed beading (ball and

chain like structure). Morphological differences between spinning with DMSO instead of DMF

may be attributed to different solution properties, such as volatility and viscosity, which has

previously been shown to affect morphology of electrospun nanofibers.[33] At room temperature

(20 ^{o}C), DMSO has a lower vapor pressure than DMF (0.42 mmHg compared to 2.7 mmHg,

respectively)[25] while PAN exhibits higher viscosity when dissolved in DMSO than DMF (4.48 to

0.53 Pa-s, respectively).[57] The lower vapor pressure of DMSO and increased viscosity should create smaller fibers as well as reduce beading.[58]

Harder to control environmental parameters, such as relative humidity (RH) may also alter the ability to consistently synthesize homogeneous fibers.[33] The RH was monitored during electrospinning of the PAN and modified PAN fibers was consistently measured at 16%. Unfortunately, the RH gauge available in the laboratory reports a minimum RH value of 16%, followed by 3% intervals from 21 to 80%, meaning the actual RH could have been below 16% or up to 21%. It is important to monitor changes in RH because this environmental variable can inhibit solvent evaporation and an increase in RH can results in larger nanofiber dimensions and pore volumes.[58] Grothe et al. previously demonstrated that RH was the most critical parameter when spinning PAN in DMSO because mats could not be synthesized if the RH value rose to a certain threshold, although the RH when this occurred was not reported.[59]

Amidoximation of PAN fibers caused no change in the nanofiber morphology, which is similar to observations reported by Horzum et al.[21] This may be a result of the post-synthetic modification, which only impacts the surface of the polymer nanofiber. The inclusion of HDEHP and Aq into PAN also resulted in smooth fibers. The addition of charged surfactants has been previously shown to increase sol gel conductivity which helps in decreasing nanofiber sizes and reducing beading although Peter et al. has shown that at higher surfactant loadings (~15-40% wt/ wt PAN) these benefits can be negated due to increased viscosity which offsets the benefits from a more conductive sol gel.[40] Aq fibers typically produced hair-like structures (denoted by white arrows in images), which became more prominent as the surfactant wt% was increased.

34

3.2.2 Nanofiber dimensions

Diameters of the nanofibers produced with DMF were determined via SEM imaging of 100 fibers (Figure 3-2). PAN7 creates fibers with the smallest diameter at 110 ± 20 nm, where these values represent the mean and standard deviation from SEM sizing analysis. Nanofiber diameters were unchanged after amidoximation (110 ± 30 nm) and uranium uptake (120 ± 20 nm). This invariance in nanofiber diameter after functionalization and U capture was also previously reported by Horzum et al.[21]

Unlike with amidoximation, changes in nanofiber diameter were observed upon the introduction of surfactants. Inclusion of Aq and HDEHP into PAN mats produced an increase in nanofiber diameter compared to that of unmodified PAN (Aq-containing nanofibers ranged from 130 ± 40 to 160 ± 30 nm, while HDEHP-containing nanofibers ranged from 150 ± 30 to 190 ± 40 nm). Addition of surfactants changes the physicochemical properties (e.g., viscosity, conductivity, and surface tension) of the precursor solution, which ultimately influences the morphology of the resulting fiber. For example, relatively low (<1 wt%/ wt sol gel) mass loadings of surfactants have been shown to improve sol gel conductivity and decrease bead formation and nanofiber diameters.[60] At higher mass loadings of surfactants, these benefits can be negated due to increased viscosity.[61]

DMSO-based precursor solutions produced similarly sized nanofibers. For example, SEM imaging of PAN6 revealed a mean diameter of 110 ± 20 nm. With the inclusion of HDPA into the sol gel with DMSO, there was no apparent change in nanofiber diameter (HDPA-containing fibers had diameters of 120 ± 20 nm).

3.2.3 Surface area and pore volume

The specific surface area and pore volume for select materials was determined by N_2-BET isotherms (Table 3-1). The specific surface area and pore volume of all materials were similar (ranging between 15 to 21 m^2/g for surface area and 27.7 to 39 10^{-3} mL/g for pore volume) except for that of PAN7-HDEHP1. The surface area for PAN7 remained the same after the amidoximation process, which is expected as only the polymer backbone is changed during the post-synthetic reaction. The inclusion of Aq and HDPA into PAN mats resulted in little to no change in its specific surface area compared to unmodified PAN, but inclusion of HDEHP surfactant resulted in a decrease, although the reason is unknown and merits future investigation. Specific surface areas and pore volumes for unmodified PAN mats (synthesized in DMF) from Peter et al. were 18.8 ± 0.3 m^2 g^{-1} and 0.045 ± 0.005 mL g^{-1}, respectively, which are similar to the results found here.[62]

3.2.4 Infrared spectra of polymer mats

FTIR spectra of PAN7, AOPAN7, PAN7-HDEHP1, PAN7-Aq1, and PAN6-HDPA0.5 are shown in Figure 3-3, with analysis of functionalized materials for U capture providing evidence of either amidoximation or surfactant inclusion. As a baseline for comparison, the FTIR spectra of PAN7 has aliphatic peaks at 2940 cm^{-1} and 1460 cm^{-1}, along with a characteristic peak at 2400 cm^{-1} associated with the C$\equiv$N stretch.[21] The band at 1670 cm^{-1} is not observed in the FTIR spectra of the PAN polymer provided by the manufacturer (Sigma Aldrich), suggesting this feature may be attributed to a C=O stretch from residual DMF left within the polymer matrix or from natural oxidation of nitrile to carbonyl.[63–65]

Amidoximation was confirmed with the addition of a broad band between 3000-3700 cm^{-1} after functionalization, which is indicative of stretching from -NH$_2$ and -OH groups. Further, a peak appearing at 1610 cm^{-1} can be attributed to the formation of -NH$_2$ groups while the peak at 1670 cm^{-1} may be attributed to the formation of –C=N or from carbonyl groups due to oxidation of nitrile or residual DMF.[21,63–65] This spectral characterization of amidoximated PAN is consistent with FTIR results also obtained by Horzum et al.[21]

The incorporation of all surfactants (HDEHP, Aq, and HDPA) resulted in the appearance of a band at 2850 cm^{-1} that can be assigned to the asymmetric stretch of -CH$_2$. This peak does not appear in the spectrum of unmodified PAN and has been used previously to identify Aq and HDEHP in a polymer matrix of polyvinyl chloride (PVC).[66] Aq has strong bands from symmetric stretching of –CH$_3$ and –CH$_2$ between 2956 and 2926 cm^{-1}, respectively, but these cannot be distinguished from PAN at a similar wavelength.[66] Unique to HDEHP is a strong absorption band at 1034 cm^{-1} that originates from the bending of the -C-O-P- bond.[66] FTIR spectra of free octadecyl phosphonic acid (2 carbon atoms longer than HDPA) shows characteristic and strong intensity bands at 3795 and 1324 cm^{-1} that corresponds to –OH and P=O stretching, respectively.[67] Notably, these bands were not found with the inclusion of HDPA, which produced no new spectral features compared to that of unmodified PAN.

Some characteristic spectral features of these surfactants (e.g., hydroxyls in HDPA and HDEHP) may not be present in the IR spectra due to their low abundance (8-15% wt /wt PAN) in the polymer, which would lead to a weak signal and low signal to noise. Accordingly, additional spectra were collected on samples with at highest surfactants loadings (≥20 wt% / wt PAN). However, these spectra (not shown) only resulted in greater intensities of asymmetric stretching from –CH$_2$ in all surfactants and the –C-O-P- band from HDEHP, but no new

37

characteristic peaks of the surfactant were observed in the spectra collected at these elevated
mass loadings.

3.3 Performance of materials in batch systems

3.3.1 Kinetic uptake

Kinetics studies were conducted to determine rates of uranium uptake on each material
and the time necessary to achieve sorption equilibrium (i.e., when solution phase concentration
no longer changes over time) (Figure 3-4). All materials showed relatively rapid uptake over ~2
h. Time to equilibrium for each material varied, with Aq and HDEHP mats reaching equilibrium
at 2 hours and AOPAN achieving steady-state near 16 hours. HDPA followed a much slower
period of uptake and never reached equilibrium during the course of the experiment. After 16
hours, the sorbed fraction of U bound to the mats decreased in the order of HDPA > AOPAN >
HDEHP > Aq, where the total percent of uranium removed from the aqueous phase was ~90, 75,
45, and 25%, respectively.

Prior studies with AOPAN nanofibers showed similar uptake rates (1 g mat L^{-1}; initial
uranium concentration of 100 mg/L; pH 4) in batch systems, with rapid uptake in the first 1.3 h,
followed by equilibration after 3 hours.[68] Similarly, phosphate functionalized polyethylene
nanofibers also had similar uptake rates compared to our HDPA-functionalized materials (0.2 g
mat L^{-1}; initial uranium concentration of 50 mg/L; pH 8.2), with rapid uptake in the first 6 hours
and maintained sorption percent at any longer reaction periods.[69]

3.3.2 Effect of uranium uptake with varying pH

Materials were tested over a broad pH range (2-7) spanning conditions representative of acid mine drainage to surface and ground waters. These studies were conducted to establish the materials' treatment efficacy for uranium removal as a function of the speciation of both the surface functional groups of embedded binding agents and soluble uranium. Environmentally relevant uranium concentrations of 1 and 10 μM^6 UO_2^{2+} (Figure 3-5) were used throughout all of the sorption experiments.

At an initial U concentration of 10 μM (Figure 3-5A), HDPA mats exhibited high uptake (>60% of total U) over the entire pH range. The highest uranium removal with HDPA-functionalized materials occurred at pH 2 (~95%) while the lowest uptake was at pH 5 (~60%). AOPAN achieved relatively low removal at pH 2 (~40%), but U removal increased with pH, producing relatively high and constant removal between pH 3 and 7 (~80%). HDEHP-containing mats exhibited opposite behavior relative to AOPAN; its highest uptake at pH 2 (~50%), but U removal decreased rapidly at pH 3 (< 20%) and was maintained at this low level for all pH values above 3. Finally, Aq-containing materials exhibited the lowest removal overall (between 0-15%), but U uptake did modestly increase with increasing pH values.

At an initial U concentration of 1 μM (Figure 3-5B), different U removal trends were observed for some, but not all, materials. Trends in pH-dependent U uptake at 1 μM were comparable to those observed at higher initial U for HDEHP- and Aq-containing materials. Once again for HDEHP, the best performance occurred at pH 2 (~50% U removal) followed by much lower but constant removal (< 10%) at pH 3 and above. Likewise, Aq-containing mats exhibited low but steadily increasing removal with increasing pH, although a higher maximum percent removal was obtained at 1 μM of initial U (30% removal) compared to the 15% removal

39

at an initial U of 10 µM. It should be noted that even though the percent of uranium removed at the lower U concentration was greater than that of the higher U concentration, the total mass removed (and thus sorbed on the mats) was greater at the higher U concentration ($\sim$1 µg/mg) than at the lower U concentration ($\sim$0.3 µg/mg).

In contrast, AOPAN and HDPA-containing mats exhibited different pH-dependent performance at low initial U relative to high initial U systems. For AOPAN, this difference was only observed at higher pH values (pH >5). Specifically, whereas removal was relatively constant ($\sim$80%) above pH 5 in high U systems, uptake decreased steadily from pH 5 ($\sim$80%) to pH 7 ($\sim$40%) in low U systems. A much greater difference in performance between low and high concentration U systems was observed with HDPA. While HPDA removal at 10 µM U was always greater than 60%, removal in low U systems was a maximum at pH 2 ($\sim$50% U) and decreased steadily until pH 4 ($\sim$10%), above which uptake was negligible.

We propose that the difference in performance between low and high U systems for AOPAN and HDPA-containing mats reflect removal via surface precipitation at high U concentrations. For AOPAN, we suspect this precipitation is driven by the relatively high pH and elevated near-surface concentration of U on the nanofibers (recall, differences in performance were only observed above pH 5). For HDPA, evidence of precipitation is observed across a wider pH range. Uranyl phosphate complexes are known to have very low $\log K_{sp}$ values (-49.00 to -53.33)[70] compared to that of hexavalent uranyl hydroxides (-21.75 to -24.10)[71] and uranyl carbonates (-13.29 to -14.91),[70] which enables uranium phosphates to precipitate in even acidic solutions. This behavior has been seen before with phosphate-functionalized TiO_2, where an insoluble sodium autunite ($NaUO_2PO_4$) complex formed after uranium sorption in acidic solutions (pH 2).[52] The mechanism of uptake was described as a combination of absorption and

40

surface complexation that shifts to surface precipitation; this scenario seems consistent with the likely removal mechanism on HDPA mats.[52]

For nanofibers without evidence of surface precipitation, trends in pH-dependent removal lend insight into the mechanism of U binding on the functionalized nanofiber. For example, while HDEHP performs similarly at both high and low initial U concentrations, its sorption capacity is reduced considerably above pH 3. HDEHP has a pKa of 1.47,[72] and thus will become increasingly more deprotonated at pH 2 and above. Notably, while HDEHP become more anionic from pH 2 to 3, U removal decreases from 50% to ~10% over this same pH range. Thus, U removal does not appear to proceed via a purely electrostatic mechanism (i.e., positively charged UO_2^{2+} bound by negatively charged HDEHP sites). This means that U uptake can occur by exchange of H^+ during uranyl coordination which has been previously observed.[73] Also, hydrolysis of UO_2^{2+} should not be affecting uranium uptake with HDEHP because hydrolysis products are not abundant until pH 4 for solutions containing 1 or 10 µM U(VI) (Figure 3-6). As a final consideration, the chemical differences between HDEHP and HDPA may provide insight regarding the mechanism of uranium uptake. HDEHP is a phosphonate that contains only one hydroxyl group available for uranium binding, whereas HDPA has multiple hydroxyls that allow it to chelate and precipitate uranium similar to the phosphate anion.

At both low and high U, Aq mats resulted in a slight increase in uranium uptake as pH increases. This behavior likely reflects that the uptake of Aq is dependent on the fraction of anionic uranyl species present in solution. Aq is positively charged across the pH range investigated, and as a strong base ion exchanger, it has been shown to scavenge negatively charged uranium species from high ionic strength acid mine wastes.[47] We therefore hypothesize that anion exchange is the main mechanism for uptake of uranium on Aq mats, but further

41

verification of this mechanism is warranted. In fact, for pure aqueous systems, anionic uranyl species (e.g. $UO_2(OH)_3^-$) should not be formed until ~pH 7 (Figure 3-6). Furthermore, while negatively charged species can form in the presence of carbonate (e.g., $(UO_2)_2CO_3(OH)_3^-$ can form as early as pH 4), these anionic carbonate species are only produced at dissolved CO_2 concentrations higher than those in our current systems.[74] Nevertheless, because increased uranium removal on Aq mats typically occurred as early as pH 3, the dissolved U speciation may not be entirely understood in our experimental system or an unknown mechanism of uptake is at play.

For AOPAN, the binding mechanism for uranium to amidoxime is still widely disputed, with arguments for either monodendate (binding with either N or O) or bidentate (binding to both N and O) complexes in prior investigations.[75] Pekel et al. suggested that deprotonation of the imine group was important for chelation to uranyl by exchange of H^+ with UO_2^{2+} while Hirotsu et al. reported that ligand exchange (and ion exchange of H^+ depending on pH) occurs during uranyl uptake when it is accompanied with a ligand.[76,77]   In both high and low U systems at pH 2, similar uranium removal occurs (~ 40%) with 100% of the uranyl species being UO_2^{2+} (Figure 3-6) suggesting that the high H^+ concentration competes with UO_2^{2+} in the amidoxime group. A decrease in the H^+ concentration (increase in pH) allows for UO_2^{2+} to compete with H^+ in the amidoxime site which results in ~80% U removal between pH 3 and 5 at both high and low U concentrations. It should be noted that in the high and low U concentrations tested (1 and 10 µM) hydrolysis of UO_2^{2+} starts at pH 4 and is no longer the dominant species by pH 5. In higher concentrations, insoluble $UO_2(OH)_2 \cdot H_2O$ is the dominant species by pH ~5.5 which may be precipitating on the surface as seen at pH 6 and 7 with U removal of ~80% still. This is contrasted with low initial U concentrations in which U removal is reduced with increasing pH

(~ 70% at pH 6 and ~40% at pH 7). The decreased uptake may be indicative of speciation changes that occurs beyond pH 5 where UO_2OH^+ is the dominant form at pH 5 and 6 (~50% and ~40% of total U, respectively) followed by $UO_2(OH)_2 \cdot H_2O$ at pH 7 (~90% of total U). Since ligand exchange is expected to occur in these regions, the lower uptake may also be due to slower kinetics involved with ligand exchange.[77] Based on the results herein it seems that uranyl uptake is pH dependent at pH 5 and below, where UO_2^{2+} competes with H^+, while being speciation dependent at pH's greater than 5 due to hydrolysis products of UO_2^{2+}.

We note that IR spectra were also collected after uranium uptake experiments (not shown) to explore the nature of bound uranium on each mat. Unfortunately, this analysis did not produce any signals specific to uranium. This is likely attributable to FTIR being a bulk analytical approach, while most of the uranium is expected to be bound on the nanofiber surface. For example, even at the highest sorbed uranium content we observed, the final mass of uranium on these mats represents between 0.1 and 1 wt% of the total mass (sorbent plus U) available for analysis. Thus, the majority of the signal generated during FTIR analysis is associated with the bulk polymer and functionalization agents because they comprise the majority of the system mass.

3.3.3 Materials capability for uranium capture over varying uranium concentrations

Sorption isotherms (Figure 3-7) can be useful for determining a material's capacity and the appropriate models (e.g., Langmuir and Freundlich) that can be used to describe their behavior as a sorbent. Materials were tested over a range of uranium concentrations that varied from just below its MCL in drinking water (0.1 µM) to the more extreme levels of uranium contamination that may be present in some affected water resources (10 µM).[6] HDPA and

43

HDEHP were both tested in acidic conditions (pH 2) because those are the conditions where they exhibited the best performance. Isotherm experiments with Aq and AOPAN were conducted at a pH of 6.8, as these conditions are more representative of surface and drinking water samples while also being a pH that both Aq and AOPAN performed well in.

Overall, a trend of increasing solution phase U concentration resulted in a nearly linear trend of increased sorbed U concentration for all materials. This linear trend lacks a clear plateau which is used as an indicator of monolayer sorption, an assumption made for Langmuir isotherms. Consequently, this lack of plateau results in the maximum sorbed uranium content on the mats to occur at the highest initial uranium concentration (10 μM) which gave 4.4, 7.5, 1.4, and 6.1 μg/mg mat for HDEHP-, HDPA-, Aq- and AOPAN mats, respectively. In comparison, these sorbed uranium loadings are dramatically lower compared to capacities reported for other nanofiber mats. For example, AOPAN nanofibers with a PS core shell had a maximum sorbed content of 137 μg/mg (1 g mat L^{-1}; initial uranium concentration of 100 mg/L; pH 4)[68] and phosphate functionalized polyethylene had a maximum sorbed content of 176.6 μg/mg (0.2 g mat L^{-1}; initial uranium concentration of 50 mg/L; pH 8.2).[69] The similarity in these materials to AOPAN and HDPA synthesized herein suggests that greater uranium uptake can occur, although testing in similar conditions is required obtain a plateau that shows our materials are reaching a form of capacity. Strong base anion exchangers, similar to Aq, have not been used for uranium uptake in nanofibers but show high uptake in resins at ~50 μg/mg in groundwater (initial uranium concentration of 1,200 ug/L; pH 6.5; flow through system).[47]

In order to model these systems, Freundlich isotherms were fit to the data to determine their model parameters (Table 3-2). The Freundlich isotherm model [$C_{sorbed} = K_f \cdot (C_{aq})^{1/n}$, where K_f is the Freundlich isotherm parameter and n is the degree of linearity] is an empirically derived

model and can be used to describe either mono- or multilayer sorption mechanisms. The parameters for the Freundlich isotherms have relatively high standard deviations, which may be from the relatively small number of concentrations (n = 5) used to construct isotherms.   Due to the linearity of uptake of the isotherm (i.e. uptake percent stayed relatively the same across all concentrations) all materials seem to be best described by the Freundlich model although testing at higher U concentrations may give better insight into what model fits best since no plateau was formed which can aid in guiding model fits.

3.4 Performance of materials under dead end filtration conditions

Break through curves, plotting normalized U concentration (i.e., effluent concentration normalized to influent concentration; C_{out}/C_{in}) as a function of volume of water treated (Figure 3-8), were used to examine how functionalized nanofiber mats perform under flow conditions more representative of water treatment. Complete breakthrough occurs when the effluent concentration is equal to that of the influent ($C_{out} = C_{in}$), which means either that the materials are saturated (i.e., all binding sites are occupied and thus not capable of removing any more uranium) or that timescales for U uptake on the remaining available surface sites are far slower than the residence time for U in the mat system. With an influent concentration of 1 μM U (238 μg/L) at pH 6.8, we note that any normalized concentration above ~0.1 would be considered above the MCL for uranium. The fluxes used ranged from 80 to 160 LMH (0.4 to 0.8 mL/min; 3 cm^2 active area) which was at the high range for ultrafiltration (80 LMH) and low end of microfiltration (160 LMH). To increase the mass of the filters used for treatment, thicker filters were created by stacking extra layers of material with the same effective filtration area, thereby increasing the residence time for U-containing influent within the nanofiber mat.

45

For AOPAN, the lowest mass tested did not show complete breakthrough but produced approximately constant, incomplete removal of U (C_{out} ~0.6C_{in}). Increasing the mass of AOPAN (from 13 mg to 26 mg by adding a second filter layer) resulted in near complete removal of uranium. In contrast, while all Aq mats had an initially brief period of good uranium removal (C_{out} < ~0.1C_{in}), effluent concentration levels for U rapidly increased thereafter to a level near complete breakthrough (with C_{out} > 0.8C_{in}) after 15 to 40 mL of treated water volume. This general trend was observed even at higher Aq filter masses or at lower water flux (both of which increase contact time between U and Aq mats). Meanwhile, HDPA mats removed more than 90% of the U under the same flow through conditions as AOPAN (11.5 mg verse 13 mg). We note that for all materials tested, the effluent concentrations were quantifiable and above that of the detection limit for ICP-MS, meaning that complete removal of U(IV) was not observed for any mat under flow.

Based on these results, U uptake on AOPAN appears kinetically limited under our experimental conditions. At lower mass (13 mg), breakthrough is effectively steady-state; complete saturation of the filter did not occur (i.e., there was always some residual capacity for U removal), but effluent U concentration was not zero nor was it changing over time. At the conclusion of the experiment, the mass of U captured on the filter was 0.87 µg/mg at 120 mL treated water, which is well below the maximum sorbed concentration of 6.1 µg/mg observed in batch isotherm experiments. This suggests that AOPAN materials still have considerably more sites available for U binding. When more mass is added to the filter (from 13 mg to 26 mg) then the contact time between the U-containing solution and the AOPAN increases, which results in near-complete removal of U from the 120 mL sample volume. A second run of a 26 mg filter over 240 mL of water treated revealed that AOPAN was still able to remove more than 90% of

46

the influent uranium. This sample still hadn't reached saturation and contained the highest sorbed content of U on AOPAN (2.62 µg/mg) which is ~40% of the max uranium sorption found in batch (6.1 µg/mg). This suggests that AOPAN mats are kinetically and not capacity limited.

Aq mats were more susceptible to higher effluent concentrations relative to AOPAN. When the effluent concentrations did stabilize, they usually remained between 80 and 90% of the influent concentration. Increasing the mass of the mats (from 12 to 24 mg) resulted in the effluent concentration reaching 90% of the influent concentration at a later treated volume (from 20 mL to 40 mL), corresponding to an increase in total U removed from 5.4 to 6.2 µg. When the mass of the filter was held constant (at 24 mg), but the flowrate was decreased (from 0.8 mL/min to 0.4 mL/min), the effluent concentration decreased from 90 to 80% of the influent concentration, which occurred after 40 mL of treated solution volume. This corresponds to a slight increase in the total mass of U removed from 6.2 at higher flow to 6.6 µg at lower flux.

We also explored the importance of the Aq loading in the PAN mat (from Aq1 to Aq2) on U binding in flow through systems. The higher Aq loading resulted in the effluent concentration reaching 90% of the influent concentration at the same volume of water treated (20 mL) although at 60 mL of treated volume it dropped and stabilized to 80% of the influent concentration until 120 mL of volume was reached. Thus, the total U removed increased from 5.4 to 6.0 µg. For all the conditions tested, sorbed uranium content was between 0.26 and 0.47 µg/mg, which is below the maximum found in batch of 1.4 µg/mg and suggests that U-binding sites are still available on the surface of the mats. It can be seen for Aq materials that total U removal can be increased by increasing the mass of the mats, or Aq loading in the polymer, or by decreasing the flowrate. Changing any of these variables results in longer contact times between

47

the U-containing solutions and the active sites from Aq in the polymer mats. This suggests that the materials may exhibit a kinetic limitation in flow through systems.

HDPA removed more than 90% of the uranium when used in the same conditions as AOPAN (11.5 mg verse 13 mg). This is indicative of a uranium loading of 2.73 µg/mg, which is below the 7.5 µg/mg observed during batch sorption experiments. This suggests that the material is either not kinetically limited or uranium is precipitating on the surface, which should exhibit rapid uranium removal. In batch systems, minimal uranium uptake (Figure 3-6) is expected to occur at these concentrations (1 µM U; pH 6.8) whereas higher U concentrations (10 µM) resulted in surface precipitation. This suggests that under flow conditions surface precipitation may be able to occur at lower initial uranium concentrations compared to that of batch.

Similar to batch systems, competing ions and the presence of ligands have the potential to interfere with uptake in flow conditions. Thus, water quality effects were also tested in which Ca^{2+} (competing ion) or CO_3^{2-} (uranyl ligand) were added to the system to evaluate their impact. For AOPAN, the presence of Ca^{2+} and CO_3^{2-} seemed to have no influence on the removal of uranium. In both chemical matrices, the higher masses of mat (~26 mg) were used to ensure there were no kinetic limitations and it was found that breakthrough never occurred during the 120 mL treated volume. Sorbed uranium from the Ca^{2+} and CO_3^{2-} runs were nearly identical to the experiments performed in the absence of competing ions, with U contents of ~1.2 µg/mg for all three trials. The lack of interference from Ca^{2+} and CO_3^{2-} may due to the actual chemical complexation of uranium on the surface of the mats as opposed to electrostatic interactions that could potentially be impacted by co-solute ions. It should also be noted that the pH of the solution varied from 6.8 to 7.5 over the course of experiments containing the CO_3^{2-} anion,

suggesting that HCO_3^- may have been scavenged by AOPAN during the run by either amidoxime

or nitrile groups.
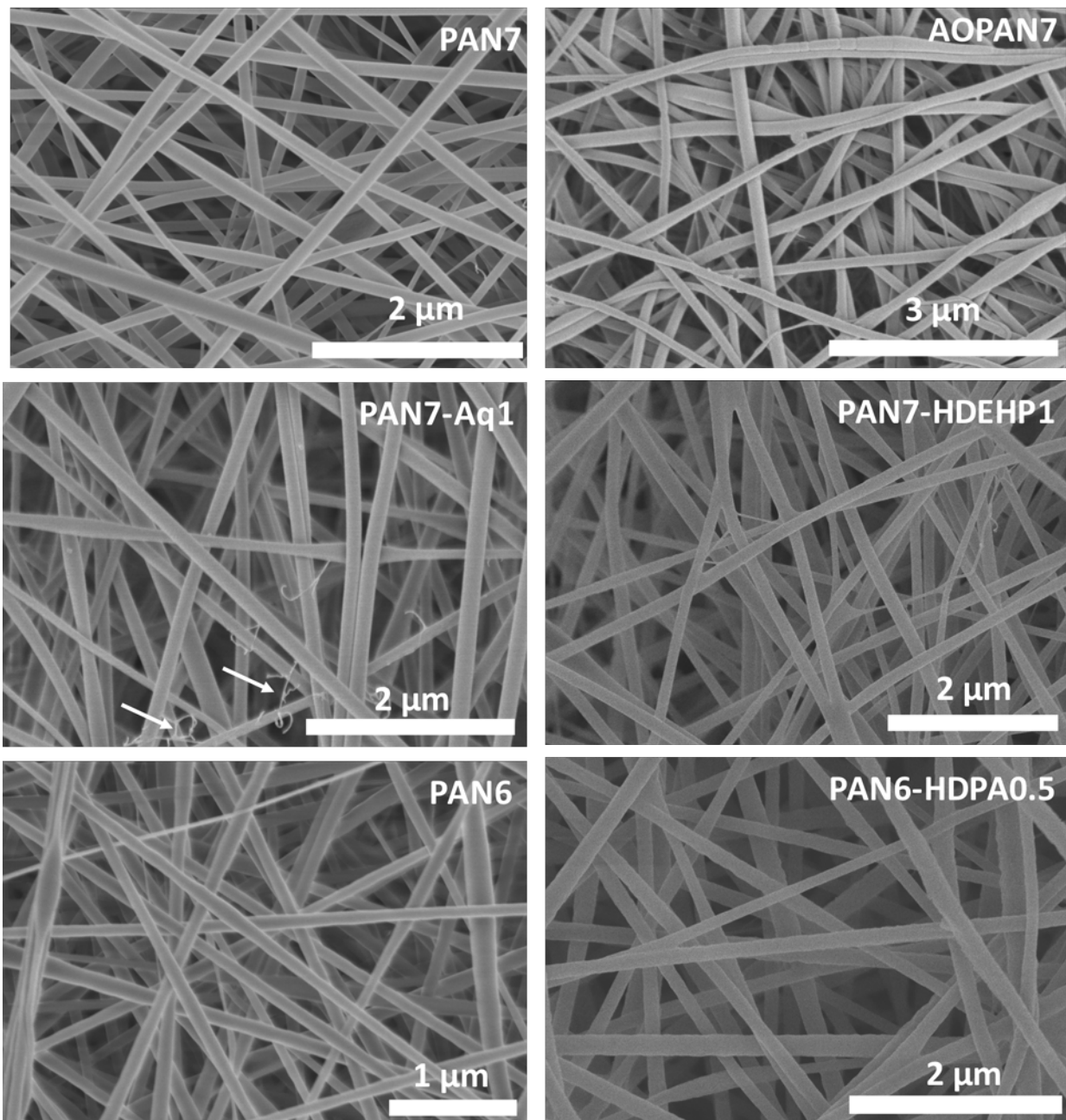
Figure 3-1. Representative SEM images of synthesized nanofibers. Arrows denote "hair-like" structures that were present in Aq-mats.
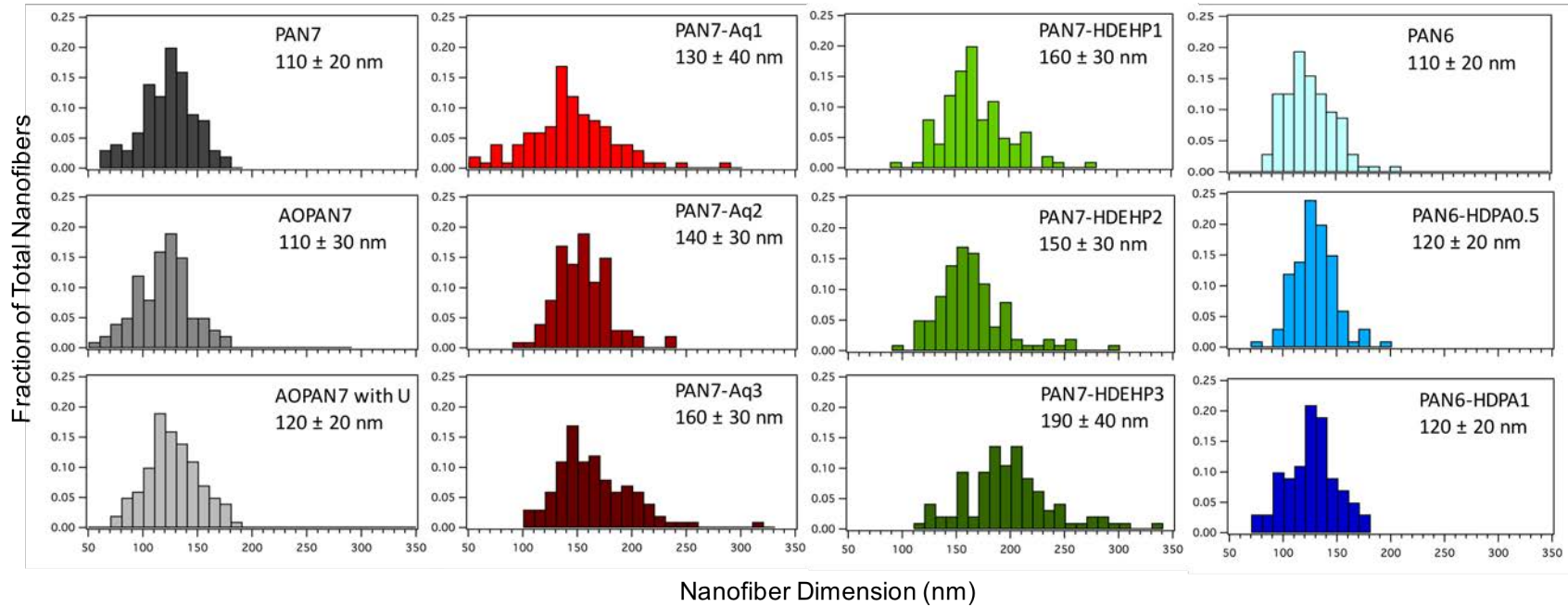
Figure 3-2. Histogram of nanofiber dimensions (bin size of 10 nm) analyzed by ImageJ with images taken via SEM. During analysis ≥100 nanofibers were measured with the average and standard deviation reported.

Table 3-1. N_2-BET measurements to determine specific surface area (m2/g) and pore volume (mL/g) of select materials. Average and standard deviations from duplicate measurements

Mat	Surface Area (m^2/g)	Pore Volume $(10^{-3}\ mL/g)$
PAN7	16.3 ± 0.7	-
AOPAN7	16.3 ± 0.6	-
PAN7-Aq1	16.5 ± 4.0	27.7 ± 3.3
PAN7-HDEHP1	11.0 ± 4.5	12.6 ± 5.0
PAN6	21.1	39.0
PAN6-HDPA1	15.1	30.6
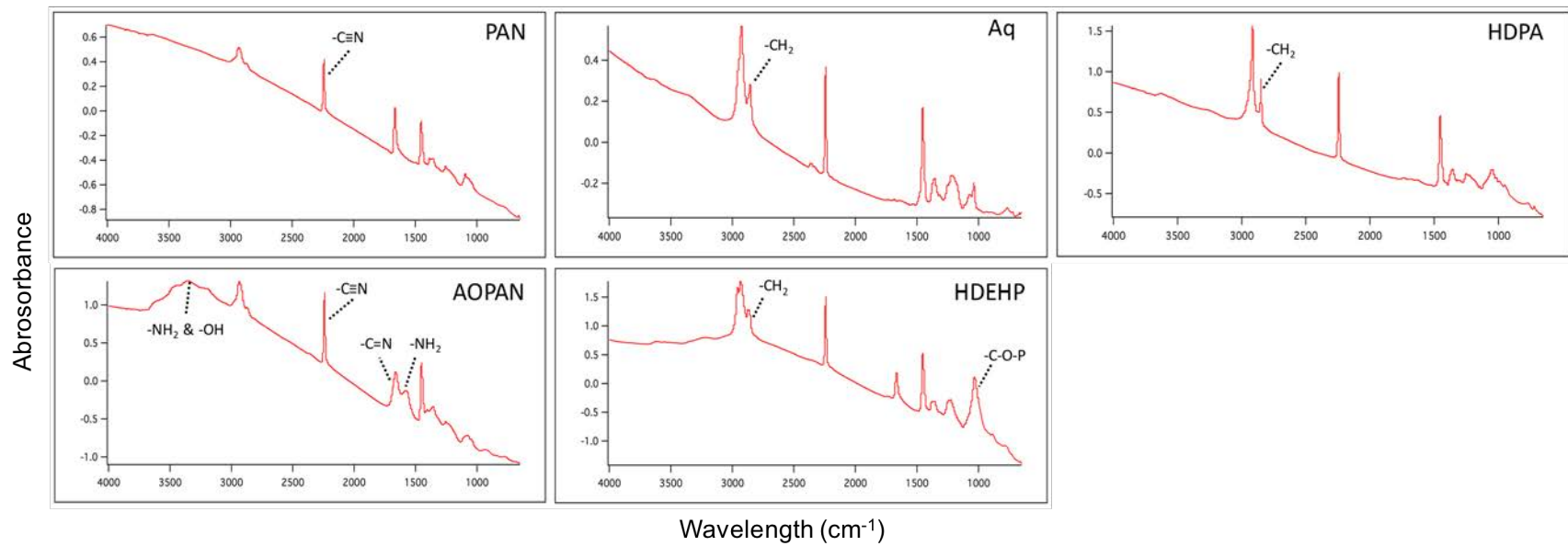
Figure 3-3. FTIR spectra of synthesized polymer mats. Key features associated with each material are identified.
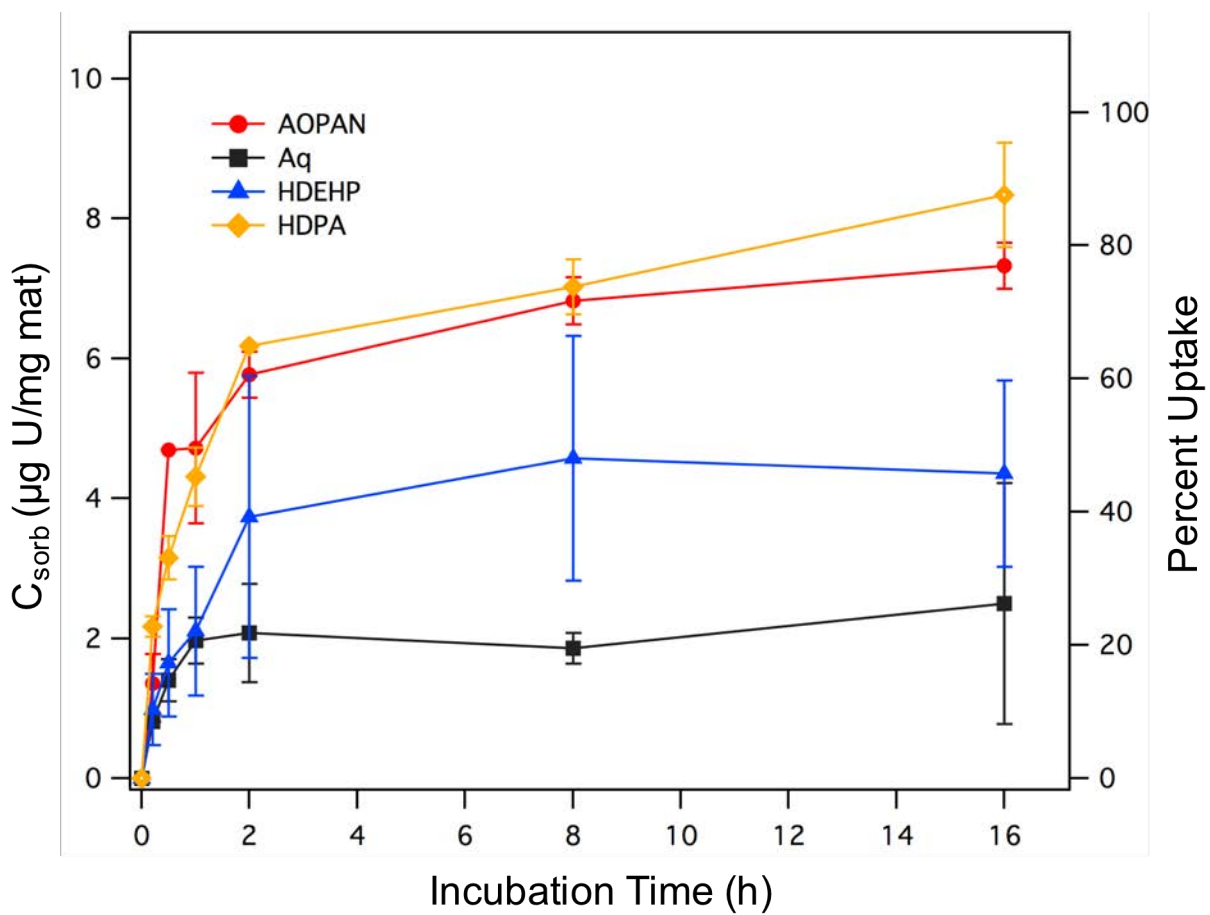
Figure 3-4. Sorbed uranium concentration as a function of time. All materials were tested at an initial concentration of 10 µM U. Aq and AOPAN experiments were conducted in 10 mM HEPES at pH 6.8, while HDEHP and HDPA experiments were conducted in water acidified to pH 2 with HNO_3. Uncertainties from standard deviation of duplicate experiments. Mass loadings used were 0.25 g L^{-1}.

54
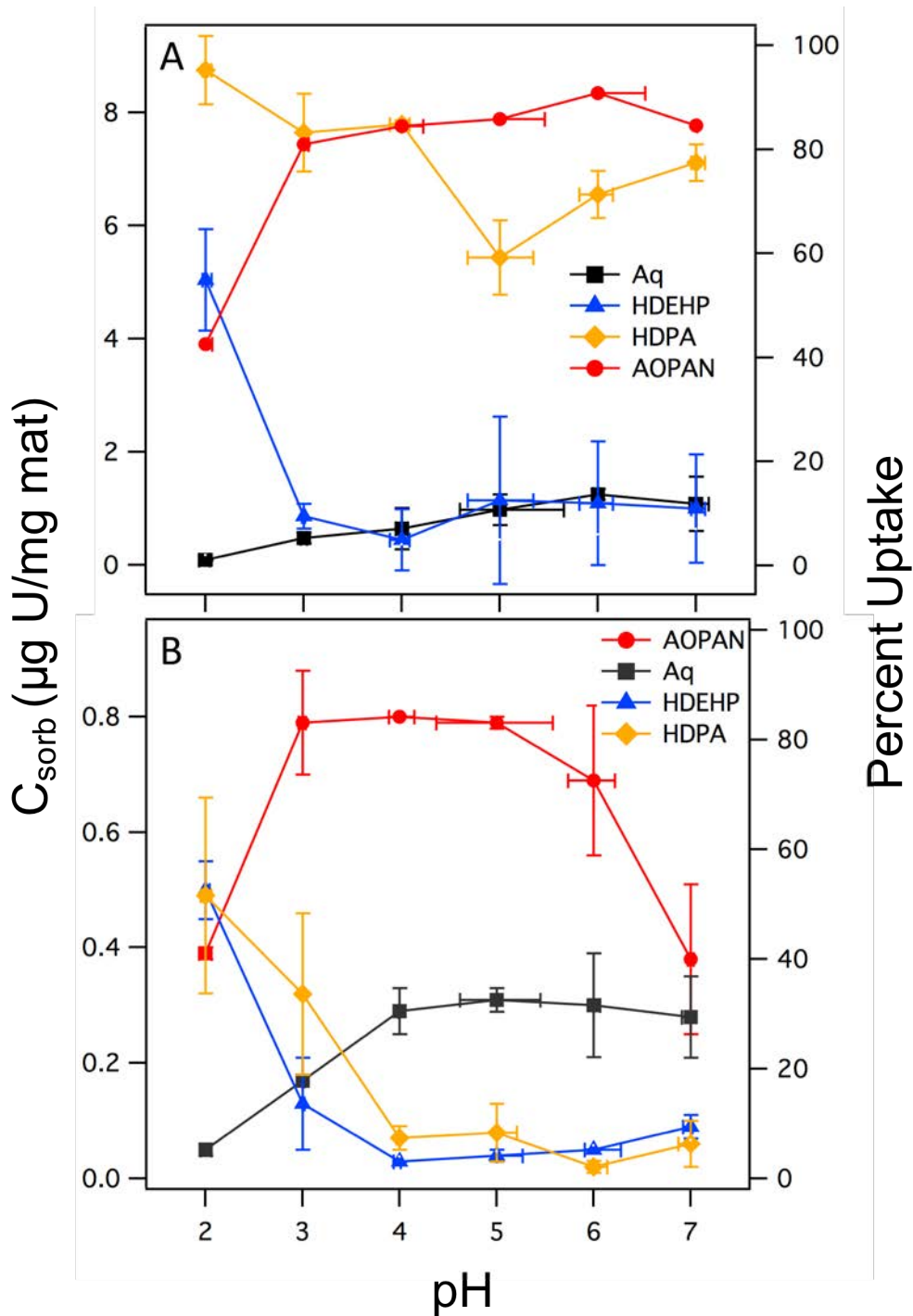
Figure 3-5. Sorbed uranium concentration as a function of solution pH at an initial uranium concentration of (A) 10 µM U and (B) 1 µM U. All materials were tested in water (pH adjusted with 5 M NaOH or HNO₃). Vertical error bars reflect standard deviation of duplicate trials while horizontal error bars represent the range of pH drift observed over the course of the experiment (~ 16 h). Mass loadings used were 0.25 g L⁻¹.
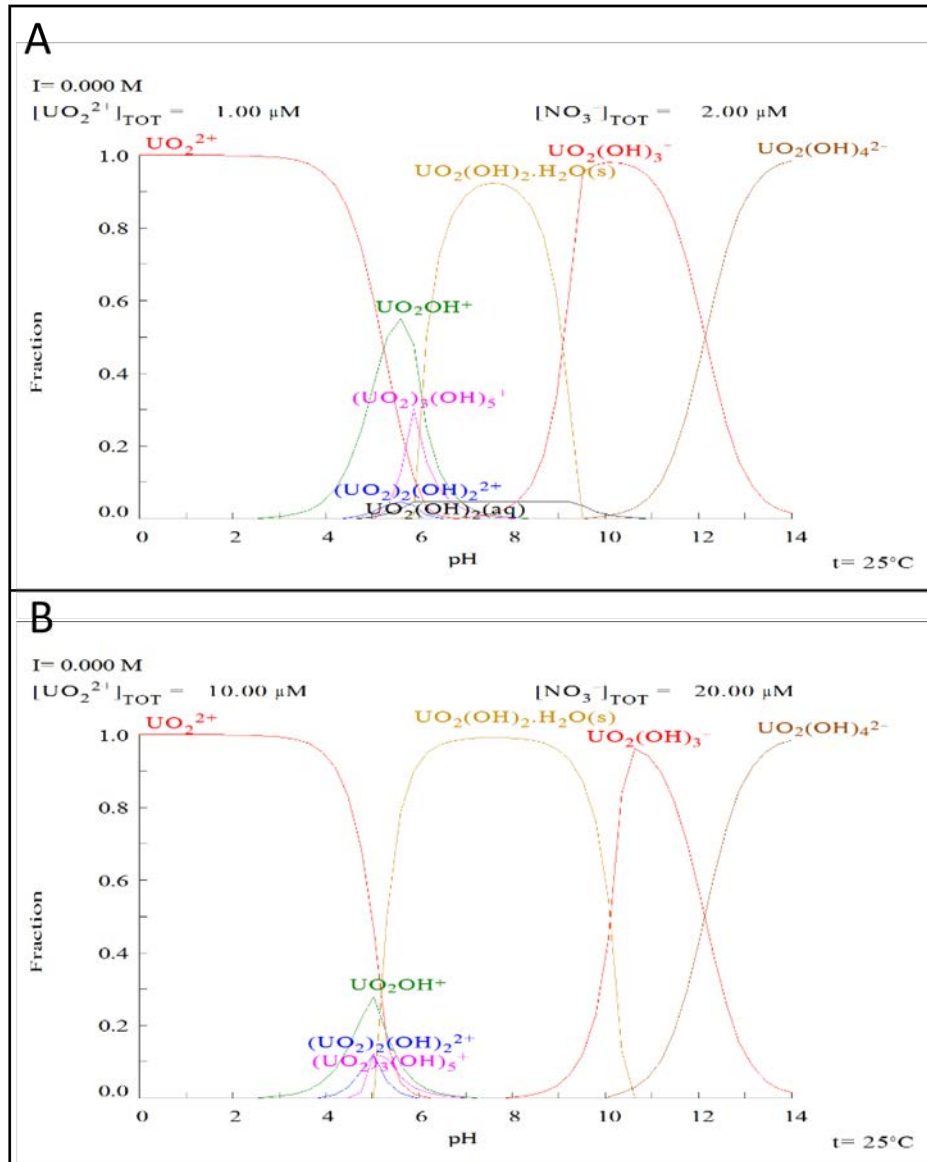
Figure 3-6. Uranium speciation diagram for uranium in water at (A) 1 µM and (B) 10 µM produced with Medusa software. Graphs reproduced with permission from Nate Parizeck.
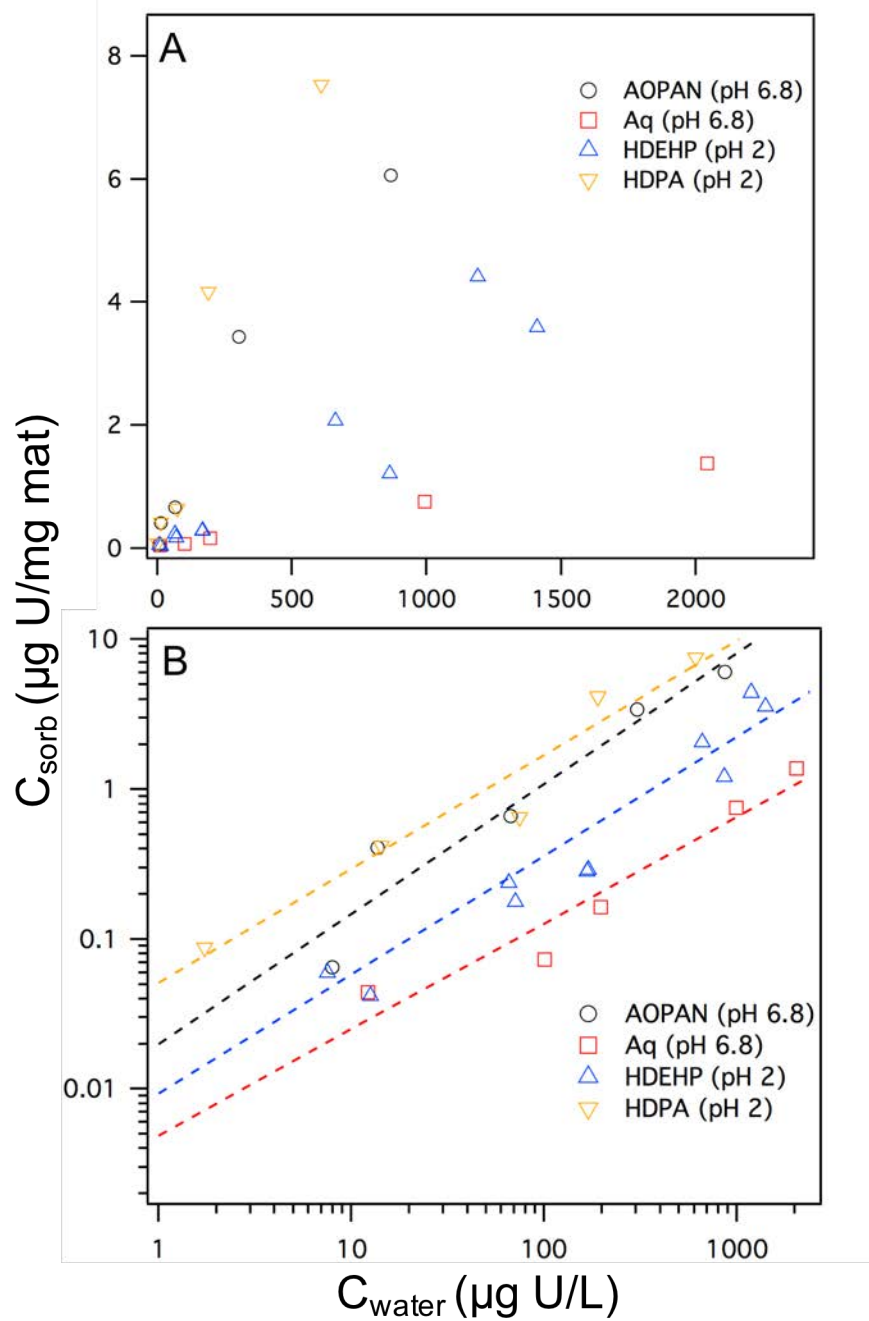
Figure 3-7. Sorbed uranium concentration verse solution
concentration (A) at equilibrium. Sorption isotherms were conducted
in either 10 mM HEPES at pH 6.8 (Aq and AOPAN) or in water
acidified to pH 2 with HNO_3 (HDEHP and HDPA). Freundlich
equation fits (B) shown for each material, with model fit parameters
summarized in Table 3-2. Mass loadings used were 0.25 g L^{-1}.

57

Table 3-2. Freundlich isotherm parameter fits and standard deviations determined at the 95% confidence interval. K_f is the Freundlich isotherm parameter and n is the degree of linearity.

Freundlich			
Material	$\log K_f$ $(\mu g\ U/g\ mat)/(L/\mu g\ U)^{1/n}$	1/n	R^2
AOPAN	-1.7 ± -0.9	0.87 ± 0.47	0.921
Aq	-2.3 ± -0.9	0.71 ± 0.36	0.929
HDPA	-1.3 ± -0.7	0.76 ± 0.35	0.942
HDEHP	-2.0 ± -0.4	0.79 ± 0.15	0.949

58
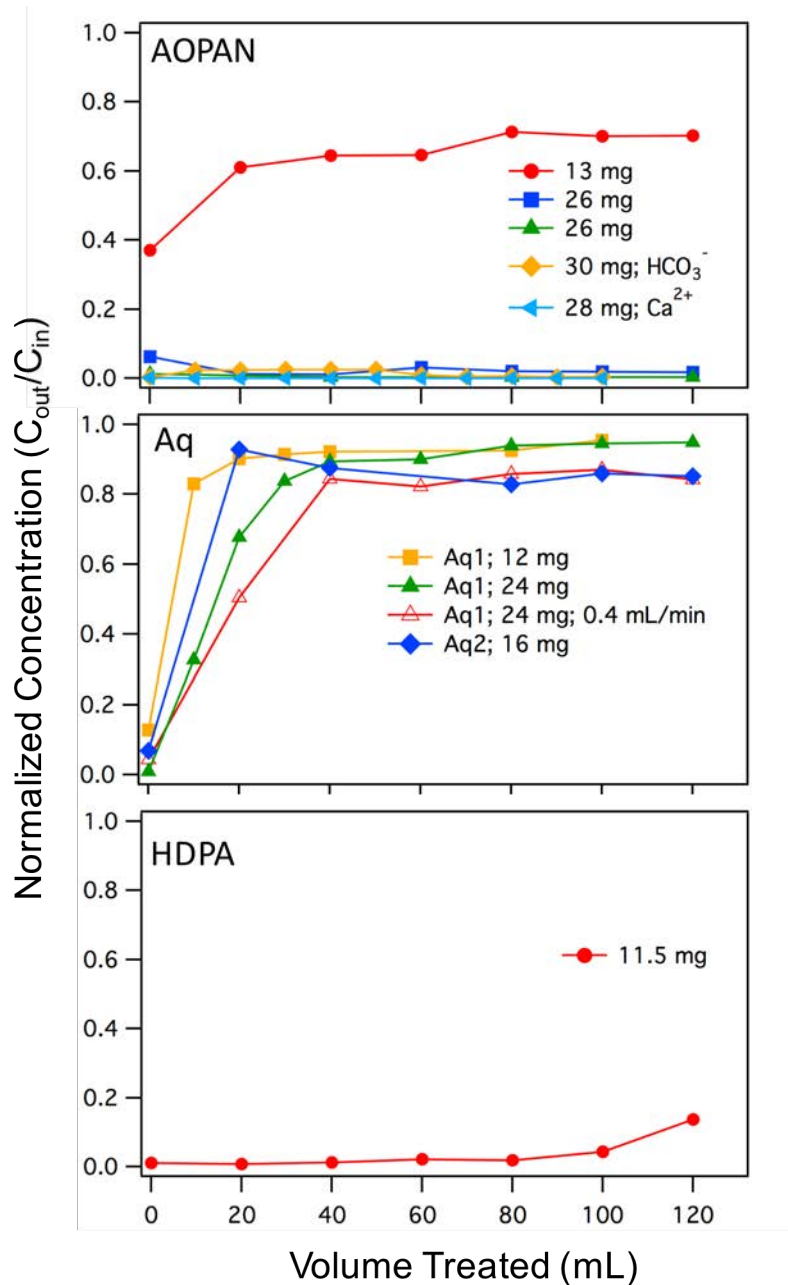
Figure 3-8. Normalized concentration (effluent concentration divided by influent concentration) of uranium over the volume treated in a dead-end filtration setup at an influent concentration of 1 μM in 10 mM HEPES (pH 6.8) and a flowrate of 0.8 mL/min (160 LMH), unless otherwise stated.

CHAPTER 4: CONCLUSIONS

4.1 Project summary

Work conducted herein has helped to illustrate the promise of functionalized electrospun polymer nanofiber mats for capturing uranium from water and (more generally) aqueous-based systems. Electrospun nanofiber mats have long been touted as low-cost yet robust materials for sorption of inorganic and organic species from aqueous solutions, with widespread applications in sensor developing[37–39], bio scaffolding[35,36], and water treatment[33,34]. By modifying the composition of electrospun polymer nanofiber mats, we show here that uranyl $(UO(VI)_2^{2+})$ can be specifically targeted for capture in drinking water, as well as biologically relevant media (e.g., see evidence of U capture from synthetic urine in Figure A-2C). Broadly, these findings address the overall goal of this thesis to develop polymer mats exhibiting enhanced U(VI) removal for applications in point of use (POU) water treatment and as a platform for concentrating otherwise dilute U concentrations to improve detection limits of next-generation sensing approaches (e.g., surface enhanced Raman spectroscopy, or SERS).

There are several notable outcomes of the research conducted herein. In Chapter 3, mechanically stable nanofiber mats were synthesized in reproducible fashion, both with respect to the properties of nanofibers, which were extensively characterized, and their performance toward U uptake driven by functional groups added as part of material fabrication. Several formulations of nanofibers were considered, including:

- *Amidoximated polyacrylonitrile (or AOPAN):* AOPAN nanofiber mats were synthesized and amidoximation confirmed by vibrational spectroscopy. Small nanofibers were synthesized (~110 nm) that results in a high surface area material (16 $m^2\,g^{-1}$), which is advantageous since uranium capture is a surface based process.

- *Surfactant-modified nanofibers*: Aliquat® 336 (Aq), hexadecyl phosphonic acid (HDPA), and bis(2-ethylhexyl) phosphate (HDEHP) were embedded into the mats at varying wt% while also keeping nanofiber diameters relatively small (~200 nm or less). Again, this creates high specific surface area mats (between 11 and 21 $m^2 g^{-1}$) which allows for a more surface reactive material. Inclusion of all three surfactants was confirmed with vibration spectroscopy.

After fabrication, performance testing of these materials in batch and flow through systems gave insight into their potential ability to remove uranium in various conditions. In batch systems, these materials were tested over a range of environmentally relevant uranium concentrations (between 0.1 and 10 µM U)[6], pH values and timescales to evaluate their efficacy and mechanism responsible for U capture. Key outcomes of performance testing are summarized below:

- *Kinetics*: All materials showed rapid uptake within 2 hours. Equilibrium was reached with Aq- and HDEHP-containing mats in 2 hours, AOPAN in 16 hours, and HDPA not reaching equilibrium in the 16 hour reaction period but removed ~95% of uranium (initial U concentration of 10 µM). The rapid uptake exhibited by these materials is desirable for both sensing and POU treatment applications. For sensing, it reduces the time required to concentrate uranium and thus reduces detection time while for treatment it means that uranium capture can occur rapidly which is vital for the low contact times experienced in flow conditions.

- *pH edge*: All materials were tested in environmentally relevant pH's between acid mine drainage to groundwater (pH 2-7) and at high and low U concentrations (1 and 10 µM, respectively). HDEHP and Aq performed similarly at high and low concentrations while

HDPA and AOPAN had varying performance depending on the U concentration. At the high and low concentrations, HDEHP's max uptake occurred at pH 2 (~50%), decreased at pH 3, and maintained below <10% at pH's higher than 4. Aq followed a general trend of increasing uptake with increasing uptake, which ranged from 0-15% at 10 μM U and 0-30% at 1 μM U. HDPA performed well over the entire pH range at high U concentrations (10 μM) at 60% removal or above. At lower initial U concentrations HDPA followed the same trend as HDEHP with maximum uptake at pH 2 (~50%), decreased at pH 2, and maintained below <10% at pH's higher than 4. At high initial U, AOPAN had low uptake at pH 2 (~40%) but maintained ~80% U removal at pH 3-7. At the lowest U concentration, AOPAN followed a concave curve trend with 40% uptake at pH 2, 80% between pH 3-5, and 40% uptake between pH 6-7. These experiments gave useful insight into the potential mechanisms at play (described below).

- *Isotherms*: When testing the materials at their optimal pH (pH 2 for HDEHP and HDPA) or relevant pH of ground water (pH 6.8 for Aq and AOPAN) a nearly linear isotherm was observed (U concentrations of 0.1, 0.5, 1, 5, and 10 μM) which exhibited no plateau. This suggests that the materials can afford to remove more uranium from solution than what was seen in the highest uranium concentration tested (10 μM U) which gave sorbed U contents of 4.4, 7.5, 1.4, and 6.1 μg/mg mat for HDEHP-, HDPA-, Aq- and AOPAN mats, respectively. Although further tests need to be conducted to ensure more uranium can be sorbed, the potential to sorb more uranium could allow for lower detection limits in sensing and extended performance of materials in flow through systems for POU treatment.

- *Mechanism:* Based on the pH edge experiments (summarized above) several types of mechanisms seem to be at play. For HDPA, the discrepancies between U uptake at high and low U concentrations suggest that surface precipitation is occurring. This may be significant for long-term removal in POU treatment since it may create highly insoluble U complexes which resist dissolving back into solution but can impact sensing which will lack speciation information. With AOPAN, either monodentate or bidentate chelation appears to be the mechanism at play although it can't be distinguished within this study which, if any, is the primary form of binding. At high enough U concentrations, surface precipitation may also be occurring at higher pH's (6-7). Chelation is ideal for both sensing and POU applications as it is the least susceptible to interferences from co-solutes in solution. HDEHP seems to undergo cation exchange (removal of H^+ during uranium capture) which is not impacted by uranium concentration but is highly dependent on pH. This limits its performance to only acidic conditions which may make it useful when probing concentrations of uranium in abandoned mines. Finally, Aq is most likely undergoing anion exchange (uranyl exchanging with Cl^-) for uranium capture. For sensing, anion exchange allows for more speciation data to be unlocked which can be valuable information. In terms of POU treatment, anion exchange requires anionic uranyl for removal which is ideal since uranyl is mostly $UO_2(CO_3)_2^{2-}$ and $UO_2(CO_3)_3^{4-}$ in ground water which is expected to be readily removed by anion exchange.

In flow through systems, AOPAN removed U(VI) even in the presence of competing calcium and carbonate ions, which are common to many drinking water sources (e.g., ground water) and effluent uranium concentrations did not exceed the MCL over 0.13 liters (with ~30 mg of filter material), which suggests that saturation of the available surface sites did not occur

63

for this membrane. The material was kinetically limited, meaning increasing the flux will require more mass to obtain sufficient contact time for removal of U. Assuming that an average person drinks 2 L/day, only ~180 g of filter material would be required to treat their annual drinking water requirement. Comparatively, Aq mats showed immediate uranium retention, followed by uranium in the effluent stabilizing to 80-90% of the influent concentration. This phenomenon occurred regardless of the Aq loading in the mats, mass loading, or flowrate used in experiments, suggesting that uranium removal is dependent on the contact time. Over all of the conditions tested the sorbed U loading ranged between 0.26 and 0.47 µg/mg, which is below the maximum found in batch of 1.4 µg/mg, suggesting that active sites are still available. HDPA mats removed uranium to 10% of the influent concentration during the first 100 mL of the flow-through experiment while the last 20 mL of effluent had U concentration greater than 10% of the influent. This high U removal may be indicative of surface precipitation because high uranium sorption was observed under flow conditions (2.6 µg/mg; 0.1 g mat L^{-1}) which was not observed when under similar conditions in batch uptake experiments (0.17 µg/mg; 0.25 g mat L^{-1}). For all materials tested with the flow-through configuration, the sorbed U(VI) content on the mats was below the maximum found in batch, suggesting that further removal may be afforded in these systems.

The results herein suggest that these materials can concentrate U(VI) from aqueous systems and, thus, may be viable as a platform in sensor development and POU water treatment technologies. For sensing applications, these mats are capable of concentrating uranium while also removing chemical matrix interferences, which should allow for lower detection limits and improve their economic viability. AOPAN has already been shown to be applicable for detection of uranyl in combination with SERS (Appendix A) even in complex matrices such as

urine. Aq may be useful for gaining more detailed speciation information and the electrostatic bond should allow for easier coordination to AuNS, although its lower sorbed uranium content may not allow for lower detection limits. HDPA's surface precipitation makes it not ideal for sensing, while HDEHP's chelation to uranyl may make it useful for sensing of uranium in acid mine drainage. For applications in POU water treatment, the AOPAN and HDPA mats were capable of removing uranium to levels below the MCL, although more complex matrices still need to be considered, in some cases. Aq mats did not reach acceptable levels of removal for water treatment, although more environmentally relevant conditions and uranyl species (e.g. carbonate present) may result in better removal than that observed herein.

4.2 Future work

This study was successful in developing materials for removing uranium from water but questions remain regarding material capacities in batch systems, U(VI) sorption in both batch and flow through systems, and performance of materials under real-world conditions. Answering these questions would be valuable for the further optimization of the performance of these materials for uranium capture.

In batch systems, questions regarding material capacities, influence of co-solutes and competing ions, surfactant leachability, and reversibility merit future investigations. Material capacities may be determined by increasing the mat loading (decreasing mat mass used with same volume) or by increasing the initial uranium concentration, although concerns may arise regarding the formation of surface precipitates and speciation if the level is too high. For mats containing surfactants, determining U(VI) capacities could investigate the relationship between surfactant loading in the polymer and the materials capacity. This would provide additional

65

information for developing electrospun polymer nanofibers with the maximum U(VI) concentration potential. Leachability of surfactants should also be investigated, as a materials capacity may decrease from removal of surfactant and loss of surface active sites. Reversibility of uranium binding should also be evaluated to give insight into the reusability of materials and strength of U(VI) sorption.

There are also lingering questions on the mechanism of uptake, specifically for Aq and HDPA mats. In Aq mats, multiple experiments can be done to probe if anion exchange is occurring such as using competing counter ions, making solutions dominated with anionic uranyl species and by measuring the release of chloride (anion present in Aq). By adding counter ions (either during uranium uptake or after) the contribution of electrostatic verse non-specific binding can be determined for Aq. For example, materials can be regenerated with both HCl, NaCl or NaHCO$_3$ to determine the impact of cations (H$^+$), anions (Cl$^-$) or ligands (e.g., CO$_3^{2-}$) on U binding.[42] The importance of the overall charge on the uranyl complex can be evaluated by adding U(VI) to chemical matrices known to produce predominantly negatively charged species (e.g. carbonate or oxalate). Chloride concentrations in water can also be measured with ion chromatography to see if there is a release of chloride (anion present in Aq) over time that coincides with uranium uptake. The ratio of chloride release to U sorption could then be evaluated to provide additional insight into the extent to which anion exchange sites are occupied by U, and the type of binding of surface species that result (e.g., some ions have been known to occupy two adjacent exchange sites).[40] HDPA mats with suspected surface precipitation (batch systems; 10 µM U) can be characterized using X-ray diffraction (XRD) or X-ray photoelectron spectroscopy (XPS) to explore and potentially identify any specific solid phases generated via

66

precipitation. Identification of the solid U(VI) phases will provide additional insight into the solubility and reversibility of the U(VI) sorbed to the surface of the polymer mats.

Initial studies with the flow-through system suggested U(VI) sorption, but a huge determinant of their efficacy will be the presence of competing ions that can alter uranium uptake. Although synthetic, complex matrices can be developed to evaluate these systems, the ultimate test of the materials performance is to use either uranium spiked tap water or samples from the Navajo Nation. Testing breakthrough conditions in these systems will be required to determine the effectiveness of the system and the potential use of these materials for POU applications. Due to the different mechanisms at play, it may also be of worthwhile to test multiple of these materials in series for a multi-targeted approach that may allow for greater U removal. For example, Aq mats could be added first to target anionic uranyl species followed by HDPA or AOPAN which can chelate any remaining uranyl of non-anionic charge.

Appendix A: Matrix-independent SERS Detection of Uranyl using Electrospun Amidoximated Polyacrylonitrile Mats and Gold Nanostars[1]

A.1 Introduction

Hexavalent uranium (U), found in contaminated soils and water as the uranyl cation (UO_2^{2+}), presents a significant biological, chemical, and radiological threat,[4,78] as chronic exposure promotes adverse health effects in at-risk populations. Uranium is a naturally-occurring, radioactive element that decays by alpha emission ($t_{1/2} = 4.5 \times 10^9$ years) and is a wide-spread contaminant in the southwest United States where U concentrations in unregulated water sources can routinely exceed the US EPA maximum contaminant level (30 µg/L U) by as much as five fold. [4,78] From a public health perspective, this chronic environmental exposure to U is concerning because it is a documented nephrotoxin, negatively impacts DNA repair, disrupts regulation of transcription factors and gene expression, and promotes apoptosis thus increasing the risk of cancer and other health problems.

Uranium detection in environmental and biological samples is the first step towards addressing public health concerns and environmental remediation of impacted lands, but there are issues with the complex nature of the matrix. In general, uranyl speciation in a biological or environmental sample is dynamic and complex and depends on the abundance of other ions, organic ligands, solid surfaces, and pH.[79–82] This complexity leads to problems in separations and data analysis; thus, samples are often altered using concentrated acids or separated using multi-step, time intensive columns and precipitation reactions.[83–86] After these pre-treatment steps, traditional radiometric and analytical detection methods, such as alpha spectroscopy and mass spectrometry, provide excellent detection limits to quantify solution species but require

---

[1] Manuscript submitted to Analytical Chemistry

expensive equipment and trained personnel. Thus, new approaches for simple and rapid detection of U from complex matrices are needed.

Raman spectroscopy is an attractive alternative method for U detection because the symmetric stretch associated with the uranyl bond is readily detectable from 870-800 cm^{-1}. Furthermore, the vibrational frequencies of this bond are sensitive to inner sphere ligand coordination, providing additional speciation information, and spectral signal can be acquired in minutes.[87–91] Normal Raman spectroscopy, however, is limited by the inherently small Raman cross sections associated with molecules so must be used in conjunction with enhancement methods to achieve detectable signals. For instance, normal Raman signals can be enhanced by 2-9 orders of magnitude[92–94] using surface-enhanced Raman scattering (SERS).

SERS detection of uranyl is feasible[95–100] but limited by the inherent non-specific adsorption of other molecules on SERS-active substrates[101] as well as the previously discussed complex and dynamic speciation of uranyl present in a complex sample matrix.[95–99] For instance, humic acid was shown to coordinate with uranyl affecting its speciation in solution, which in turn, reduced the adsorption of uranyl to silver SERS substrates. This resulted in lower detectability of uranyl using SERS.[100]

In the current study, we demonstrate the development of a SERS-based method for the detection of U in buffer and in the presence of environmentally-relevant confounding ions or synthetic urine by utilizing electrospun, amidoximated (AO) polyacrylonitrile (PAN) mats to extract U from solution and Au nanostars to enhance spectral signals (Figure A-1). The key advancement of this approach is the use of AO-PAN mats to initially isolate and pre-concentrate U from complex matrices followed by SERS detection directly on the polymer mats. By doing

69

so, Raman spectra become simplified and matrix effects minimized thereby providing fast, reproducible, and quantitative detection of uranyl from complex matrices.

A.2 Materials and methods

A.2.1 Fabrication, functionalization, and characterization of electrospun PAN mats

Detailed descriptions[102–105] of the fabrication and functionalized of the electrospun mats are found in Appendix B. Briefly, polymer mats are prepared step-wise by first spinning a polyvinylidene fluoride (PVDF) support layer onto a grounded drum collector. The PAN layer is subsequently electrospun on top of the PVDF. Once removed from the drum, nitrile groups in the polymeric mats are converted into amidoxime groups using reduction by hydroxylamine.[106,107] After functionalization, the mats are rinsed with DI water until the pH of the rinse water is less than 7, placed on parafilm (PAN side up), dried for at least 12 h in air at room temperature, and stored at room temperature until use.

Scanning electron microscopy (SEM) is used to characterize the morphology and average fiber diameter of the polymer mats. Electrospun fibers are sputter coated with Au/Pd (Emitech Sputter Coater K550) then imaged using a Hitachi S-4800 SEM. Fiber diameter is analyzed using Image Pro. At least 100 measurements are used.

A.2.2 Uranyl uptake and validation

Uranyl sorption is evaluated using 1 μM-10 mM U solutions by adding known amounts of a 1000 mg/L depleted uranium (SPEX CertiPrep) stock solution and 85.0 μL of ^{232}U radiotracer (LSC measurements only; 3.5 Bq, NIST traceable standard, Eckert & Ziegler) in 10 mM HEPES (pH 6.8; adjusted using 5 N NaOH or HCl), 3.4 mM $CaCl_2$, 5 mM $NaCO_3$, or 20

70

mL Surine™ Negative Urine Control (Cerilliant). These solutions were chosen to reflect co-solutes and concentrations typical of U-containing ground water samples. Five mg of the amidoximated composite mat (dry weight) is added to these solutions and incubated for 18 hours. Each experiment is performed in triplicate with appropriate controls. Uranyl uptake is confirmed using liquid scintillation counting (LSC) and normal Raman microscopy (see Appendix B).

A.2.3 SERS measurements and analysis

SERS measurements are collected using 6-mercaptohexanoic acid (6-MHA) functionalized Au nanostars. Previously reported protocols are used to generate these materials,[51] which are described in detail in Appendix B. The functionalized Au nanostars are stored at concentrations of 0.3 nM in 5 mM EPPS until use. Immediately prior to use, the materials are concentrated to 8 nM using centrifugation (2000×g; 40 min) and dispersed in an 80% ethanolic solution.

Nanostar structure is evaluated using transmission electron microscopy (TEM). A JEOL JEM-1230 TEM equipped with a Gatan CCD camera and a 120 keV acceleration voltage are used. Small volumes (10 μL) of the nanostars dispersed in 50% ethanol are deposited on 400 mesh copper grids coated with Formvar and carbon (Ted Pella). At least 100 Au nanostars are analyzed using Image Pro to evaluate the radius of curvature of the nanostar tips and the overall average sizes.

SERS measurements are collected using the same microscope setup used for normal Raman measurements. AO-PAN mats are diced into 3 mm x 3 mm squares. Next, 1 μL of the ethanolic Au nanostar solution is added every ~2 minutes until 10 μL of the solution is deposited

on the mats, which are then allowed to equilibrate for 10 minutes. Mats evaluated in a hydrated state are placed on a microscope slide (PVDF side down) and covered by 50 µL water. A coverslip is carefully placed over the hydrated mats so that no air bubbles are visible. Alternatively, mats are placed on a microscope slide (PVDF side down) and placed in a lyophilizer for 24 hours prior to analysis. All measurements are collected using 785 nm excitation and at ambient conditions (20 °C and 30-40% relative humidity). Hydrated samples are collected using a 10x objective, power = 25 mW, and t_{int} = 30 s. Lyophilized samples are collected using a 20x objective, power = 1.5 mW, and t_{int} = 50 s. Five measurements from different locations are averaged. Reported spectra are raw minus identically collected spectra from a control (matrix only). Detailed spectral analysis was reported previously[89] and can be found in Appendix B.

A.3 Results and discussion

A.3.1 Characterization of and uranyl uptake on PAN and AO-PAN mats

Previous studies indicated that amidoximation[21,77,108–116] 33-43 of PAN led to uranyl uptake that was dependent on pH, and additional gains in U extraction efficiency were achieved using high surface area to volume nanomaterials[117,118] and electrospun fibers.[21,119,120] Here, high surface area materials (surface area = 16.3 ± 0.6 m^2/g) used are integrated for Raman analysis in a step-wise fashion to maximize uranyl uptake and for reproducible and robust spectroscopic detection. As shown in Figure A-1A, electrospun PAN fibers form a mat structure with an average fiber diameter (d) of 100 ± 30 nm. PAN mats are hydrophilic[121] but did not readily coordinate to uranyl (*vide infra*). Amidoximation of the PAN fibers (Figure A-2A) does not significantly alter the average d (Figure A-1B) of 110 ± 20 nm. FTIR analysis confirms the

72

presence of amidoxime groups on PAN after functionalization (see Appendix B), and spectra are similar to previous literature reports.[106,107]

Fiber diameters remain constant upon incubation with uranyl (Figure A-1C, $d = 120 \pm 20$ nm). As shown in the photographs in Figure A-1, successful uranyl uptake is confirmed visually by a slight yellowing of the AO-PAN mats when 10 µM uranyl concentrations are used. Time-dependent uranyl uptake data from HEPES buffer (pH 6.8) are summarized in Figure A-2B. As incubation time increases, the amount of sorbed uranyl increases systematically during the first ~16 hours before reaching sorption equilibrium. As a result, an 18 hour incubation period is used for all subsequent uptake studies.

Additional sorption experiments with 1, 5, and 10 µM uranyl in the presence of 500 mg/L Ca^{2+} or 500 mg/L HCO_3^- as well as synthetic urine explores the influence of solution composition on uranyl uptake. Uptake in relatively idealized 10 mM HEPES is provided for comparison. As shown in Figure A- 2C, solution complexity produces no statistical difference in average uranyl uptake across the concentration range investigated for Ca^{2+} and HCO_3^-. Thus, uranyl binding by amidoxime groups on the AO-PAN surface appears relatively insensitive to environmental variables [e.g., components of hardness (Ca^{2+}) and alkalinity (HCO_3^-)] that often limit the capacity and selectivity of sorbents. Although uptake in synthetic urine is comparable to other matrices when uranyl concentration is below 5 µM, uptake is significantly impacted by the matrix at the highest U concentration investigated. We attribute these uptake differences to variations in uranyl speciation in solution and/or the formation of insoluble U[122], which reduces the effective concentration in solution.

A.3.2 Evaluation of uranyl uptake on AO-PAN mats using normal Raman spectroscopy

Now that successful uranyl uptake for various sample matrices has been confirmed, normal Raman detection is employed directly on lyophilized electrospun AO-PAN mats using Raman microscopy through evaluation of the symmetric uranyl stretch. Near-infrared excitation and a 50x objective are used to minimize mat damage by the laser and to reduce implications of mat roughness on measurements, respectively. Uranyl coordinated to AO-PAN mats is confirmed in Figure A-3A from the broad (full width at half maximum, Γ, 46 and 57 cm^{-1} for pH 4 and 6.8, respectively) spectral feature centered at 818 cm^{-1}. Several important details are noted. First, the vibrational feature band width is larger than that of a single solution-phase[13] uranyl species (~14-20 cm^{-1}). This suggests that the vibrational bands arise from uranyl coordinated to the AO-PAN mats (i.e., surface Raman spectra)[123] rather than from uranyl in solution. It is also possible that an increase in linewidth arises from multiple uranyl coordination geometries to the AO-PAN mat, but both hypotheses suggest that the UO_2^{2+} cation is bound to the mat surface. Next, the vibrational band intensity is ~1.6 times more intense when uranyl uptake occurs at pH 6.8 vs. 4. Finally, intensities and Γ increase but vibrational frequencies remain constant when the solution pH used during uptake increases from 4 to 6.8. Because pH impacts both uranyl speciation[92] and AO-PAN functional group protonation[113,124] both would influence the resulting vibrational features.

Previously, several computational and well-controlled experimental studies were conducted to decipher the structure of amidoxime and uranyl complexes[110,114,116] and formation constants.[109,112,113,124,125] We build on this excellent foundation for understanding these spectral features and uranyl binding mechanisms. First, we consider the pK_a values (assumed at infinite dilution) of acetamidoxime (5.78 and 13.50)[113,124] as a model compound to gain insights on the

thermodynamics of uranyl uptake on the functionalized mat surface. [113,124] These details are summarized in Figure A-1A and Table B-1. These pK_a data are based on experiments performed in solution (different from the AO-PAN surface chemistry, which is more complex and could slightly impact the thermodynamic parameters). In addition, the amidoximation process was previously shown to lead to carboxylate and cyclic amidoxime group formation, which further complicates uranyl speciation and uptake. Use of this simplified model, however, provides specific insights into U uptake mechanism and is corroborated by spectroscopy data as described in detail below.

At pH 4, the amidoxime groups are positively charged (protonated hydroxylamine or AOH_2^+), and uranyl uptake likely occurs via the formation of UO_2AO^+. In contrast, at pH 6.8 the amidoxime groups are mostly neutral (AOH) and/or deprotonated (AO^-) via residual hydroxide groups that remain on the hydrophilic polymer surface after functionalization. The resulting uranyl species would then be $UO_2AO(OH)$ and UO_2AO^+, respectively, as summarized in Figure A-6. Normal Raman spectra shown in Figure A-3A support these coordination mechanisms. As mentioned previously, the uranyl linewidths observed are consistent with surface-coordinated species. From the spectroscopic data and thermodynamic constants, we hypothesize that both $UO_2AO(OH)$ and UO_2AO^+ are isolated at pH 6.8 while only UO_2AO^+ forms at pH 4.

While the polymer mats are hydrophilic, hydration level influences swelling of the polymer mats,[126,127] which could induce slight vibrational frequency differences and irreproducibility in spectral intensities and band shapes. To improve measurement reproducibility, two approaches are used including evaluation of uranyl from AO-PAN mats in either hydrated or lyophilized states. First, AO-PAN mats are equilibrated in 1 and 10 mM uranyl then rinsed in water and buffer to remove weakly bound species. The mats are then immersed in

buffer and evaluated using normal Raman microscopy. Representative spectra for 1 and 10 mM uranyl collected from hydrated mats are shown in Figures A-3B-1 and A-3B-2, respectively. These spectra reveal that the vibrational band associated with uranyl collected on hydrated mats are centered at 820 cm^{-1}, and band areas increase slightly as uranyl concentration increases. This signal is easily detectable above the noise likely because of uranyl pre-concentration on the AO-PAN. As a comparison, normal Raman spectra of PAN and AO-PAN mats incubated in 1 mM uranyl is shown in Figures A-4A-1 and -2, respectively. No uranyl signal is observed from the unfunctionalized mats. This is consistent with negligible uptake as quantified using LSC (0.37±0.05 mg U per g mat). Uranyl uptake increases to 6.26 ± 1.33 mg U per g mat of AO-PAN and is confirmed from the small normal Raman signal observed in Figure A-4A-2.

Similar trends are observed for AO-PAN mats incubated in uranyl then lyophilized. These data are summarized in Figures A-3B-3 and A-3B-4 for 1 and 10 mM uranyl, respectively. First, similar increases in band area with increasing concentration are observed for the lyophilized vs. hydrated mats. Two notable differences, however, are observed. First, the normal Raman vibrational frequency for uranyl is slightly blue-shifted from that observed on hydrated mats. The small 2 cm^{-1} blue-shift of the vibrational frequency to 818 cm^{-1} is attributed to Stark effects.[128] Second, uranyl intensities are larger after lyophilization. Upon dehydration, the fibers deswell thus the amount of uranyl in the laser focal volume increases thereby increasing the signal magnitude. As a result, concentration-dependent uranyl signals are reproducible if the hydration state of the mats is maintained during these vibrational spectroscopy measurements.

A.3.3 Maximizing and understanding uranyl detection using SERS and AO-PAN mats

Previously, we reported a SERS based assay using solution-phase nanoparticles that resulted in the quantitative detection of uranyl down to 100 nM.[51] While reproducible measurements were achieved in buffer, uranyl detection was limited to solution conditions where nanoparticles retained their physical stability.[129] Using AO-PAN mats to extract uranyl from solution before SERS-active nanostructures are equilibrated with a sample, is a plausible approach for achieving reproducible and enhanced detection of these chemical species. This is demonstrated in Figure A-4A-3.

To attain this result, 6-MHA functionalized Au nanostars are added drop-wise to AO-PAN mats after uranyl uptake and rinsing. TEM and SEM images of the Au nanostars and AO-PAN mats after nanostar deposition are shown in Figures A-1E and -1D, respectively. The Au nanostars contain 3-7 spikes and average dimensions (diameter = 59.8 ± 14.0 nm, radius of curvature of tips = 3.8 ± 0.6 nm) consistent with previous reports.[51] When uranyl is present, the Au nanostars adhere to the fiber surfaces (Figure A-1E). This observation is consistent with nanostar coordination via terminal carboxylate groups on the nanostars to uranyl bound to the AO-PAN mats.

To evaluate the impact of Au nanostar functionalization on uranyl detectability, SERS microscopy is used. As shown in Figure A-4A-3, 10 μM uranyl is easily detected on hydrated AO-PAN mats. The vibrational frequency of uranyl is centered at 837 cm^{-1}, a value that is blue-shifted 17 cm^{-1} from the normal Raman mode. Because vibrational frequencies observed in SERS spectra typically red-shift relative to normal Raman frequencies (i.e., because bond lengths tend to increase upon interaction with nanomaterial surfaces),[96,99,130] we hypothesize that the carboxylate groups on the Au nanostars coordinate to uranyl upon disruption of uranyl

77

coordination to AO groups on the mats as shown in Figure A-6C. This is further confirmed in that SERS enhancement of uranyl is not observed when unfunctionalized nanostars are used.

Uranyl coordination, however, likely depends on the density of both singly-deprotonated amidoxime and 6-MHA groups on the Au nanostars. Because these values are not known quantitatively, we use SERS data to provide evidence in understanding how uranyl is coordinating to and/or interacting with the mats and nanostars for detection. To do this, SERS responses are collected from 10 µM uranyl incubated with 0.5 nM Au nanostars for 24 hrs at neutral pH. The solution is centrifuged for 5 minutes ($2500 \times g$), the supernatant removed, and the loose pellet deposited on glass, PAN mats, and AO-PAN mats. SERS spectra of these samples are summarized in Figure A-4B and vibrational mode frequency and lineshapes compared. These samples are selected because AO-PAN, PAN, and glass samples all contain carboxyl groups and amidoxime/nitrile, nitrile, and no other functional groups, respectively. Vibrational mode lineshapes are similar and vibrational frequencies are universally centered from 836-838 cm^{-1} (Γ = 30-35 cm^{-1}) in all spectra. This surprising result suggests that 6-MHA on the Au nanostars disrupt uranyl coordination to the amidoxime groups because of high densities of 6-MHA molecules locally vs. amidoxime as shown in Figure A-6.

A.3.4 Evaluating matrix effects in uranyl detection using SERS

To assess how matrix effects (a common limitation in SERS) impact SERS measurements, AO-PAN mats are incubated in 1-10 µM uranyl solutions adjusted to pH 6.8 in 10 mM HEPES with no other ion additions, 3.4 mM Ca(NO$_3$)$_2$, or 5 mM Na$_2$CO$_3$, or synthetic urine. This approach allows for the evaluation of how ideal solutions as well as those containing

common confounding ions and U coordinating ligands at their relevant concentrations in ground water (Ca^{2+} and CO_3^{2-}) and biological matrices (synthetic urine) impact SERS detection.

Of note, SERS intensities directly correlate to the amount of U sorbed for each matrix and are summarized in Figure A-5 and Table A-1. Uranyl signals using both lyophilized (Figure A-5A) and hydrated (Figure A-5B) AO-PAN mats are shown. In general, uranyl successfully coordinates to AO-PAN mats and carboxylated Au nanostars in all conditions. This result is unexpected, and several trends are noted. First, on samples analyzed with SERS, LSC measurements confirm that slight signal variations arise from differences in U uptake. Second, differences in SERS spectral features in the uranyl window (i.e., vibrational frequency ($\bar{\upsilon}$), Γ, and/or integrated area of the entire uranyl window) are reproducible if mat areas with uniform nanoparticle deposition are sampled thus suggesting robust detection and largely sample matrix-independent SERS detection. This provides further evidence of the uranyl coordination mechanism proposed in Figure A-6. Of note, sample dryness is impacted by the relative humidity (30-40% RH) during data collection because of mat swelling. In addition, each spectrum collected using lyophilized mats contains a vibrational mode centered at 817 cm^{-1}. This band is attributed to a CH_2 bending mode from the 6-MHA molecules.[131] This band was previously observed for well-ordered, solid-like alkane monolayers. Because this band occurs in the uranyl window, it limits spectral interpretation and must be considered when quantifying uranyl signals on lyophilized mats. As such, SERS measurements using lyophilized AO-PAN mats must be done carefully so that reproducible uranyl detection is realized.

An alternative route for reproducible detection is to use hydrated AO-PAN mat samples. As shown in Figure A-5B, samples collected from hydrated AO-PAN mats exhibit less intense uranyl vibrational modes; but these signals are more uniform, do not exhibit interference from

79

the 6-MHA CH_2 bending mode, and reveal vibrational frequencies that are red-shifted vs. spectra collected using lyophilized samples. For example, SERS spectra collected from samples incubated in HEPES exhibit a uranyl band centered at 835 cm^{-1} (Figure A-5B-1) when hydrated and 844 cm^{-1} (Figure A-5A-1) upon lyophilization. A red-shifted vibrational frequency upon hydration is attributed to Stark effects[128] as detailed in Appendix B and Table A-1.

We hypothesize that hydration increases the distance between nanostars on the polymer mats, which decreases the electric field strengths between the nanoparticles[132] in a sample matrix dependent manner thus inducing a red-shift in each vibrational frequency relative to the dehydrated samples. In addition to the vibrational frequency Stark effects, measurements collected on hydrated mats exhibit vibrational frequencies that differ by only ~2 cm^{-1} for all sample matrices. The vibrational frequency of uranyl in HEPES, Ca^{2+}, CO_3^{2-}, and synthetic urine are 835.3 ± 0.4, 832.8 ± 0.3, 835.0 ± 0.5, and 833.0 ± 0.6 cm^{-1}, respectively. Total integrated areas follow similar trends in the amount of U sorbed to the mats. That is, the largest signals are associated with samples incubated in HEPES followed by Ca^{2+} and CO_3^{2-}, then urine. While these trends can be partially attributed to different amounts of uranyl sorbed from the various sample matrices, the SERS signals likely also depend on electromagnetic coupling differences between Au nanostars on the AO-PAN mats.

Finally, evaluation of samples using both lyophilized and hydrated mats reveal useful information regarding uranyl coordination. For instance, all SERS spectra from lyophilized samples reveal intense (vs. normal Raman and hydrated mat SERS measurements) vibrational bands with frequencies ranging from 845-844 cm^{-1} for samples incubated in HEPES and Ca^{2+} and ~845-830 cm^{-1} for carbonate and urine samples. This suggests that the ligands coordinated to uranyl are similar (in HEPES and Ca^{2+}) and distinct from the second two (CO_3^{2-} and urine (PO_4^{3-}

80

)). Furthermore, these bands are consistent with uranyl coordinated to a carboxylate group from 6-MHA on Au nanostars and possibly to hydroxide as proposed in Figure A-6. The vibrational frequencies observed for the carbonate and urine samples suggest that either carbonate or phosphate[133] (urine) are coordinated to uranyl. In addition, the signals collected from urine are relatively broad and contain multiple vibrational frequencies each of which could arise from uranyl species coordinating to phosphate and/or those interacting with cations (i.e., Na^+) or small organic molecules that are present in urine. Exact confirmation of the proposed U speciation is beyond the scope of this work and will be explored in future studies. Furthermore, the integrated areas in the uranyl vibrational window obtained from the SERS spectra from both lyophilized and hydrated mat samples follow trends consistent with variations in uranyl uptake (Figures A-5C and A-5D) obtained from LSC of uranyl uptake on the AO-PAN mats thus demonstrating the powerfulness of this approach for detecting uranyl in complex matrices.

A.4 Conclusions

The successful sorption and detection of uranyl from four unique sample matrices was achieved using AO-PAN mats followed by addition of 6-MHA functionalized Au nanostars and SERS. AO-PAN mats exhibit high surface areas that facilitate large scale fabrication and functionalization that are ideal for uranyl isolation from near-neutral pH solutions. This was verified using structural as well as spectroscopic characterization of the mats at each stage of fabrication and uranyl detection. By comparing vibrational band frequencies, a potential mechanism of uranyl uptake using AO-PAN mats and functionalized Au nanostars was proposed. This includes initial isolation of uranyl via amidoxime coordination to the equatorial plane of uranyl followed by replacement of these coordinating groups by locally high densities of

carboxylate on the nanostars used for SERS detection. Given this likely coordination mechanism, simplified SERS spectra are observed from uranyl samples prepared in buffer, in the presence of confounding ions including Ca^{2+} and CO_3^{2-}, as well as synthetic urine. Vibrational frequencies collected using hydrated AO-PAN mats from all four of these matrices vary by only ~2 cm^{-1}. This result is impressive given large matrix effects are normally observed for uranyl detected from these solution conditions using traditional detection methodologies and with SERS in general. Thus, this study demonstrates that electrospun AO-PAN mats efficiently isolate uranyl from different matrices and that the subsequent addition of functionalized Au nanostars results in simplified Raman features for reproducible and robust uranyl detection. This work lays the foundation for a promising method for the rapid detection of trace uranyl from complex sample matrices that does not require radioactive tracers or sample pretreatment.
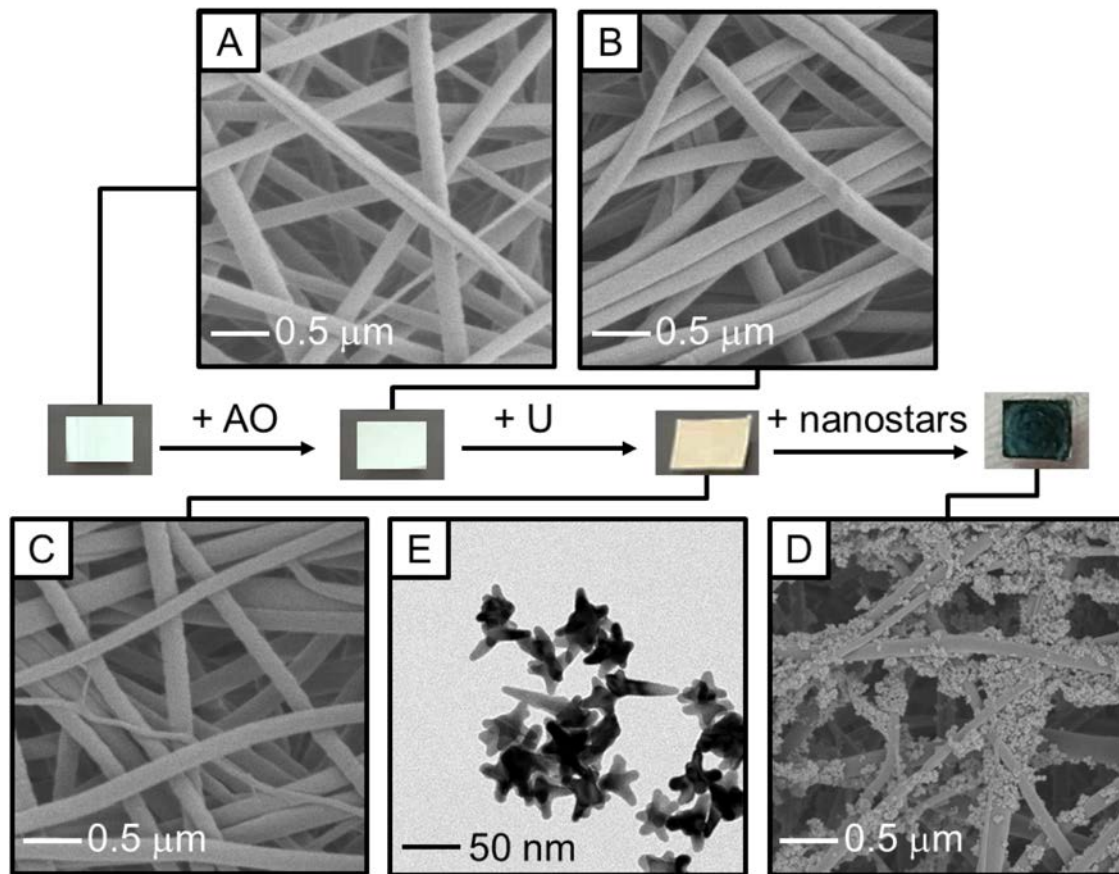
Figure A-1. Overview of the isolation and detection of uranyl using AO-PAN mats and Au nanostars. Representative photographs and SEM images of the PAN mats (A) as fabricated (d = 101 ± 28 nm), after (B) AO functionalization (d = 113 ± 22 nm), (C) uranyl uptake (d = 116 ± 24 nm), and (D) Au nanostar deposition are shown. In addition, (E) TEM images of the 6-MHA functionalized Au nanostars are shown (size = 59.8 ± 14.0 nm).
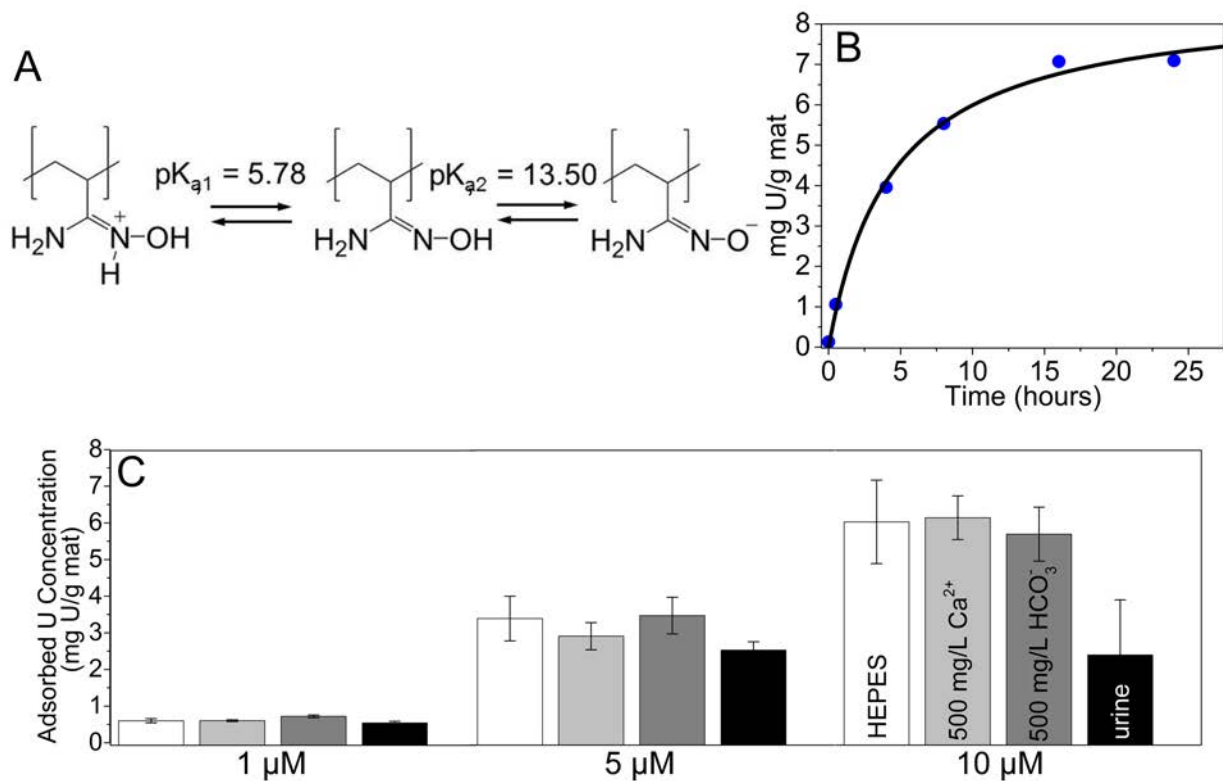
Figure A-2. Confirmation of U uptake. (A) Deprotonation of AO groups as a function of pH. (B) Evaluation of uranyl sorption as a function of incubation time using AO-PAN mats and LSC. A standard kinetic model is used to fit the data (y = 8.5*x/(4.43+x)). (C) Adsorbed U determined using LSC as a function of initial U concentration in 10 mM HEPES buffer as well as in HEPES buffer with 500 mg/L of Ca^{2+} or HCO_3^- or synthetic urine.
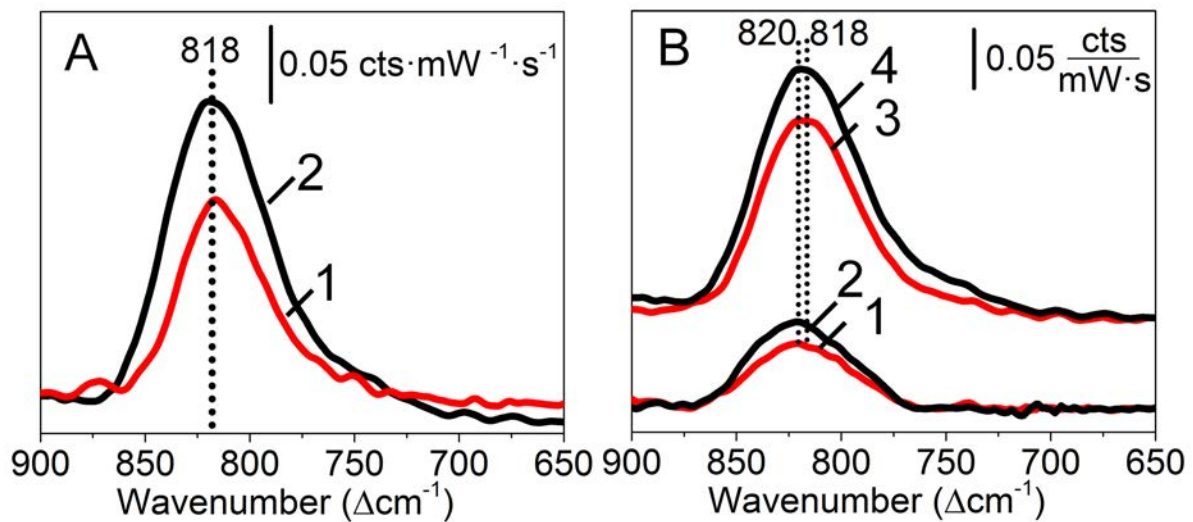
Figure A-3. Evaluation of uranyl detectability using Raman microscopy. (A) Normal Raman spectra of 10 mM uranyl uptake from pH (1) 4 and (2) 6.8 solutions onto lyophilized AO-PAN mats. (B) Normal Raman spectra of (1) 1 and (2) 10 mM uranyl collected using hydrated and (3) 1 and (4) 10 mM uranyl using lyophilized AO-PAN mats. Spectra are collected using the following parameters: λ_{ex} = 785 nm; t_{int}= 50 s and P = 55 mW, 5 averages; 50x objective; 10 mM HEPES was used (18 hour incubation).
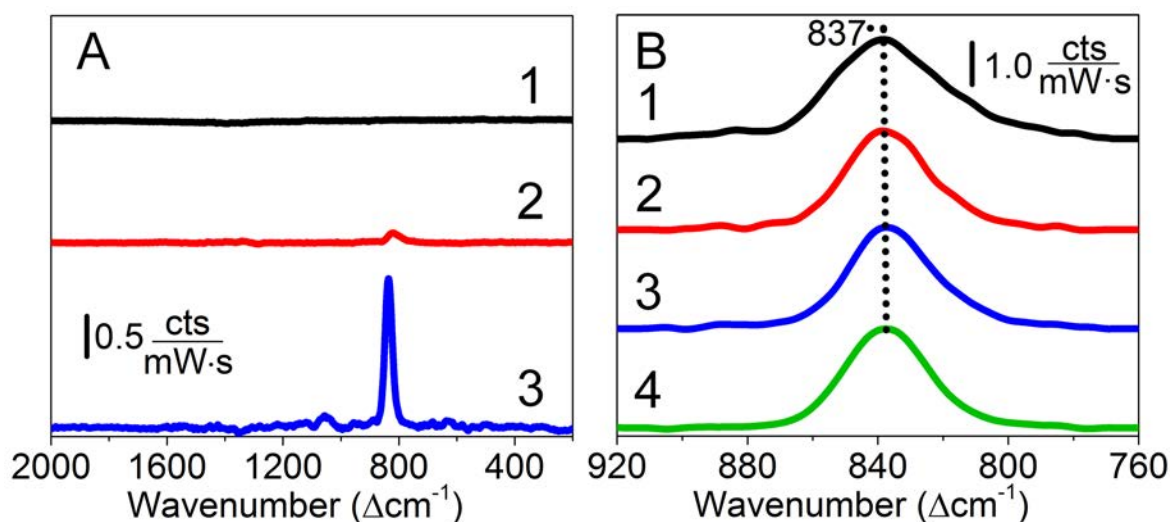
Figure A-4. (A) Normal Raman spectra of 1 mM uranyl after uptake on hydrated (1) PAN and (2) AO-PAN mats as well as (3) a representative SERS spectrum of 10 µM uranyl after uptake on hydrated AO-PAN mats. (B) SERS spectra of 10 µM uranyl incubated with Au nanostars then deposited onto a (1) glass slide ($\bar{\upsilon}$ =836.2 ± 1.5 cm^{-1} and Γ = 35.2 ± 1.5 cm^{-1}), (2) PAN mat ($\bar{\upsilon}$ =836.1 ± 0.7 cm^{-1} and Γ = 30.9 ± 1.0 cm$^{-1)}$, (3) AO-PAN mat ($\bar{\upsilon}$ =837.0 ± 0.5 cm^{-1} and Γ = 30.3 ± 0.6 cm^{-1}) and 10 µM uranyl (4) uptake on hydrated AO-PAN mats followed by addition of Au nanostars ($\bar{\upsilon}$ = 838.0 ± 0.5 cm^{-1} and Γ = 30.3 ± 1.0 cm^{-1}). Collection conditions for normal Raman spectra are the same as in Fig. A-3. SERS collection parameters: P = 25 mW, t_{int} = 30 sec, 10x objective (hydrated) or P = 1.5 mW, t_{int} = 50 sec, 50x objective (lyophilized).
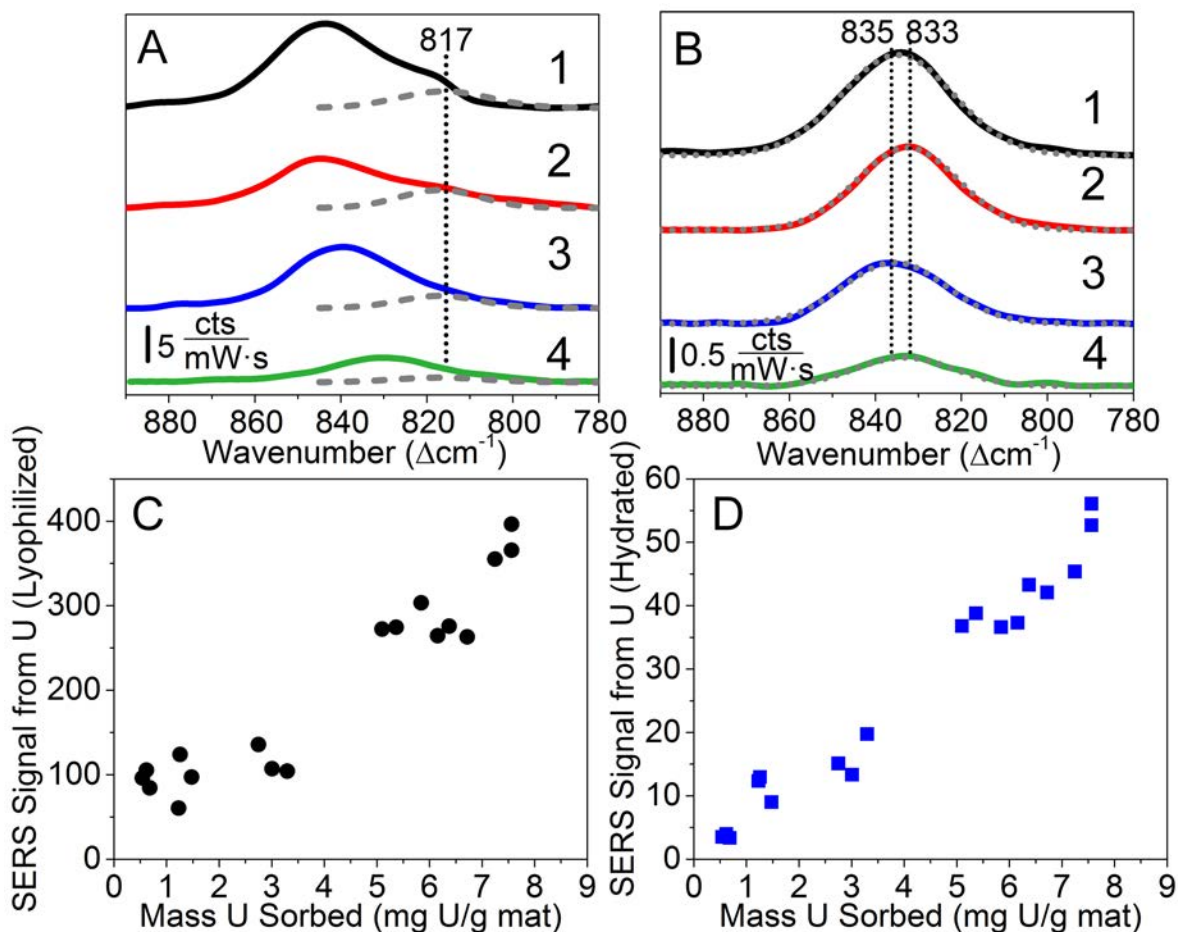
Figure A-5. SERS spectra of 10 µM uranyl (pH 6.8) in 1) 10 mM HEPES, 2) 3.4 mM Ca^{2+}, 3) 5 mM HCO_3^{2-}, and 4) synthetic urine using (A) lyophilized and (B) hydrated AO-PAN mats and 6-MHA functionalized Au nanostars. SERS on (C) lyophilized and (D) hydrated mats vs. mass U sorbed determined by LSC. The CH_2 bending mode from 6-MHA is observed in lyophilized spectra and is centered at 817 cm^{-1}. All other spectral features are from uranyl (Table A-1). Collection same as Figure A-4.
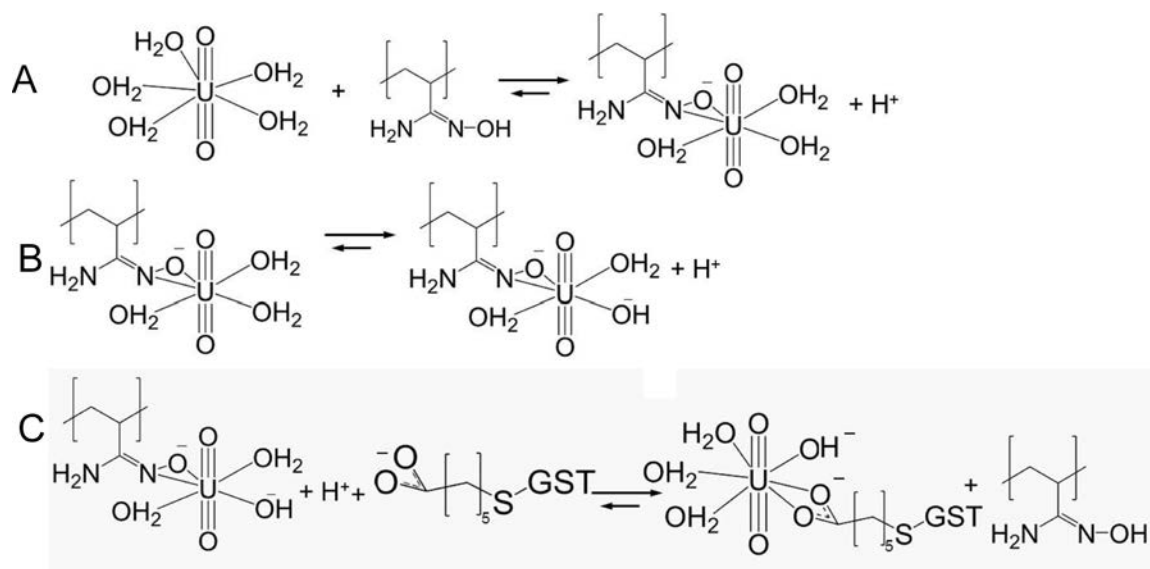
Figure A-6. Proposed pathway of uranyl uptake on AO-PAN mats from solution via hydroxylamine coordination to uranyl with (A) all aqua and (B) two aqua and one hydroxyl ligands and (C) coordination with carboxylic acid from 6-MHA functionalized Au nanostars.

Table A-1. Summary of U sorbed and correlated SERS measurements in various sample matrices

Matrix	LSC mass U sorbed (mg U/g mat)	SERS (lyophilized) $\bar{v}$ (cm^{-1})	Total Integrated Area (-MHA band)	SERS (hydrated) $\bar{v}$ (cm^{-1})	Total Integrated Area	Γ (cm^{-1})	Ratios of areas
HEPES	6.26 ± 1.33	844.4 ± 0.5	373 ± 22	835.3 ± 0.4	51.4 ± 5.4	31 ± 1	7.3
Ca^{2+}	5.99 ± 0.82	845.7 ± 0.4	267 ± 5	832.8 ± 0.3	38.7 ± 0.3	28 ± 1	6.9
HCO$_3^-$	5.73 ± 0.49	840.3 ± 1.1	284 ± 16	835.0 ± 0.5	39.6 ± 0.3	30 ± 2	7.2
Synthetic urine	2.48 ± 1.50	831.9 ± 1.1, 845.2 ± 3.0	79 ± 24	833.0 ± 0.6	11.4 ± 2.1	26 ± 1	6.9

B.1 Synthesis, functionalization, and FTIR characterization of electrospun PAN mats

For fabricating electrospun PAN mats, a polyvinylidene fluoride (PVDF) support layer is first prepared from a 12 wt% PVDF (average 180,000 g/mol) solution in dimethylacetamide and acetone (3:7 v/v). Next, a polyacrylonitrile (PAN) layer is prepared from a 7 wt% PAN (average 150,000 g/mol) solution in N,N-dimethylformamide (DMF). Both solutions are mixed for 2 h at 700 RPM and 60˚C (Eppendorf ThermoMixer C) prior to use. For conversion of nitrile groups in the PAN mat into amidoxime (AO) groups, a solution containing 15 g/L hydroxylamine hydrochloride and 0.375 M (15 g/L) sodium hydroxide is added to a 190×100 crystallizing dish. Next, 2 g/L (~0.065 m^2/L) composite PVDF-PAN mat is placed in this solution (PAN side down), which is then covered with aluminum foil to reduce solution evaporation and immersed into a Precision Scientific water bath (30 °C, 30 RPM) for 24 h. Mats are then rinsed extensively with DI water until the pH of the rinse water is less than 7, placed on parafilm (PAN side up), and dried for at least 12 h in air at room temperature. The functionalized PAN mats are stored at room temperature until use.

For electrospinning each layer, the appropriate sol gel is loaded into a 12 mL plastic syringe (HSW Norm-Ject) that is placed into a syringe drive (New Era Pump Systems, Inc.) and connected to a 2.0 mm ID polyethylene (PE) tube via a 1/16" PE female luer lock fitting. The tubing is connected to a metal nozzle adapter (NanoNC Co., Ltd) using a second 1/16" PE female luer lock fitting and a ½" 25G needle attached to other end of the nozzle. The tip of the needle is placed 10 cm from the surface of a 9 5/16" circumference metal drum collector (SPG Co., Ltd; Korea), which is grounded and covered in aluminum foil. The PVDF solution is

---

[2] SI submitted to Analytical Chemistry

electrospun first using a pumping speed of 0.4 mL/hour, a +21 kV tip voltage (Acopian), and a grounded collector rotating at 500 RPM (Dingtuo Technology). The PAN solution is electrospun using identical parameters except that 0.3 mL/h pumping speeds and +15 kV tip voltages are used. The PAN layer is deposited directly onto the underlying PVDF support layer, after which the bilayer polymeric composite mat is removed from the foil using tweezers for further processing.

FTIR spectroscopy (Gold Infinity) is used to confirm mat functionalization. Samples are placed on KBr salt plates, loaded into the chamber, and purged with dry air. Single beam scans are performed in transmission mode. Data shown represent 250 averaged spectra and were collected using a spectral resolution of 4 cm^{-1}. From FTIR spectroscopy (Figure B-1), PAN mats before and after incubation in hydroxylamine exhibited up to four spectral features. First, the C≡N stretch at 2240 cm^{-1} was observed in both spectra, but the relative absorbance with respect to the 1450 cm^{-1} (CH$_2$ scissoring, internal standard) decreased by ~10% with conversion of nitrile groups into C=N during amidoxiation. This is consistent with previous studies in which up to ~30% of nitrile was converted into amidoxime.[21] Second, a C=N stretch[134] at 1650 cm^{-1} was observed after amidoxime functionalization. Finally, vibrational modes associated with N-H scissoring[134] at 1600 cm^{-1} and O-H stretching[43] from 3000-3700 cm^{-1} were observed upon amidoximation. These functional groups directly coordinate to uranyl for sorption from the various sample matrices. These results are consistent with prior analysis by Horzum and co-workers.[106,107]

<u>B.2 Additional details for U uptake on the mats</u>

Uranyl sorption experiments were performed in 50 mL conical tubes by adding known amounts of a 1000 mg/L depleted uranium (SPEX CertiPrep) stock solution. For analysis by LSC, 85.0 μL of ^{232}U radiotracer (3.5 Bq, NIST traceable standard, Eckert & Ziegler) was added to the depleted uranium stock solution. *CAUTION: ^{238}U and ^{232}U are both radioactive isotopes and are only handled by trained personnel in a properly licensed facility*. It is important to note that the radiotracer was only used to validate the U uptake and the spectroscopic analysis was performed on mats that only contained depleted uranium. The stock solution is diluted to a final volume of 20 mL in 10 mM HEPES (pH 6.8), 3.4 mM $CaCl_2$, 5 mM $NaCO_3$, or 20 mL Surine™ Negative Urine Control (Cerilliant). Uranyl concentrations ranging from 10 μM-10 mM are used and the final pH of 6.8 using 5 N NaOH or 5 N HCl.

Next, 5 mg of the amidoximated composite mat (dry weight) is added to the prepared solutions and incubated in the uranyl solution on a tube rotator for 18 hours unless noted. The mats are then rinsed with water and stored at room temperature in scintillation vials until analysis. Mats are prepared in triplicate. In addition, one mat incubated in the matrix without uranyl is prepared for control measurement purposes.

<u>B.3 Initial characterization of U uptake using LSC and Raman microscopy</u>

Uranyl uptake is confirmed using liquid scintillation counting (LSC). Mats (5 mg dry weight) and 3 mL of 0.1 M HCl are placed in 20 mL scintillation vials to desorb uranyl. After 2 hours, 17 mL of a liquid scintillation cocktail is added to the vial, which is mixed well then allowed to equilibrate until bubbles are no longer visible. A Liquid Scintillation Counter

(Packard) is used. Signals are measured from 75-2000 keV for 40 minutes. All measurements represent averages and standard deviations collected from a minimum of three mats. Normal Raman microscopy confirmed uranyl uptake. A semi-homebuilt Raman microscope (Olympus BX51) modified with a CCD detector (ExamineR785, DeltaNu) is used. Prior to analysis, mats are dried for 1 hour at room temperature in air. Lyophilized samples are then placed in a freeze dryer (Thermo-Fisher) for 24 hours and stored in a vacuum chamber until analysis. Hydrated samples are placed on a microscope slide. Next, 50 µL water is added to the mats and covered carefully with a cover slip to ensure no air bubbles are trapped. Measurements on at least three samples are taken using an excitation wavelength (λ_{ex}) of 785 nm, laser power (P) of 53 mW, an integration time (t_{int}) of 50 seconds, 5 averages, and a 50x objective. The detector is calibrated using a polystyrene standard, and raw spectra are collected. Reported spectra are generated by subtracting identically collected blank measurements from the uranyl containing samples.

B.4 Synthesis, functionalization, and characterization of gold nanostars

Briefly, gold nanostars are synthesized by adding 20 mM HAuCl$_4$ (200 µL) into 50 mM EPPS (pH 7.4, 20 mL), mixing, and equilibrating the solution for 2 hours. Next, an additional 50 µL of the 20 mM HAuCl$_4$ solution is added and allowed to equilibrate for 1 hour at 35˚C. Gold nanostar functionalization proceeds by adding a 10 mM 6-MHA solution to a 1 nM gold nanostar solution using a syringe pump at a rate of 10 µL·min^{-1} until the final 6-MHA concentration is 0.91 mM. The gold nanostars (ε_{724} nm = 2.31×10^9 cm^{-1}·M^{-1})[135] are stored in 5 mM EPPS at a concentration of 0.3 nM. The localized surface plasmon resonance wavelength of the gold

nanostars shifts from 723.5 to 735.8 nm upon functionalization. Thus, these materials exhibit plasmonic properties that are appropriate for near-infrared SERS measurements.

B.5 Detailed protocol for and understanding of Raman and SERS data

Uranyl spectral features are confirmed by second derivative analysis of the uranyl window from 900-780 cm^{-1}.[89] Briefly, the spectra were smoothed using an 8-12 point Savitzky-Golay and a second order polynomial function. The second derivative is calculated, and all wavenumbers above a 20% threshold are considered significant and possible uranyl species. Next, overlapping vibrational bands in this spectral window are found by defining a baseline from 900-780 cm^{-1}. Gaussian functions are fit with full width at half maxima (Γ) ranging from 25-30 cm^{-1} and centers at the previously determined vibrational frequencies ($\pm$ 1 cm^{-1}) found in the second derivative spectra (fitting tolerance = 10^{-6}). Band intensities that are less than three times the noise (calculated from 1850-1950 cm^{-1}) are considered insignificant and not further analyzed. Peak areas of the uranyl window are reported using integration.

A red-shifted vibrational frequency upon hydration is attributed to vibrational Stark effects, in which local electric field effects on vibrational frequencies are considered.[128] These local electric fields can be approximated from calculated SERS enhancement factors (EF):

$$EF = (|E_{exc}|^2/|E_0|^2) \cdot (|E_{em}|^2/|E_0|^2) \approx E^4 \qquad\qquad \text{Eq B-1}$$

where E_{exc} is the excitation field, E_{em}, is the emitted field, and E_0 is the incident field. Both the excitation and emitted fields are normalized relative to the incident field. Furthermore, the

94

emitted field is approximately equivalent to the excitation field, thus the EF is proportional to the electric field to the 4th power.

Effects of electric field differences can be assessed from the collected SERS data. To do this, the integrated areas from lyophilized sample matrices (minus the 6-MHA band contribution) and from hydrated samples are calculated by integrating the total area in the uranyl window (see Table A-1). A ratio of these areas can then be used to roughly compare the enhancement factors and electric field enhancement differences between lyophilized and hydrated SERS-active mats as a function of sample matrix. For instance, the EF from the lyophilized sample compared to the hydrated sample collected from HEPES is ~7x larger (i.e., integrated areas of 373/51.4 in the lyophilized vs. hydrated samples). As a result, the electric field strengths between the two samples vary by approximately the same amount. Ratios of these signals vary from ~6 to 10x for uranyl detected from the various sample matrices. As such, the observed SERS signal magnitudes likely depend on this enhancement. We hypothesize that the presence of water in the hydrated samples increases the distance between nanostars on the polymer mats, which decreases the electric field between the nanoparticles[132] in a sample matrix dependent manner thus inducing a red-shift in each of the vibrational frequencies relative to the dehydrated samples.

B.6 Summary of thermodynamic constants for uranyl speciation predictions

The relative abundance of each uranyl species can be estimated using the equilibrium constants found for each coordinating ground (Table B-1) and can be represented as a ratio of each uranyl species to uncoordinated uranyl (i.e., $[UO_2AO^+]/[UO_2^{2+}]$ or $[UO_2AO(OH)]/[UO_2^{2+}]$).[95] Because uranyl coordination depends on the local density and chemical composition, we can qualitatively predict relative ratios of uranyl species to

uncoordinated uranyl for the various coordination sites. As this ratio increases, a particular

species will more readily form. This applies both before and after gold nanostar addition. As

such, when uranyl coordinates to 6-MHA bound to gold nanostars, an effective species is

expected to form (UO_2S*^{2+} where S represents adsorbed 6-MHA on gold nanostars (4.58×10^{14}

molecules/cm^2)).[129] The ratio of complex uranyl to free uranyl is $[UO_2S*^{2+}]/[UO_2^{2+}]$. As such,

the equilibrium constant ($\log(K_9)$) of uranyl and 6-MHA on functionalized gold nanostar surfaces

can be used. Previously, this was quantified using Langmuir adsorption isotherm analysis and

determined to be 5.85 (from $K_{eq,MHA} = 0.71 \pm 0.18 \ \mu M^{-1}$).[51] These values are included in Table

B-1, and ($[UO_2S^{2+}]/[UO_2^{2+}]$) is equal to $K_9[S]$ when functionalized gold nanostars are incubated

with uranyl. When considering these thermodynamic values and experimental results, local not

bulk densities of uranyl, 6-MHA, and amidoxime are hypothesized to lead to the observed

results.
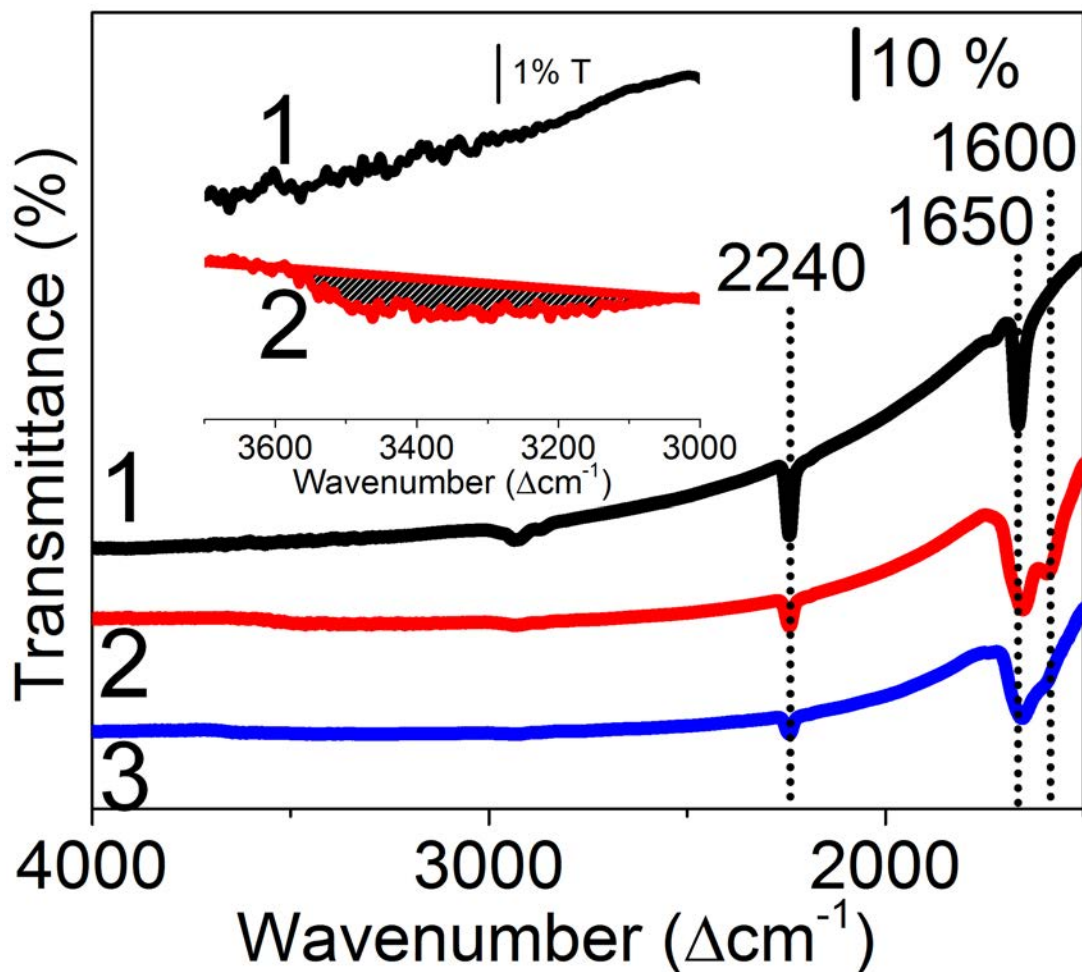
Figure B-1. Characterization and confirmation of PAN mat functionalization and 10 mM uranyl uptake (pH 6.8, in 10 mM HEPES for 18 hrs). (A) FTIR spectra of (1) PAN and AO-PAN mats (2) before and (3) after incubation in uranyl. Mat functionalization is confirmed via vibrational bands centered at 1600 (NH_2 scissoring), 1650 (C=N stretching), 2240 (C≡N stretching), and 3000-3700 cm^{-1} (magnified spectra shown in the inset, OH stretching).

Table B-1. Summary of chemical reactions and formation/equilibrium constants (K)

Reaction	Log K	Eq.	Reference
$AOH_2^+ \rightleftharpoons AOH + H^+$	-5.78	(1)	113
$AOH \rightleftharpoons AO^- + H^+$	-13.21	(2)	113, 124
$UO_2^{2+} + AO^- \rightleftharpoons UO_2AO^+$	13.6	(3)	113
$UO_2^{2+} + AO^- + OH^- \rightleftharpoons UO_2AO(OH)$	6.8	(4)	113
$UO_2^{2+} + AOH_2^+ \rightleftharpoons UO_2AO^+ + 2H^+$	-5.39	(5)	Derived from (1), (2), and (3)
$UO_2^{2+} + AOH \rightleftharpoons UO_2AO^+ + H^+$	0.41	(6)	Derived from (2) and (3)
$UO_2^{2+} + AOH + OH^- \rightleftharpoons UO_2AO^+ + H_2O$	14.41	(7)	Derived from (6) and K_w
$UO_2^{2+} + OH^- + AOH \rightleftharpoons UO_2AO(OH) + H^+$	7.21	(8)	Derived from (2), (3), and (4)
$UO_2^{2+} + 2OH^- + AOH \rightleftharpoons UO_2AO(OH) + H_2O$	20.21	(9)	
$UO_2^{2+} + S^* \rightleftharpoons UO_2S^{*2+}$	5.85	(10)	51

*S: the adsorbed 6-mercaptohexanoic acid on the nanostar surfaces.

Literature Cited

1. Jones, V. C. *Manhattan, the Army and the atomic bomb. United States Army in World War II Special studies* (Center of Military History For sale by the Supt. of Docs., U.S. G.P.O., 1985).
2. Ram, N. M., Moore, C. & Mctiernan, L. Cleanup Options for Navajo Abandoned Uranium Mines. *Remediation* **26,** 131–148 (2016).
3. McLemore, V. Uranium Resources in New Mexico. *Proceedings for SME Annual Meeting 2007 and CMA 109th National Western Conference 2007: The Power of Mining: Energy's Influence* 1–13 (2007). Available at: https://geoinfo.nmt.edu/resources/uranium/nmresources.html. (Accessed: 10th March 2018)
4. Blake, J. M. *et al.* Elevated Concentrations of U and Co-occurring Metals in Abandoned Mine Wastes in a Northeastern Arizona Native American Community. *Environ. Sci. Technol.* **49,** 8506–8514 (2015).
5. US Environmental Protection Agency, O. of W. Radionuclides Rule: A Quick Reference Guide. **65,** EPA 816-F-01-003 (2001).
6. Kamp, S. D. & Morrison, S. J. Use of chemical and isotopic signatures to distinguish between uranium mill-related and naturally occurring groundwater constituents. *Groundw. Monit. Remediat.* **34,** 68–78 (2014).
7. Orloff, K. G. *et al.* Human exposure to uranium in groundwater. *Environ. Res.* **94,** 319–326 (2004).
8. Ting, B. G. *et al.* Uranium and thorium in urine of United States residents: Reference range concentrations. *Environ. Res.* **81,** 45–51 (1999).
9. World Health Organization. *Uranium in drinking-water: background document for development of WHO guidelines for drinking-water quality.* (2004).
10. Centers for Disease Control and Prevention. Biomonitoring Summaries - Lead. (2016). Available at: https://www.cdc.gov/biomonitoring/Lead_BiomonitoringSummary.html. (Accessed: 11th March 2018)
11. Wei, B. L. *et al.* Biokinetic modeling of uranium in man after injection and ingestion. *Radiat. Environ. Biophys.* **44,** 29–40 (2005).
12. Vicente-Vicente, L. *et al.* Nephrotoxicity of uranium: Pathophysiological, diagnostic and therapeutic perspectives. *Toxicol. Sci.* **118,** 324–347 (2010).
13. Lourenço, J. *et al.* Evaluation of the sensitivity of genotoxicity and cytotoxicity endpoints in earthworms exposed in situ to uranium mining wastes. *Ecotoxicol. Environ. Saf.* **75,** 46–54 (2012).
14. Audi, G. & Wapstra, A. H. Table of Isotopic Masses and Natural Abundances. *Nucl. Phys. A* **565,** 1–65 (1993).
15. Lehto, J. & Hou, X. *Chemistry and analysis of radionuclides laboratory techniques and methodology.* (Wiley-VCH Verlag GmbH & Co. KGaA, 2010). doi:10.1002/9783527632770
16. Casey, J. A. *et al.* Predictors of indoor radon concentrations in Pennsylvania, 1989 -- 2013. *Environ. Health Perspect.* (2015). doi:10.1289/ehp.1409014
17. Elío, J., Crowley, Q., Scanlon, R., Hodgson, J. & Zgaga, L. Estimation of residential radon exposure and definition of Radon Priority Areas based on expected lung cancer incidence. *Environ. Int.* **114,** 69–76 (2018).

18. Dalrymple, G. B. The age of the Earth in the twentieth century: a problem (mostly) solved. *Geol. Soc. London, Spec. Publ.* **190,** 205–221 (2001).

19. Cahill, C. L., de Lill, D. T. & Frisch, M. Homo- and heterometallic coordination polymers from the f elements. *CrystEngComm* **9,** 15–26 (2007).

20. Zanonato, P. L. *et al.* Hydrolysis of Uranium(VI) at Variable Temperatures (10-85 °C). *J. Am. Chem. Soc.* **126,** 5515–5522 (2004).

21. Horzum, N., Shahwan, T., Parlak, O. & Demir, M. M. Synthesis of amidoximated polyacrylonitrile fibers and its application for sorption of aqueous uranyl ions under continuous flow. *Chem. Eng. J.* **213,** 41–49 (2012).

22. Loiseau, T., Mihalcea, I., Henry, N. & Volkringer, C. The crystal chemistry of uranium carboxylates. *Coord. Chem. Rev.* **266–267,** 69–109 (2014).

23. Pasilis, S. P. & Pemberton, J. E. Speciation and Coordination Chemistry of Uranyl(VI)-Citrate Complexes in Aqueous Solution. *Inorg. Chem.* **42,** 6793–6800 (2003).

24. Usgs. NATURAL PROCESSES OF GROUND-WATER AND SURFACE-WATER INTERACTION The. *Usgs* 1–13 (2016). Available at: http://pubs.usgs.gov/circ/circ1139/htdocs/natural_processes_of_ground.htm. (Accessed: 14th March 2018)

25. Green, D. W. & Perry, R. H. *Perry's Chemical Engineer's Handbook. Book* (Sixth edition / prepared by a staff of specialists under the editorial direction of late editor Robert H. Perry ; editor, Don W. Green ; assistant editor, James O. Maloney. New York : McGraw-Hill, [1984] ©1984, 2008).

26. Zhang, R., Hu, S., Zhang, X. & Yu, W. Dissolution kinetics of dolomite in water at elevated temperatures. *Aquat. Geochemistry* **13,** 309–338 (2007).

27. Blake, J. M. *et al.* Uranium mobility and accumulation along the Rio Paguate, Jackpile Mine in Laguna Pueblo, NM. *Environ. Sci. Process. Impacts* **19,** 605–621 (2017).

28. IAEA. Live Chart of Nuclides - Nuclear Structure and Decay Data. (2014). Available at: https://www-nds.iaea.org/relnsd/vcharthtml/VChartHTML.html. (Accessed: 19th March 2018)

29. Environmental, S., Group, I. & Street, R. Evaluation of Uranium Measurements in Water by Various Methods – 13571 Brian J . Tucker , Ph . D .* and Stephen M . Workman ** ** ALS Laboratory Group , Environmental Division , 225 Commerce Drive , Fort Collins , CO 80524 ; Steve.Workman@ALSGlobal.com. 1–11 (2013).

30. Zhang, C. C. *Fundamentals of Environmental Sampling and Analysis. Fundamentals of Environmental Sampling and Analysis* (Wiley-Interscience, 2007). doi:10.1002/0470120681

31. States, U. Point-of-Use or Point-of- Entry Treatment Options for Small Drinking Water Systems. *US Environ. Prot. Agency* EPA 815-R-06-010 (2006). doi:EPA 815-R-06-010

32. Sorg, T. J. Methods for Removing Uranium From Drinking Water. *Source J. (American Water Work. Assoc. Radionuclides* **80,** 105–111 (1988).

33. Ahmed, F. E., Lalia, B. S. & Hashaikeh, R. A review on electrospinning for membrane fabrication: Challenges and applications. *Desalination* **356,** 15–30 (2015).

34. Peter, K. T. *et al.* Synthesis, Optimization, and Performance Demonstration of Electrospun Carbon Nanofiber-Carbon Nanotube Composite Sorbents for Point-of-Use Water Treatment. *ACS Appl. Mater. Interfaces* **8,** 11431–11440 (2016).

35. Mohammadi, M. *et al.* Micro and nanotechnologies for bone regeneration: Recent advances and emerging designs. *J. Control. Release* **274,** 35–55 (2018).

36. Zhao, P. *et al.* Fabrication of scaffolds in tissue engineering: A review. *Front. Mech. Eng.* **13,** 107–119 (2018).
37. Choi, S. J. *et al.* Electrospun Nanostructures for High Performance Chemiresistive and Optical Sensors. *Macromol. Mater. Eng.* **302,** 1600569 (2017).
38. Terra, I. A. A., Mercante, L. A., Andre, R. S. & Correa, D. S. Fluorescent and colorimetric electrospun nanofibers for heavy-metal sensing. *Biosensors* **7,** 61 (2017).
39. Mercante, L. A., Scagion, V. P., Migliorini, F. L., Mattoso, L. H. C. & Correa, D. S. Electrospinning-based (bio)sensors for food and agricultural applications: A review. *TrAC - Trends Anal. Chem.* **91,** 91–103 (2017).
40. Peter, K. T., Johns, A. J., Myung, N. V. & Cwiertny, D. M. Functionalized polymer-iron oxide hybrid nanofibers: Electrospun filtration devices for metal oxyanion removal. *Water Res.* **117,** 207–217 (2017).
41. Chaúque, E. F. C., Dlamini, L. N., Adelodun, A. A., Greyling, C. J. & Catherine Ngila, J. Modification of electrospun polyacrylonitrile nanofibers with EDTA for the removal of Cd and Cr ions from water effluents. *Appl. Surf. Sci.* **369,** 19–28 (2016).
42. Bode-Aluko, C. A., Pereao, O., Ndayambaje, G. & Petrik, L. Adsorption of Toxic Metals on Modified Polyacrylonitrile Nanofibres: A Review. *Water. Air. Soil Pollut.* **228,** (2017).
43. Huang, F. *et al.* Preparation of amidoxime polyacrylonitrile chelating nanofibers and their application for adsorption of metal ions. *Materials (Basel).* **6,** 969–980 (2013).
44. Daoud, J. A., Zeid, M. M. & Aly, H. F. Tetravalent uranium extraction by HDEHP in kerosene from phosphate medium. *Solvent Extr. Ion Exch.* **15,** 203–217 (1997).
45. Paul, S., Pandey, A. K., Shah, R. V., Bhushan, K. S. & Aggarwal, S. K. Polymer based sorbent materials for thermal ionization mass spectrometric determination of uranium(VI) and plutonium(IV) ions. *J. Anal. At. Spectrom.* **31,** 985–993 (2016).
46. Smith, S. W. The Role of Chelation in the Treatment of Other Metal Poisonings. *J. Med. Toxicol.* **9,** 355–369 (2013).
47. Riegel, M. Sorption of Natural Uranium on Weakly Basic Anion Exchangers. *Solvent Extr. Ion Exch.* **35,** 363–375 (2017).
48. Blackie, E. J., Le Ru, E. C. & Etchegoin, P. G. Single-molecule surface-enhanced raman spectroscopy of nonresonant molecules. *J. Am. Chem. Soc.* **131,** 14466–14472 (2009).
49. Xu, X. *et al.* Near-field enhanced plasmonic-magnetic bifunctional nanotubes for single cell bioanalysis. *Adv. Funct. Mater.* **23,** 4332–4338 (2013).
50. Sharma, B., Frontiera, R. R., Henry, A. I., Ringe, E. & Van Duyne, R. P. SERS: Materials, applications, and the future. *Mater. Today* **15,** 16–25 (2012).
51. Lu, G., Forbes, T. Z. & Haes, A. J. SERS detection of uranyl using functionalized gold nanostars promoted by nanoparticle shape and size. *Analyst* **141,** 5137–5143 (2016).
52. Kapnisti, M. *et al.* Enhanced sorption capacities for lead and uranium using titanium phosphates; sorption, kinetics, equilibrium studies and mechanism implication. *Chem. Eng. J.* **342,** 184–195 (2018).
53. Calì, E. *et al.* Functionalised magnetic nanoparticles for uranium adsorption with ultra-high capacity and selectivity. *J. Mater. Chem. A* **6,** 3063–3073 (2018).
54. Popov, L. Determination of uranium isotopes in environmental samples by anion exchange in sulfuric and hydrochloric acid media. *Appl. Radiat. Isot.* **115,** 274–279 (2016).

55. Zagorodnyaya, A. N. *et al.* Sorption of rhenium and uranium by strong base anion exchange resin from solutions with different anion compositions. *Hydrometallurgy* **131–132,** 127–132 (2013).

56. Kizildag, N., Ucar, N., Onen, A. & Karacan, I. Polyacrylonitrile/polyaniline composite nanofiber webs with electrostatic discharge properties. *J. Compos. Mater.* **50,** 3981–3994 (2016).

57. Li, W. *et al.* Solvent-solubility-parameter-dependent homogeneity and sol–gel transitions of concentrated polyacrylonitrile solutions. *J. Appl. Polym. Sci.* **134,** (2017).

58. Liao, Y., Loh, C. H., Tian, M., Wang, R. & Fane, A. G. Progress in electrospun polymeric nanofibrous membranes for water treatment: Fabrication, modification and applications. *Progress in Polymer Science* **77,** 69–94 (2018).

59. Ehrmann, A., Grothe, T., Wehlage, D., Böhm, T. & Remche, A. Needleless Electrospinning of PAN Nanofiber Mats. in *Proceedings of the Second International Conference on Mechanics, Materials and Structural Engineering (ICMMSE 2017)* **60,** 290–295 (2017).

60. Lin, T., Wang, H., Wang, H. & Wang, X. The charge effect of cationic surfactants on the elimination of fibre beads in the electrospinning of polystyrene. *Nanotechnology* **15,** 1375–1381 (2004).

61. Peter, K. T. *et al.* Synthesis, Optimization, and Performance Demonstration of Electrospun Carbon Nanofiber-Carbon Nanotube Composite Sorbents for Point-of-Use Water Treatment. *ACS Appl. Mater. Interfaces* **8,** 11431–11440 (2016).

62. Peter, K. T., Myung, N. V. & Cwiertny, D. M. Surfactant-assisted fabrication of porous polymeric nanofibers with surface-enriched iron oxide nanoparticles: composite filtration materials for removal of metal cations. *Environ. Sci. Nano* (2018). doi:10.1039/C7EN00720E

63. Stuart, B. H. *Infrared Spectroscopy: Fundamentals and Applications*. *Infrared Spectroscopy: Fundamentals and Applications* **8,** (2005).

64. Malik, H. *et al.* Removal of lead from aqueous solution using polyacrylonitrile/magnetite nanofibers. *Environ. Sci. Pollut. Res.* **25,** 3557–3564 (2018).

65. Pan, W. E. I., He, X. & Chen, Y. A. N. Preparation and characterization of polyacrylonitrile / antimony doped tin oxide composite nanofibers by electrospinning method. *Optoelectron. Adv. Mater. Commun.* **4,** 390–394 (2010).

66. St John, A. M. *et al.* Micrometer-scale 2D mapping of the composition and homogeneity of polymer inclusion membranes. *Aust. J. Chem.* **64,** 930–938 (2011).

67. Luschtinetz, R., Seifert, G., Jaehne, E. & Adler, H. J. P. Infrared spectra of alkylphosphonic acid bound to aluminium surfaces. in *Macromolecular Symposia* **254,** 248–253 (Wiley-Blackwell, 2007).

68. Hu, L. *et al.* Preparation of amidoximated coaxial electrospun nanofibers for uranyl uptake and their electrochemical properties. *Sep. Purif. Technol.* **171,** 44–51 (2016).

69. Shao, D. *et al.* Phosphate-Functionalized Polyethylene with High Adsorption of Uranium(VI). *ACS Omega* **2,** 3267–3275 (2017).

70. Gorman-Lewis, D., Burns, P. C. & Fein, J. B. Review of uranyl mineral solubility measurements. *J. Chem. Thermodyn.* **40,** 335–352 (2008).

71. Fujiwara, K. *et al.* Solubility product of hexavalent uranium hydrous oxide. *J. Nucl. Sci. Technol.* **42,** 289–294 (2005).

72.   Cheng, K. *CRC Handbook of Organic Analytical Reagents*. (Routledge, 182AD). doi:10.1201/9781315140568

73.   Kiwan, A. M. and A. R. S. The Solvent Extraction of Uranium(Iv)--Iii Extraction of Uranium(Iv) by Di-(2-Ethylhexyl) Phosphoric Acid from Sulphuric Acid Solutions. **36,** 2591–2593 (1974).

74.   Chivot, J., Mendoza, L., Mansour, C., Pauporté, T. & Cassir, M. New insight in the behaviour of Co-H2O system at 25-150 °C, based on revised Pourbaix diagrams. *Corros. Sci.* **50,** 62–69 (2008).

75.   Gunathilake, C., Górka, J., Dai, S. & Jaroniec, M. Amidoxime-modified mesoporous silica for uranium adsorption under seawater conditions. *J. Mater. Chem. A* **3,** 11650–11659 (2015).

76.   Pekel, N., Sahiner, N. & Guven, O. Thermodynamics of Adsorption of Uranyl Ions onto Amidoximated Poly(acrylonitrile)/Poly(n-vinyl 2-pyrrolidone) Interpenetrating Polymer Networks. *J. Polym. Sci. Part B Polym. Phys.* **42,** 986–993 (2004).

77.   Hirotsu, T., Katoh, S., Sugasaka, K., Seno, M. & Itagaki, T. Adsorption equilibrium of uranium from aqueous [UO2(CO3)3]4- solutions on a polymer bearing amidoxime groups. *J. Chem. Soc. Dalt. Trans.* **0,** 1983–1986 (1986).

78.   Agency, E. P. Addressing Uranium Contamination on the Navajo Nation. 1–2 (2015). Available at: http://www3.epa.gov/region9/superfund/navajo-nation/.

79.   Bernhard, G., Geipel, G., Brendler, V. & Nitsche, H. Uranium speciation in waters of different uranium mining areas. *J. Alloys Compd.* **271–273,** 201–205 (1998).

80.   Berto, S. *et al.* Advances in the investigation of dioxouranium(VI) complexes of interest for natural fluids. *Coord. Chem. Rev.* **256,** 63–81 (2012).

81.   Rout, S., Ravi, P. M., Kumar, A. & Tripathi, R. M. Equilibrium isotherm and kinetics modeling of U(VI) adsorption by natural soil systems. *J. Radioanal. Nucl. Chem.* **303,** 2193–2203 (2015).

82.   Unsworth, E. R., Jones, P. & Hill, S. J. The effect of thermodynamic data on computer model predictions of uranium speciation in natural water systems. *J. Environ. Monit.* **4,** 528–532 (2002).

83.   Rosner, G., Hoetzl, H. & Winkler, R. Simultaneous radiochemical determination of plutonium, strontium, uranium, and iron nuclides in atmospheric deposition and aerosol samples. *Fresenius. J. Anal. Chem.* **338,** 606–609 (1990).

84.   Martinez-Aguirre, A. & Garcia-Leon, M. Transfer of natural radionuclides from soils to plants in a wet marshland. *Appl. Radiat. Isot.* **47,** 1103–1108 (1996).

85.   Horwitz Chiarizia, R., Dietz, M.L., Diamond, H., Nelson, D.M., E. P. Separation and preconcentration of actinides from acidic\rmedia by extraction chromatography. *Anal. Chim. Acta* **281,** 361–372 (1993).

86.   Horwitz, E. P. *et al.* Separation and preconcentration of actinides by extraction chromatography using a supported liquid anion exchanger: application to the characterization of high-level nuclear waste solutions. *Anal. Chim. Acta* **310,** 63–78 (1995).

87.   Tsushima, S. On the 'yl' bond weakening in uranyl(VI) coordination complexes. *Dalt. Trans.* **40,** 6732–6737 (2011).

88.   Nguyen Trung, C., Begun, G. M. & Palmer, D. A. Aqueous uranium complexes. 2. Raman spectroscopic study of the complex formation of the dioxouranium(VI) ion with a variety of inorganic and organic ligands. *Inorg. Chem.* **31,** 5280–5287 (1992).

103

89. Lu, G., Forbes, T. Z. & Haes, A. J. Evaluating Best Practices in Raman Spectral Analysis for Uranium Speciation and Relative Abundance in Aqueous Solutions. *Anal. Chem.* **88,** 773–780 (2016).

90. Foerstendorf, H., Jordan, N. & Heim, K. Probing the surface speciation of uranium (VI) on iron (hydr)oxides by in situ ATR FT-IR spectroscopy. *J. Colloid Interface Sci.* **416,** 133–138 (2014).

91. De Jong, W. A. *et al.* Complexation of the Carbonate, Nitrate, and Acetate Anions with the Uranyl Dication: Density Functional Studies with Relativistic Effective Core Potentials. *J. Phys. Chem. A* **109,** 11568–11577 (2005).

92. Chu, Y., Banaee, M. G. & Crozier, K. B. Double-Resonance Plasmon Substrates for Surface-Enhanced Raman Scattering with Enhancement at Excitation and Stokes Frequencies. *ACS Nano* **4,** 2804–2810 (2010).

93. Haynes, C. L., Yonzon, C. R., Zhang, X. & Van Duyne, R. P. Surface-enhanced Raman sensors: Early history and the development of sensors for quantitative biowarfare agent and glucose detection. *J. Raman Spectrosc.* **36,** 471–484 (2005).

94. Haynes, C. L. & Van Duyne, R. P. Plasmon-Sampled Surface-Enhanced Raman Excitation Spectroscopy. *J. Phys. Chem. B* **107,** 7426–7433 (2003).

95. Teiten, B. & Burneau, A. Detection and sorption study of dioxouranium(VI) ions on N-(2-mercaptopropionyl)glycine-modified silver colloid by surface-enhanced Raman scattering. *J. Raman Spectrosc.* **28,** 879–884 (1997).

96. Ruan, C., Luo, W., Wang, W. & Gu, B. Surface-enhanced Raman spectroscopy for uranium detection and analysis in environmental samples. *Anal. Chim. Acta* **605,** 80–86 (2007).

97. Leverette, C. L. *et al.* Trace detection and differentiation of uranyl(VI) ion cast films utilizing aligned Ag nanorod SERS substrates. *Vib. Spectrosc.* **50,** 143–151 (2009).

98. Dai, S., Lee, Y.-H. & Young, J. P. Observation of the surface-enhanced Raman scattering spectrum of uranyl ion. *Appl. Spectrosc.* **50,** 536–537 (1996).

99. Bhandari, D., Wells, S. M., Retterer, S. T. & Sepaniak, M. J. Characterization and Detection of Uranyl Ion Sorption on Silver Surfaces Using Surface Enhanced Raman Spectroscopy. *Anal. Chem. (Washington, DC, United States)* **81,** 8061–8067 (2009).

100. Bao, L., Yan, H., Mahurin, S. M., Gu, B. & Dai, S. Surface-enhanced Raman scattering of uranyl-humic complexes using a silver-doped sol-gel substrate. *ACS Symp. Ser.* **943,** 53–63 (2006).

101. Taylor, C. E., Garvey, S. D. & Pemberton, J. E. Carbon Contamination at Silver Surfaces: Surface Preparation Procedures Evaluated by Raman Spectroscopy and X-ray Photoelectron Spectroscopy. *Anal. Chem.* **68,** 2401–2408 (1996).

102. Nalbandian, M. J. *et al.* Tailored Synthesis of Photoactive TiO2 Nanofibers and Au/TiO2 Nanofiber Composites: Structure and Reactivity Optimization for Water Treatment Applications. *Environ. Sci. Technol.* **49,** 1654–1663 (2015).

103. Nalbandian, M. J. *et al.* Synthesis and optimization of BiVO4 and co-catalyzed BiVO4 nanofibers for visible light-activated photocatalytic degradation of aquatic micropollutants. *J. Mol. Catal. A Chem.* **404–405,** 18–26 (2015).

104. Nalbandian, M. J. *et al.* Synthesis and optimization of Fe2O3 nanofibers for chromate adsorption from contaminated water sources. *Chemosphere* **144,** 975–981 (2016).

105. Nalbandian, M. J. *et al.* Synthesis and optimization of Ag-TiO2 composite nanofibers for photocatalytic treatment of impaired water sources. *J. Hazard. Mater.* **299,** 141–148 (2015).

106. Horzum, N. *et al.* Hierarchically Structured Metal Oxide/Silica Nanofibers by Colloid Electrospinning. *ACS Appl. Mater. Interfaces* **4,** 6338–6345 (2012).

107. Horzum, N., Taşçıoglu, D., Okur, S. & Demir, M. M. Humidity sensing properties of ZnO-based fibers by electrospinning. *Talanta* **85,** 1105–1111 (2011).

108. Li, W. P. *et al.* Recovery of uranyl from aqueous solutions using amidoximated polyacrylonitrile/exfoliated Na-montmorillonite composite. *Chem. Eng. J.* **279,** 735–746 (2015).

109. Leggett, C. J., Endrizzi, F. & Rao, L. Scientific Basis for Efficient Extraction of Uranium from Seawater, II: Fundamental Thermodynamic and Structural Studies. *Ind. Eng. Chem. Res.* **55,** 4257–4263 (2016).

110. Abney, C. W. *et al.* XAFS investigation of polyamidoxime-bound uranyl contests the paradigm from small molecule studies. *Energy Environ. Sci.* **9,** 448–453 (2016).

111. Endrizzi, F., Leggett, C. J. & Rao, L. Scientific Basis for Efficient Extraction of Uranium from Seawater. I: Understanding the Chemical Speciation of Uranium under Seawater Conditions. *Ind. Eng. Chem. Res.* **55,** 4249–4256 (2016).

112. Endrizzi, F., Melchior, A., Tolazzi, M. & Rao, L. Complexation of uranium(VI) with glutarimidoxioxime: thermodynamic and computational studies. *Dalt. Trans.* **44,** 13835–13844 (2015).

113. Lashley, M. A. *et al.* Amidoximes as ligand functionalities for braided polymeric materials for the recovery of uranium from seawater. *Polyhedron* **109,** 81–91 (2016).

114. Mehio, N. *et al.* Quantifying the binding strength of salicylaldoxime-uranyl complexes relative to competing salicylaldoxime-transition metal ion complexes in aqueous solution: a combined experimental and computational study. *Dalt. Trans.* **45,** 9051–9064 (2016).

115. Mehio, N. *et al.* Acidity of the Amidoxime Functional Group in Aqueous Solution: A Combined Experimental and Computational Study. *J. Phys. Chem. B* **119,** 3567–3576 (2015).

116. Tsantis, S. T. *et al.* Binding of oxime group to uranyl ion. *Dalt. Trans.* **45,** 9307–9319 (2016).

117. Sadeghi, S., Azhdari, H., Arabi, H. & Moghaddam, A. Z. Surface modified magnetic Fe3O4 nanoparticles as a selective sorbent for solid phase extraction of uranyl ions from water samples. *J. Hazard. Mater.* **215–216,** 208–216 (2012).

118. Zhuang, Z., Chen, H., Lin, Z. & Dang, Z. Mn2O3 hollow spheres synthesized based on an ion-exchange strategy from amorphous calcium carbonate for highly efficient trace-level uranyl extraction. *Environ. Sci. Nano* **3,** 1254–1258 (2016).

119. Lee, H. G., Sai-Anand, G., Lee, K.-P., Kang, S.-W. & Gopalan, A. I. Development of novel electrospun functional nanofibrous mats for efficient uranium/lithium recovery. *Sci. Adv. Mater.* **6,** 1365–1374 (2014).

120. Zhang, B. *et al.* Synergistic nanofibrous adsorbent for uranium extraction from seawater. *RSC Adv.* **6,** 81995–82005 (2016).

121. Tripathi, B. P., Dubey, N. C., Subair, R., Choudhury, S. & Stamm, M. Enhanced hydrophilic and antifouling polyacrylonitrile membrane with polydopamine modified silica nanoparticles. *RSC Adv.* **6,** 4448–4457 (2016).

122. Sutton, M. & Burastero, S. R. Uranium(VI) Solubility and Speciation in Simulated Elemental Human Biological Fluids. *Chem. Res. Toxicol.* **17,** 1468–1480 (2004).

123. Maya, L. Sorbed uranium(VI) species on hydrous titania, zirconia, and silica gel. *Radiochim. Acta* **31,** 147–151 (1982).

124. Mehio, N. *et al.* Acidity of the Poly(acrylamidoxime) Adsorbent in Aqueous Solution: Determination of the Proton Affinity Distribution via Potentiometric Titrations. *Ind. Eng. Chem. Res.* **55,** 4217–4223 (2016).

125. Tian, G., Teat, S. J., Zhang, Z. & Rao, L. Sequestering uranium from seawater: binding strength and modes of uranyl complexes with glutarimidedioxime. *Dalt. Trans.* **41,** 11579–11586 (2012).

126. Buchanan, K. J., Hird, B. & Letcher, T. M. Crosslinked poly(sodium acrylate) hydrogels. *Polym. Bull.* **15,** 325–332 (1986).

127. Stafie, N., Stamatialis, D. F. & Wessling, M. Insight into the transport of hexane-solute systems through tailor-made composite membranes. *J. Membr. Sci.* **228,** 103–116 (2004).

128. Kwasnieski, D. T., Wang, H. & Schultz, Z. D. Alkyl-nitrile adlayers as probes of plasmonically induced electric fields. *Chem. Sci.* **6,** 4484–4494 (2015).

129. Wijenayaka, L. A., Ivanov, M. R., Cheatum, C. M. & Haes, A. J. Improved Parametrization for Extended Derjaguin, Landau, Verwey, and Overbeek Predictions of Functionalized Gold Nanosphere Stability. *J. Phys. Chem. C* **119,** 10064–10075 (2015).

130. Bao, L., Mahurin, S. M., Haire, R. G. & Dai, S. Silver-Doped Sol-Gel Film as a Surface-Enhanced Raman Scattering Substrate for Detection of Uranyl and Neptunyl Ions. *Anal. Chem.* **75,** 6614–6620 (2003).

131. Lucas, L. J. *et al.* Development of a sensitive, stable and EGFR-specific molecular imaging agent for surface enhanced Raman spectroscopy. *J. Raman Spectrosc.* **46,** 434–446 (2015).

132. Yang, L., Li, P., Liu, H., Tang, X. & Liu, J. A dynamic surface enhanced Raman spectroscopy method for ultra-sensitive detection: from the wet state to the dry state. *Chem. Soc. Rev.* **44,** 2837–2848 (2015).

133. Osman, A. A. A., Geipel, G., Barkleit, A. & Bernhard, G. Uranium(VI) Binding Forms in Selected Human Body Fluids: Thermodynamic Calculations versus Spectroscopic Measurements. *Chem. Res. Toxicol.* **28,** 238–247 (2015).

134. Bromberg, L. *et al.* Degradation of Chemical Warfare Agents by Reactive Polymers. *Ind. Eng. Chem. Res.* **48,** 1650–1659 (2009).

135. de Puig, H., Tam, J. O., Yen, C.-W., Gehrke, L. & Hamad-Schifferli, K. Extinction Coefficient of Gold Nanostars. *J. Phys. Chem. C* **119,** 17408–17415 (2015).

136. Takeno, N. Atlas of Eh-pH diagrams Intercomparison of thermodynamic databases. *Natl. Inst. Adv. Ind. Sci. Technol. Tokyo* 285 (2005).

137. Suleimenov, O. M., Seward, T. M. & Hovey, J. K. A spectrophotometric study on uranyl nitrate complexation to 150∈°C. *J. Solution Chem.* **36,** 1093–1102 (2007).